UNIVERSITÀ DEGLI STUDI DI GENOVA
FACOLTÀ DI INGEGNERIA

DOTTORATO IN INGEGNERIA ELETTRICA (XX CICLO)

MULTISCALE ANALYSIS FOR OPTIMIZED VESSEL SEGMENTATION OF FUNDUS RETINA IMAGES

Tutor: Chiar.mo Prof. Mauro Parodi

Candidato: Andrea Anzalone

Abstract

Automated segmentation of the vascolature in retinal images is important in the detection of a number of eye diseases. Some diseases, e.g retinopathy of prematurity, affect the morphology of the vessel tree itself. In other cases, e.g. pathologies like microaneurysms, the performance of automatic detection methods may be improved if regions containing vascolature can be excluded from the analysis. Another important application of automatic retinal vessel segmentation is in the registration of retinal images of the same patient taken at different times. Therefore the automatic vessel segmentation forms an essential component of any automated eye-disease screening system.

In this thesis an algorithm for the segmentation of the vessels in the images of the fundus of the human retina is developed. In the first chapter we introduce some notations about the eye, the imaging technology and the archives of images. In the second chapter we show the state of art of the techniques proposed in the literature about vessel extraction. Since retinal vessels have a range of different sizes, it is a natural choice the use of an algorithm based on the multiscale analysis, so in the third chapter we deal in detail with the multiscale paradigm, and we discuss a mathematical framework to face this kind of problems using a differential and variational approach. In the fourth chapter we talk about the algorithm developed to achieve the segmentation of the retinal vessels. The algorithm is modular and is made up of two fundamental blocks. The former is devoted to vessel enhancement, using a linear multiscale analysis for ridge detection, the latter provides a binary image by resorting to both a thresholding procedure and cleaning operations. The optimal values of two algorithm parameters are found out by maximizing proper measures of performances able to evaluate from a quantitative point of view the results provided by the proposed algorithm. The choice of the measure of performance allows one to tailor the solution to the specific image features to be emphasized. Some simulation results are presented and the performances of the algorithm are compared with those of other methods proposed in the literature. In the fifth chapter we show the result improvements obtained using a nonlinear multiscale analysis (Total Variation Motion) instead of a linear technique.

Ringraziamenti

Un grazie al Chiar. professor Mauro Parodi per l'attenzione che mi ha dedicato nei tre anni di dottorato e per la pazienza e la cura con cui ha seguito mattone dopo mattone la costruzione di questa tesi.

Un grazie al Chiar. professor Marco Storace e al Dott. Ing. Federico Bizzarri per i preziosi consigli e per l'interesse con cui hanno ascoltato passo dopo passo i resoconti del mio viaggio nel mondo dell'elaborazione di immagini.

Un grazie a Marina, Tomaso, Dano, Daniele per la loro compagnia che ha reso piacevole il tempo passato in questi anni nei dintorni del laboratorio di Sistemi Complessi Non Lineari del DIBE.

Un grazie alla mia famiglia per la totale libertà che mi hanno lasciato in questi anni di studio e per l'attenzione con cui hanno sostenuto ogni mia scelta dopo che era stata presa.

Un grazie ai miei amici di una vita per tutto il sostegno ricevuto e per la pazienza con cui hanno spesso ascoltato i racconti delle mirabilia viste in questi anni di studio che ho affrontato e che tanto mi è piaciuto affrontare.

Contents

List of Figures

List of Tables

List of Abbreviations

AWGN	Additive White Gaussian Noise
CLAHE	Contrast-Limited Adaptive Histogram Equalization
DRIVE	Digital Retinal Images for Vessel Extraction
FOV	Field Of View
FPF	False Positive Fraction
MAA	Maximum Average Accuracy
PDE	Partial Differential Equation
TPF	True Positive Fraction
TVM	Total Variation Motion

Chapter 1

Introduction

Automated segmentation of the vascolature in retinal images is important in the detection of a number of eye diseases. Some diseases, e.g retinopathy of prematurity, affect the morphology of the vessel tree itself. In other cases, e.g. pathologies like microaneurysms, the performance of automatic detection methods may be improved if regions containing vascolature can be excluded from the analysis. Another important application of automatic retinal vessel segmentation is the registration of retinal images of the same patient taken at different times. The registered images are useful for automatically monitoring the progression of certain diseases. Finally, the position, size and shape of the vascolature provides information which can be used to locate the optic disk and the fovea. Therefore the automatic vessel segmentation constitutes an essential component of any automated eye-disease screening system.

1.1 Anatomy of the eye

In Figure 1.1 we can see a transverse section of the left human eyeball: all the structures of main interest are labelled.

The outer layer of the eyeball is called **fibrous tunic** and it is composed of the *sclera* and *cornea*: the former provides shape and protects inner parts, the latter admits and refracts light. The middle coat of the eye is named **vascular tunic** and comprises: the *choroid*, which provides blood supply and absorbs scattered light; the *ciliar body*, which secrets aqueous humor and alters the shape of lens for near or far vision; the *iris*, which regulates the amount of light that enters the eyeball.

The inner layer is called **nervous tunic** or **retina**: light enters the pupil (the aperture in the iris), is focused and inverted by the cornea and lens, and is projected onto the retina. The **retina** is a soft, transparent layer of nervous tissue made up of

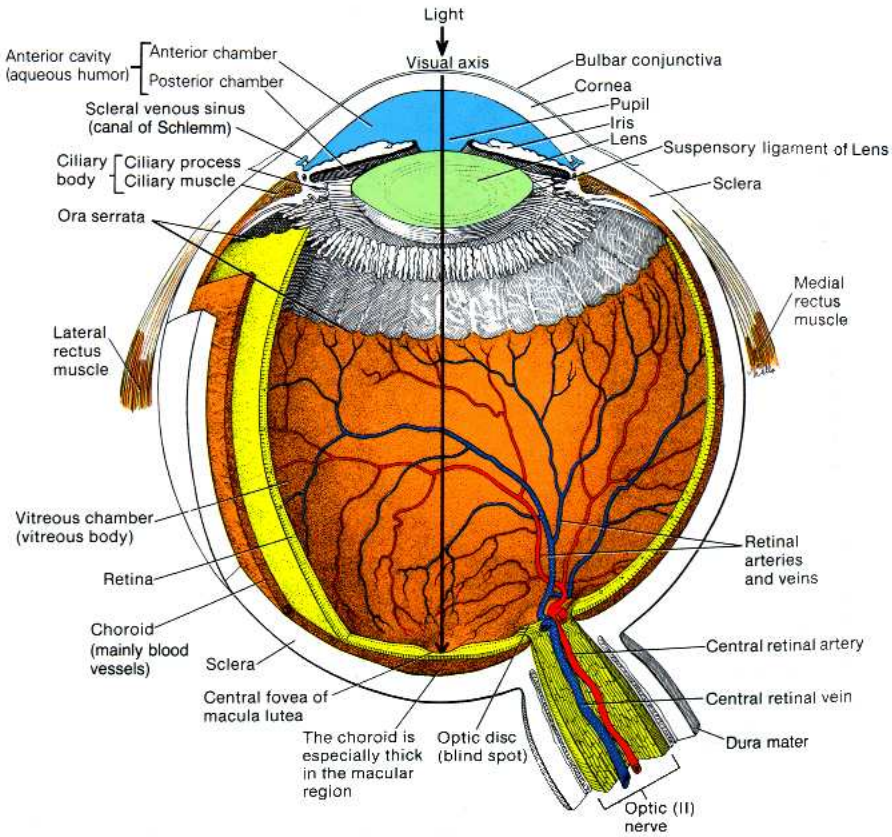

Figure 1.1: A tranverse section of the left eyeball (superior view)

millions of light receptors.

The retina is connected to the brain by the optic nerve. All of the structures needed to focus light onto the retina and to nourish it are housed in the eye, which can be considered, from this point of view, a supporting shell for the retina.

Two separate vascular systems are involved in the nutrition of the eye. The first is made up of the *uveal*, or ciliary, blood vessels and supply the oxygen to the iris, the ciliary body and the choroid. It serves also in part the nervous tunic, that owns a further an autonomous vascular system, whose vessels are called *retinal vessels*.

The retinal vessels are distributed within the inner two thirds of the retina, whereas the outer layers, including the photoreceptors, are avascular and nourished from the choroid. An avascular zone, which enables light to reach the central photoreceptors without encountering a single blood vessel, is seen centrally in the *fovea*. Arteries and veins are located within the nerve fiber layer. The capillaries are arranged in a laminated fashion with two layers of flat capillary networks in a large part of the retina.

The retinal capillaries have a diameter of 5 - 6 μm [1]. Retinal arterial diameters range between 40 - 160 μm [2], 160 μm presumably refers to the central artery. The diameters of the superior temporal and inferior temporal branches measures approximately 120 μm [3].

1.2 Imaging Techniques

Traditionally, the retina has been observed directly via either an ophthalmoscope or similar optical devices such as the fundus camera. **Fundus photography** (also known as "retinal photography") refers to a non-invasive technique for the documentation of the posterior pole of the eye (retina and choroid) utilizing a color film and a specialized instrument called "fundus camera". Fundus photography was first described by Jackman and Webster in 1886, and modern fundus photography began with the introduction of commercially available fundus cameras in 1926. In Figure 1.2 we have an example of fundus image where the main structures of the retina are pointed out.

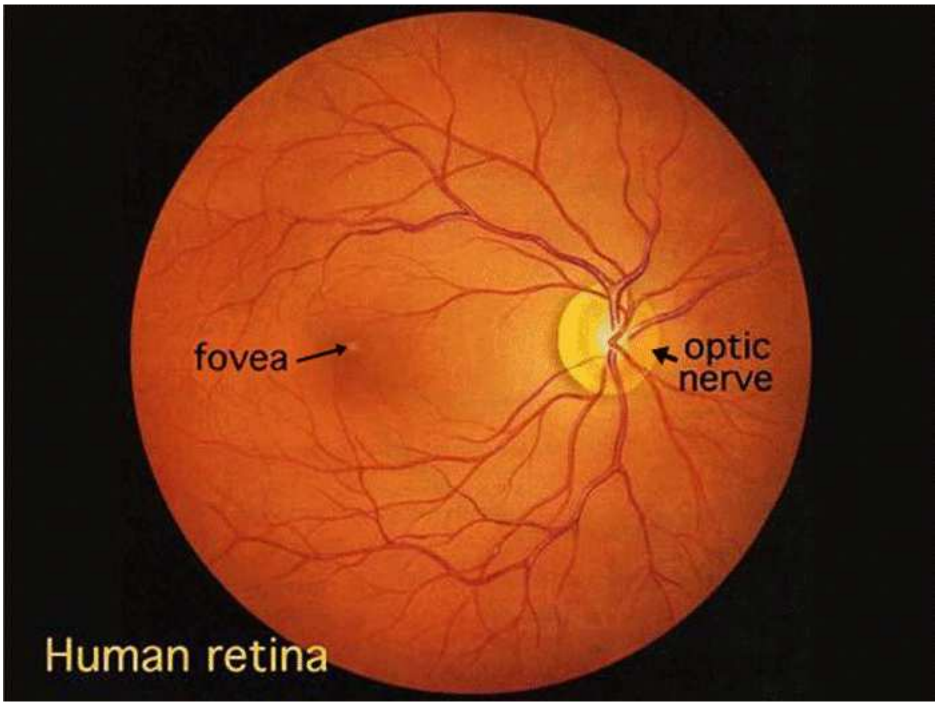

Figure 1.2: An example of fundus image

The term "**red-free**" refers to fundus photographs taken either using (*a priori*) a green filter (540 - 570 nm) over the light source or extracting (*a posteriori*) from the original color images the green channel, which gives the highest contrast between vessels and background [4]. After the acquisition, the images are digitized, thus becoming available for computer processing.

Other imaging techniques are commonly used in medicine. In 1961 **fluorescein angiography**, or fluorescent angiography, was developed by Novotny and Alvis [5]. In this case, sodium fluorescein is injected into a vein, and under filtered light the sodium fluorescein within the blood fluoresces, glowing brightly and providing easily observed patterns of blood flow within the eye. This allows the arteries, capillaries and veins to be easily identified and photographed, and from this, large amounts of information concerning the health of the circulatory system can be determined. Once the dye is administered the speed with which passages fill with marked blood, the rate at which this marked blood spreads through the eye and the time taken for the dyed blood to pass out of the eye are observed. These observations provide valuable data about the effectiveness and degree of degeneration of the circulatory system of the eye, which has been shown to be indicative of the circulatory system of the entire body.

During the 1990's the **indocyanine green dye angiography** technique was developed; similarly to the flourescein angiography, a dye is injected into the blood, however the indocyanine green dye glows in the infra-red section of the spectrum. The indocyanine green dye approach only came into widespread use when digital cameras sensitive into the infra-red became commonly available, and it complements fluorescein angiography by highlighting different aspects of the vascolature of the eye. In particular it enhances the structure of the choroid, which is the layer of blood vessels beneath the retina. These two techniques can be used together to gain a more thorough understanding of the structure and pathologies affecting an eye. They can illustrate patterns of blood flow, haemorraging and obstructions within the vascular system, but, like the ophthalmoscope, both require trained medical staff to perform the procedure, and a clinical environment where the images can be taken and analysed.

In addition to these methods for observing the vascolature of the eye, there is a variety of other, more advanced, methods for mapping structures and changes within the eye, including ultrasound and laser tomography and laser-based blood flowmeters in development and in use. All of these can be used to scan the eye and make observations and diagnoses on the eye and circulatory system.

1.3 Archives of retinal images

Several archives of digital fundus images are of public domain. They all refer to projects devoted to develope systems for the automatic diagnosis of the human eye diseases.

One of these archives is the DRIVE (Digital Retinal Images for Vessel Extraction) database [6], that consists of a total of 40 color fundus photographs. All images have been deidentified, they were stripped from all individually identifiable information and processed in such a way that this information cannot be reconstructed from the images. The photographs were obtained from a diabetic retinopathy screening program in The Netherlands. The screening population consisted of 453 subjects between 31 to 86 years of age. Each image has been JPEG compressed, which is common practice in screening programs. Among the 40 images in the database, 7 contain pathologies, namely exudates, hemorrhages and pigment epithelium changes.

The images were acquired using a Canon CR5 non-mydriatic 3CCD camera with a 45 degree field of view (FOV). Each image is captured using 8 bits per color plane at 768×584 pixels. The FOV of each image is circular with a diameter of approximately 540 pixels.

The set of 40 images was subdivided into a test and a training set both containing 20 images. Five independent human observers manually segmented a number of images. All observers were trained by an experienced ophthalmologist. The first observer segmented 14 images of the training set while the second observer segmented the other 6 images. The test set was segmented twice resulting in a set X and Y. Set X was segmented by both the first and second observer (13 and 7 images respectively) while set Y was completely segmented by the third observer. The performance of the vessel segmentation algorithms is measured on the test set. In set X the observers marked 577,649 pixels as vessel and 3,960,494 as background (12.7% vessel). In set Y 556,532 pixels are marked as vessel and 3,981,611 as background (12.3% vessel).

1.4 Mathematical definition of images

We deal with digital image analysis, so we have to properly define the notion of *image*. Nowadays, images on computers are stored using discrete representation of the data but one generally assumes that the discretization is thin enough (in the spatial directions) to be able to approximate these discrete signals by continuous (or at least piecewise continuous) mathematical functions. This is debatable and we refer the reader to [7, 8] for interesting discussions about this subject. Nevertheless, the possibility to apply classical mathematical tools as well as the good results obtained with continuous models lead us to choose this approach.

Analitically, a generic n-dimensional image can be defined as an adimensional continuous function

$$I(\mathbf{x}) : \mathbf{x} \in \Omega \subset \Re^n \rightarrow \Re^m \tag{1.1}$$

where Ω is the **image domain**.

Common values are $n = 2$ (2D or **bidimensional images**) and $n = 3$ (3D images). In the following of this thesis we will refer only to the bidimensional case without loss of generality: as a matter of fact, the results that we will obtain can be straightforwardly extended to higher dimensional cases. If $m = 1$ we deal with **monocromatic** images. For color images, we have $m = 3$. A commonly used space is RGB (Red, Green, Blue) color space, but many other color spaces are widely used: for example HSV (Hue, Saturation, Lightness) or YUV spaces (a model that defines the color space in terms of one brightness and two chrominance components).

We assume (working hypothesis) that Ω is a square domain; for $n = 2$ we have:

$$\Omega \in [0, 1] \times [0, 1] \tag{1.2}$$

For monocromatic images, I($\mathbf{x}$) can be physically thought of as a function that associates a brightness level to any point $P \equiv (x, y) \in \Omega$. This value is named **gray level**: high values represent bright regions of the image, low values correspond to dark regions.

Mathematically, we can think of $I(x, y)$ as a surface in the $\Re^3$ space (x, y, I), as illustrated in Figure 1.3

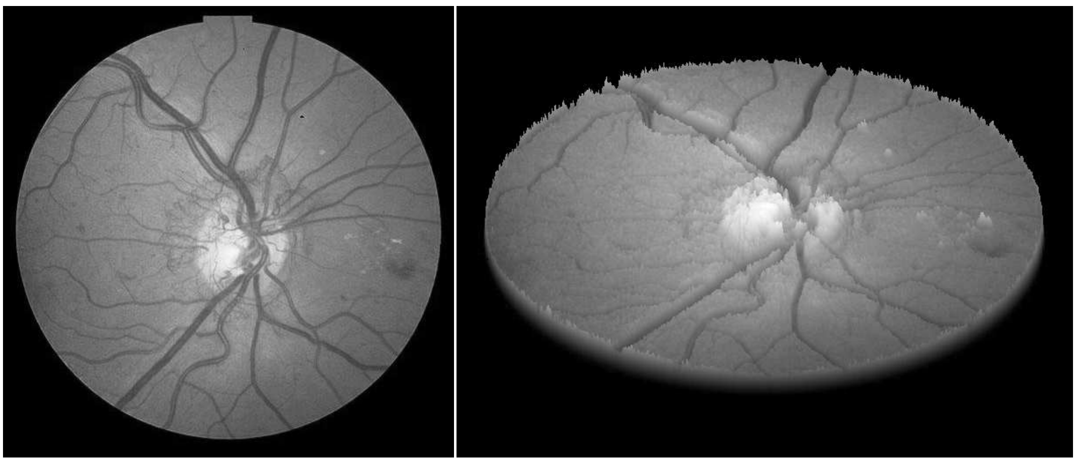

(a) (b)

Figure 1.3: (a) the image $I(x, y)$ (b) $I(x, y)$ as surface in a 3D space.

We assume, moreover, that

$$I \in [0, 255] \tag{1.3}$$

This choice allows us, after a quantization process, to represent the gray levels of a continuous image with a 8-bit encoding inside a computer. Considering a generic $\hat{I} \in [a, b]$, we can get back the conventional range through the following relationship:

$$I = \frac{\hat{I} - a}{b - a} 255 \tag{1.4}$$

A computer can process only a numerical representation of an image, defined as a matrix M_I of dimension $M \times N$. Each element of the matrix M_I is representative of the constant level of brightness of one subregion of the image (the pixel). Supposing to use an 8-bit encoding, 256 possible values (from 0 to 255) are associated to every pixel. We can pass from $I(x)$ to M_I, through an intermediate step, the discrete representation D_I. We divide the domain in many identical square dowels $\Omega_{i,j}$ (in analogy with the regular disposition of the pixels in the image). A value of constant brightness, obtained by sampling $I(x, y)$ in the center of the dowel is associated with every subdomain $\Omega_{i,j}$ is associated. What we have at this point is a matrix I_M of real values, belonging to the interval [0,255]. This is the **discrete representation** of an image. This is the representation used in analog circuits for image processing, such as the so-called cellular Neural Networks (CNNs) [9].

By quantizating the set of brightness values, instead, we obtain the matrix M_I of natural values, belonging to the set {0,255}, that constitutes the **numerical representation** of an image. This is the representation we have to use if we want to process images using a digital architecture.

1.5 Image derivatives

The derivative of an image I with respect to the variable a is written as follows

$$I_a = \frac{\partial I}{\partial a} \tag{1.5}$$

The derivatives of a *scalar image* I with respect to its spatial coordinates (x, y) form *the image gradient* and is denoted by ∇I

$$\nabla I = (I_x, I_y)^T \tag{1.6}$$

By varying (x, y) the image gradient describes a vector-valued field $\nabla I : \Omega \rightarrow \Re^2$ representing the maximum variation directions and magnitudes of the scalar image I. The *gradient norm* $\|\nabla I\| = \sqrt{I_x^2 + I_y^2}$ is often used in image analysis, since it gives a scalar and pointwise measure of the image variations, as shown in Figure 1.4.

(a) (b)

Figure 1.4: (a) The image $I(x, y)$ (b) Its gradient norm $\|\nabla I(x, y)\|$.

For directional derivatives in a direction $\mathbf{u} = (u, v)^T \in \Re^2$, we use the following notations:

$$I_u = \frac{\partial I}{\partial \mathbf{u}} = \nabla I \mathbf{u} = u I_x + v I_y \tag{1.7}$$

In the same way, the second derivative of a scalar image I with respect to a and b is denoted by

$$I_{ab} = \frac{\partial^2 I}{\partial a \partial b} \tag{1.8}$$

We define the *Hessian of I* as the matrix $\boldsymbol{H}$ of the second derivatives with respect to the spatial coordinates:

$$H = \begin{bmatrix} I_{xx}(x, y) & I_{xy}(x, y) \\ I_{yx}(x, y) & I_{yy}(x, y) \end{bmatrix} \tag{1.9}$$

The matrix H will be largely used throughout this thesis. We assume that our images are regular enough, so that $I_{xy} = I_{yx}$. Then, $\boldsymbol{H}$ is a *symmetric matrix*. As for *second directional-derivatives* in a direction $\mathbf{u} = (u, v)^T \in \Re^2$, the following notations are equivalent:

$$\begin{aligned} I_{uu} &= \frac{\partial^2 I}{\partial \mathbf{u}^2} = \nabla(\nabla I \mathbf{u})\mathbf{u} = \mathbf{u}^T H \mathbf{u} = trace(H\mathbf{u}\mathbf{u}^T) \\ &= u^2 I_{xx} + 2uvI_{xy} + v^2 I_{yy} \end{aligned} \tag{1.10}$$

A commonly used operator involving the second order derivatives is the Laplacian operator Δ, defined as follow:

$$\Delta I = trace(H) = I_{xx} + I_{yy} \tag{1.11}$$

1.6 Objectives

In this thesis we use archives of images to train an algorithm for the vessel segmentation of retinal fundus images.
In this chapter, we introduced some notations about the eye, the imaging technology and the archives of images.
In the second chapter we show the state of the art of the techniques proposed in the scientific literature concerning vessel extraction.
Since retinal vessels have a range of different sizes, it is a natural choice the use of an algorithm based on the multiscale analysis, so in the third chapter we deal in detail with the multiscale paradigm, and we discuss a mathematical framework to face this matters using a differential and variational approach.
In the fourth chapter we talk about the algorithm developed to achieve the segmentation of retinal vessels. The algorithm is modular and is made up of two fundamental blocks. The former is devoted to vessel enhancement, using a linear multiscale analysis for ridge detection, while the latter provides a binary image by resorting to both a thresholding procedure and cleaning operations. The optimal values of two algorithm parameters are found out by maximizing proper measures of performances able to evaluate from a quantitative point of view the results provided by the proposed algorithm. The choice of the measure of performance allows one to tailor the solution to the specific image features to be emphasized. Some simulation results are presented and the performances of the algorithm are compared with those of other methods proposed in the literature.
In the fifth chapter we show the improvements of the results that obtain by using a nonlinear multiscale analysis (Total Variation Motion) instead of the linear one used in the previous chapter.

Chapter 2

Vessel segmentation

The purpose of image segmentation is to partition an image into meaningful regions with respect to a particular application. Image segmentation has been, and still is, a relevant research area and hundreds of segmentation algorithms have been proposed in the last 30 years. Many segmentation methods are based on two basic properties of the pixels in relation to their local neighbourhood: discontinuity and similarity. Methods based on pixel discontinuity are called boundary-based methods, whereas methods based on pixel similarity are called region-based methods. However, it is well known that such segmentation techniques - based on boundary or region information alone - often fail to produce accurate segmentation results [10]. Hence, in the last few years, there has been a tendency towards algorithms which take advantage of the complementary nature of such information.

Reviewing the different works on region-based segmentation which have been proposed [11, 12], it is interesting to note the evolution of region-based segmentation methods, which were initially focused on grey-level images, and which gradually incorporated colour, and more recently, texture. As a matter of fact we can think to extract from the image a map of the feature of interest and apply the segmentation task to this and not to the original greyscale image.
This is a natural choice if we want to segment parts of image that share a particular geometrical pattern, like the vessels in fundus retina, which can be identified considering their tabular structure, thinking a bidimensional image as a 3D surface.

2.1 State of the art in vessel extraction techniques

Blood vessel delineation on medical images forms an essential step in solving several practical applications such as diagnosis of the vessels [13, 14, 15]. It can be useful also as a preliminary step for registration of images of the same patient obtained at different times.

The segmentation task aims to isolate the structure of interest of the fundus image highlighting them versus other regions of the image that are considered not important (e.g. vessels versus optic disk); moreover, the processing of this kind of images can be divided in two steps: the first one is the segmentation itself, the second one is the extraction of parameters of interest from the segmented image (e.g. vessel diameter, number of occlusions or haemorrhagies, etc.).
The segmentation is then useful to pre-process in the best way the fundus image, trying to eliminate elements unnecessary in the further analyses and to highlight what is important in the specific context of the application.

The vessel segmentation can be obtained by resorting to different methods (see [14, 16] for an overview), either rule-based or supervised. In the latter case, the rule for the vessel extraction is "learned" by the algorithm on the basis of a training set of reference manually-processed images. Various algorithms with a partial supervision strategy have been recently proposed [17, 18, 19].

We don't enforce any taxonomy at the beginning of this chapter. Instead, we put into the same group papers that use similar approaches. During the categorization that follows in the next pages, we try to be as specific as possible. In the following, a summary of vessel extraction techniques and algorithms is proposed:

1. Pattern recognition techniques;
   (a) Matching filters approaches
   (b) Ridge-based approaches
   (c) Region growing approaches
   (d) Multi-scale approaches
   (e) Skeleton-based approaches
   (f) Mathematical morphology schemes
2. Deformable models
   (a) Active contours (Snakes)
   (b) Level set methods
3. Tracking-based approaches
4. Artificial-intelligence-based approaches
5. Neural-network-based approaches
6. Wavelets

2.2 Pattern recognition techniques

Pattern recognition (PR) techniques deal with the detection or classification of objects or features. Humans are very well adapted to carry out PR tasks. Some of the PR techniques are the adaptation of human PR ability to the computer systems. In the vessel extraction domain, PR techniques are concerned with the automatical detection of vessel structures and features.

2.2.1 Matching filters approaches

Matching filters approach convolves the image with multiple matched filters for the extraction of objects of interest. In extracting vessel contours, designing different filters to detect the vessels with different orientations and sizes plays a crucial role [20]. The convolution kernel size affects the computational weight. Matching filters are usually followed by some other image processing operations like thresholding and connected component analysis to get the final vessel contours. Connected component analysis is preceded by a thinning process to detect vessel centerlines.

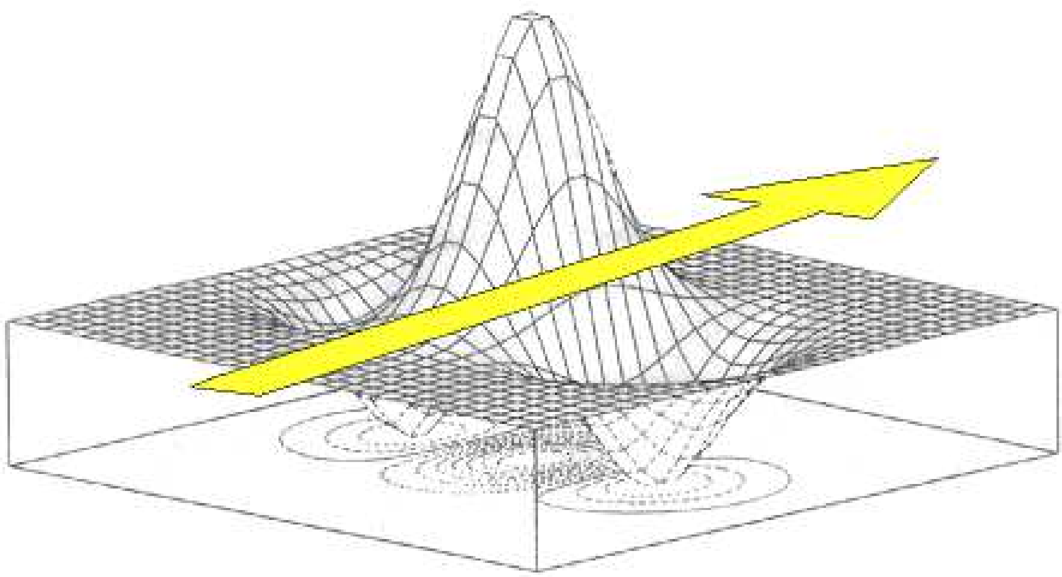

Figure 2.1: Example of filter that enhances all the patterns oriented like the arrow

The matched filter method has some parameters governing its detection process. The

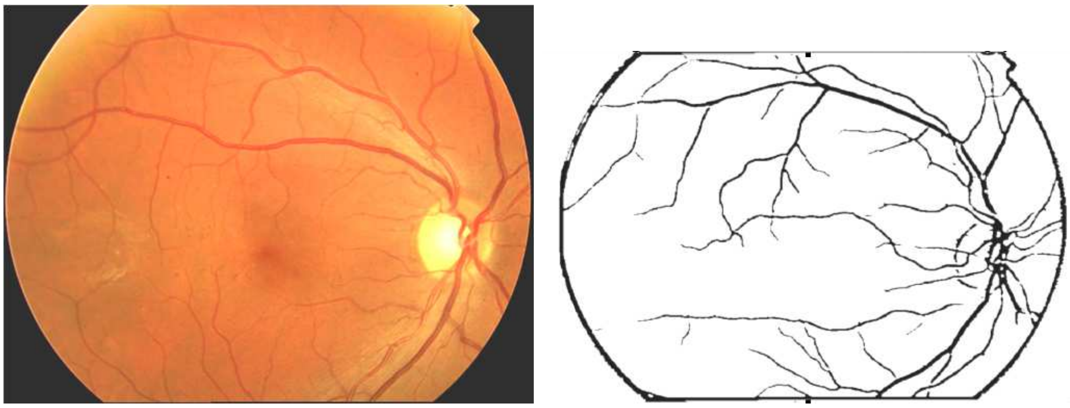

(a) (b)

Figure 2.2: (a) A red-free image. (b) Elaboration result using matching filters.

values of matched filter parameters were proposed in [20] and have been used since then in all other works for applications and comparisons. In [4] a method is proposed to improve the thresholding (and hence the segmentation) of the matched filter output image but the matched filter parameters are never changed. Only in [18] an optimization method using the DRIVE [6] database to adjust the matched filter parameters to increase the performances is presented. The optimization procedure is performed by comparing each edge detected image to the reference hand-labeled image to obtain the filter parameters.

2.2.2 Ridge-based approaches

Ridge-based methods treat grayscale images as 3D elevation maps in which intensity ridges, which coincide approximately with vessel centerlines, approximate the skeleton of the tubular objects [21]. After creating the intensity map, ridge points are local peaks in the direction of maximal surface gradient, and can be obtained by tracing the intensity map from an arbitrary point, along the steepest ascent direction. Ridges are invariant to affine transformations and can be detected in different image modalities. These properties are exploited in medical image registration [22, 23].

In [14] an algorithm based on the extraction of image ridges is discussed. The ridges are used to compose primitives in the form of line elements. An image is partitioned by the line elements into patches by assigning each image pixel to the closest line element. Every line element constitutes a local coordinate frame for its corresponding patch. For every pixel, feature vectors are computed that make use of properties of the patches and line elements. The feature vectors are classified using a NN-classifier and sequential forward feature selection. The algorithm is trained and tested using the DRIVE [6] database.

2.2.3 Region growing approaches

Starting from some seed point, region growing techniques segment images by incrementally recruiting pixels to a region, on the basis of some predefined criteria. Two important segmentation criteria are *value similarity* and *spatial proximity* [24]. It is assumed that pixels that are close to each other and have similar intensity values are likely to belong to the same object. The main disadvantage of region growing approach is that it often requires user-supplied seed points. Due to the variations in image intensities and noise, region growing can result in holes and over-segmentation. Thus, it requires post-processing of the segmentation result.

2.2.4 Multi-scale approaches

Multi-scale approaches perform segmentation at various image resolutions. The main advantage of this technique is its high processing speed. Major structures (large vessels in our application domain) are extracted from low resolution images while fine structures are extracted at high resolution. Another advantage is the high robustness. After segmenting the thick structures at the low resolution, small structures, such as branches, in the neighborhood of the strong structures can be segmented at higher resolution.

M. E. Martinez-Perez et al. [25, 15] propose a blood vessels segmentation algorithm based on a multi-scale analysis. Two geometrical features based on the first and the second derivative of the intensity image, maximum gradient and principal curvature, are obtained at different scales by means of Gaussian derivative operators. A multiple pass region growing procedure is used, which progressively segments the blood vessels using the feature information together with spatial information about the eight-neighboring pixels. The algorithm works with red-free as well as fluorescein retinal images.

2.2.5 Skeleton-based approaches

Skeleton-based methods extract blood vessel centerlines. The vessel tree is created by connecting these centerlines. Different approaches are used to extract the centerline structure. Some of these methods are: (i) thresholding and then object connectivity, (ii) thresholding followed by a thinning procedure, and (iii) extraction based on graph description.

2.2.6 Mathematical morphology schemes

Morphology relates to the study of object shapes. Morphological operators (MO) apply structuring elements (SE) to images, and are typically applied to binary images but can be extended to gray-level images. *Dilation* and *erosion* are the two main MO. *Dilation* expands objects by a SE, filling holes and connecting disjoint regions. *Erosion* shrinks objects by a SE. *Closing*, dilation followed by erosion, and *opening*, erosion followed by dilation, are two further operations. Two algorithms used in medical image segmentation and related to mathematical morphology are *top hat* and *watershed* transformations. [26].

In [27], F. Zana and J. C. Klein present an algorithm that combines morphological filters and cross-curvature evaluation to segment vessel-like patterns. Blood vessel patterns in retinal fundus images are bright features defined by morphological properties: linearity, connectivity and curvature of vessels varying smoothly along the crest line. On the basis, mathematical morphology is used to highlight vessels with respect to their morphological properties. However, other patterns fit such a morphological description. In order to differentiate vessels from analogous background patterns, a cross-curvature evaluation is performed. Vessels are detected as the only features whose curvature is linearly coherent. The detection algorithm that derives directly from this modeling is based on four steps: 1) noise reduction; 2) linear pattern with Gaussian-like profile improvement; 3) cross-curvature evaluation; 4) linear filtering. The algorithm has been tested on retinal photographs of three different types: fluoroangiography, gray images obtained with a green filter, and color images with no filter. Occasionally a short preprocessing step is necessary, since the algorithm only works with bright patterns in gray level images.

2.3 Model-based approaches

We divide deformable models into two categories: parametric deformable models and geometric deformable models. These categories are discussed in detail in the next sections.

2.3.1 Active contours (Snakes)

Deformable models are model-based techniques that find object contours using parametric curves, which deform under the influence of internal and external forces. First introduced by Kass, Witkin, and Terzopoulos in 1987 [28], active contour models or *snakes* are a special case of a more general technique of matching a deformable model by means of energy minimization. Physically, a snake is a set of control points, called *snaxels*, in an image that are connected to each other. Each snaxel has an associated energy that either rises or falls depending upon the forces that act on it. These forces are known as snake's *internal* and *external* forces, respectively. *Internal* forces serve to impose smoothness constraints on the contour while *external* forces pull the snake towards the desired image features like lines and edges. We can represent the snake parametrically by $v(s) = (x(s), y(s))$, where $x(s)$ and $y(s)$ are coordinate functions and $s \in [0, 1]$. The snake's total energy is:

$$E_{snake} = \int_0^1 F_{snake}(v(s))\, ds \tag{2.1}$$

The smoothness constraint imposed by elasticity energy makes the deformable models robust to noise. The main disadvantage is that usually it requires user interaction to initialize the snake. It also requires initial parameters given by the user. Automatic snake initialization is an active ongoing research topic [29, 30].

In [19] a system inspired to the classical snakes but incorporating specific domain knowledge, such as blood vessels topological properties, is developed. This approach takes advantage also from the automatic localization of the optic disc and from the extraction and enhancement of the vascular tree centerlines. The method achieves encouraging results in the detection of arteriovenous structures. The systems performance is evaluated on the public DRIVE database.

2.3.2 Level set methods

Caselles et al. [29] and Malladi et al. [31] use the Level Set Method (LSM) approach developed by Osher and Sethian [32] and adapt it to shape recognition to model anatomical patterns. The main idea behind the Level Set Method is to represent propagating curves as the zero level set of a higher dimensional function which is given in the Eulerian coordinate system. Hence, a moving front is captured implicitly by the level set function (LSF). The advantages of this approach are:

1. It can handle complex interfaces which develop sharp corners and change their topologies during the development;
2. Intrinsic properties of the propagating front such as the curvature and normal to the curve can be easily extracted from the level set function;
3. Since the level set function is given in the Eulerian coordinate system, discrete grids can be used together with finite differences methods to obtain a numerical approximation to the solution;

4. It is easily extendable to higher dimensions.

2.4 Tracking-based approaches

Pattern recognition approaches apply local operators to the whole image. These methods require the processing of every image pixel and numerous operations per pixel. This can be very time expensive. On the other hand, tracking-based approaches work by first locating an initial point and then exploiting local image properties to trace the vascolature recursively. They only process pixels close to the vascolature, avoiding the processing of every image pixel, and so are appropriately also called "exploratory algorithms". They have several properties that make them attractive for real-time high-resolution processing, since they scale well with image size, can provide useful partial results, and are highly adaptive while being efficient.

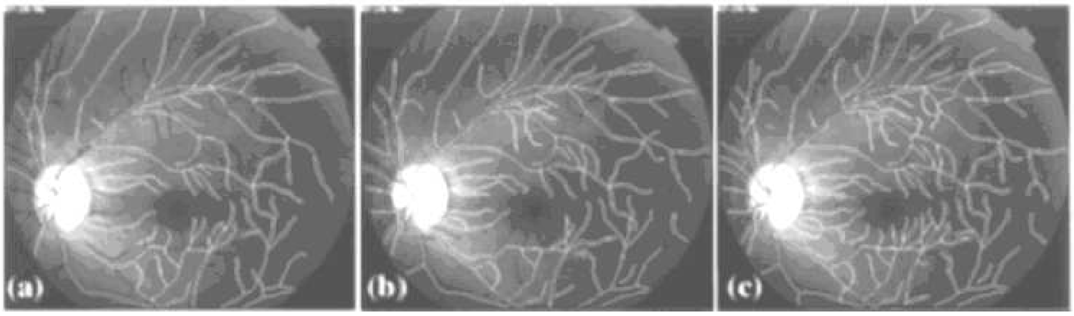

Figure 2.3: Example of segmented images using a tracking algorithm: the three images refer to results obtained using an increasing number of seeds (from (a) to (c)): we can appreciate the increasing number of extracted vessels.

Vessel tracking approaches detect vessel centerlines or boundaries by analyzing the pixels orthogonal to the tracking direction. Different methods are employed in determining vessel contours or centerlines. Edge detection operation followed by sequential tracing by incorporating connectivity information is a straightforward approach. Aylward et al. in [22] utilize *intensity ridges* to approximate the medial axes of tubular objects such as vessels. Some applications achieve sequential contour tracing by incorporating into the next step the features, such as vessel central point and search direction, detected in previous steps [33]. Fuzzy clustering is another approach to identify vessel segments. It uses linguistic descriptions like "vessel" and "nonvessel" to track vessels in retinal angiogram images. After the initial segmentation, a fuzzy tracking algorithm is applied to each candidate vessel region. Some methods utilize a model in the tracking process and incrementally segment the vessels. A more sophisticated approach to vessel tracking is the use of graph representation [34]. The segmentation process is, then, reduced to finding the optimum path in a graph representation of the image. A disadvantage of the vessel tracking approaches is that they are not fully automatic and require user intervention for selecting starting and end points.

We can distinguish three different ways to apply the tracking technique to achieve vessel segmentation [35]:

- The initial and final points of the vessel (and sometimes also the direction and the thickness) are manually inserted. Although these algorithms are very accurate, they are not suitable for the automatic real-time elaboration of fundus retina images since they need manual inputs and high processing times.
- The initial point and the direction of the vessel are manually inserted; then the algorithm traces recursively the vessel following its profile inside the image. The fact that the vessels are not necessarily connected in fundus images makes this method poorly efficient.
- The algorithm extracts in a completely automatic way the vessel network; a preliminary phase of analysis allows to set a bunch of seed points from which to begin the elaboration, that consists in the search of the vessel direction and its thickness thanks to the application of a series of filters. In detail, such filters are a set of bidimensional correlation kernels that work as:

    1. low-pass differentiator filters along the direction perpendicular to the vessel.

    2. low-pass filter along the vessel itself; they uniform the grey level of the pixels belonging to a certain set (defined by the size of the kernel) to their mean value.

2.5 Artificial intelligence-based approaches

Artificial Intelligence-based approaches (AIBA) utilize knowledge to guide the segmentation process and to extract vessel structures. Different types of knowledge are employed in different systems from various sources. Possible knowledge sources are the properties of the image acquisition technique, such as cine-angiography, digital subtraction angiography (DSA), computed tomography (CT), magnetic resonance imaging (MRI), and magnetic resonance angiography (MRA). Some applications utilize a general blood vessel model as a knowledge source. Smets et al. [36] encode general knowledge about appearance of blood vessels in the form of 11 rules (e.g., vessels have high intensity center lines, comprise high intensity regions bordered by parallel edges, etc.). Stansfield [37] applies a domain-dependent knowledge of anatomy to interpret cardiac angiograms in the high-level stages. According to Stansfield, “Anatomical knowledge is embodied within the system in the form of spatial relations between objects and the expected characteristics of the objects themselves". Knowledge-based systems exploit a priori knowledge of the anatomical structure. These systems employ some low-level image processing algorithms, such as thresholding, thinning, and linking, while guiding the segmentation process using high-level knowledge. AIBA performs well in terms of accuracy, but the computational complexity is much higher than for other methods.

2.6 Neural network-based approaches

Neural networks are used to simulate biological learning and are widely used in pattern recognition. Neural nets implement basically a classification approach. The network is a collection of elementary processor (nodes). Each node takes a number of inputs, performs elementary computations, and generates a single output. Each node is assigned a weight and the output is a function of weighted sum of the inputs. These weights are learned through training and then used in the recognition.

Back-propagation algorithm is a widely used learning algorithm. One problem associated to learning is that learning depends on the training data set. The size of the training data set affects the learning process. The training procedure should be rerun each time new training data is added to the set. Since the aforementioned neural networks require a training data set, the learning process is a supervised learning. A different class of neural networks are self-teaching and do not depend on training data set for the learning. The best known of these class of neural networks is Kohonen feature maps or [38] self-organizing networks. Interested readers are referred to [39, 40], and Haykin [41] for more information on neural networks.

In medical imaging, neural networks are mainly used as a classification method where the system is trained with a set of medical images and the target image is segmented using the trained system. One of the advantages that make neural networks attractive in medical image segmentation is their ability to use nonlinear classification boundaries obtained during the training of the network. One of the disadvantages is that they need to train every time a new feature is introduced. Another limitation is the difficulty of debugging the performance of the network.

2.7 Wavelets

To increase the contrast between the background and the areas of the image with highest variations of the grey levels (e.g. the areas corresponding to the blood vessels) it is possible to apply specific transformations to the image itself. An easy one is the so called Haar transform, that is actually an averaging and differencing operation. It operates by transforming a $1 \times N$ array of values into a $1 \times N$ array of results. The first $[1...N/2]$ elements of the array are the averages of pairs of the $[1...N]$ original elements, and the following $[N/2+1...N]$ elements in the array are the detail elements from the $[1...N]$ original elements. For the first pair of elements in the initial array, $[x_1, x_2, ...]$, the first element in the result array is $(x_1+x_2)/2$, and the corresponding detail element at position N/2 is $(x_1+x_2)/2-x_1$. As the average element is equidistant from both x_1 and x_2, to restore the initial array we simply subtract the detail element from the average element (this gives us x_1) and add the detail element from the average, to restore x_2.

For 2-dimensional images the transform operation is performed on all rows of the image and then again on all columns of the output from the first application of the transform. In the typical transform applied to images using standard inverted cartesian geometry, the average elements are stored in the top left quadrant of the input image and detail elements stored in the remaining 3 quadrants of the image. The average elements from the top left corner are then processed in the same way as the entire image was to begin with, to perform the second level of the transform. This process can be repeated as many times as desired, each time further reducing the size and resolution of the output image. Figure 2.4 sketches the way how the Haar transform works, while an example is given in Figure 2.5.

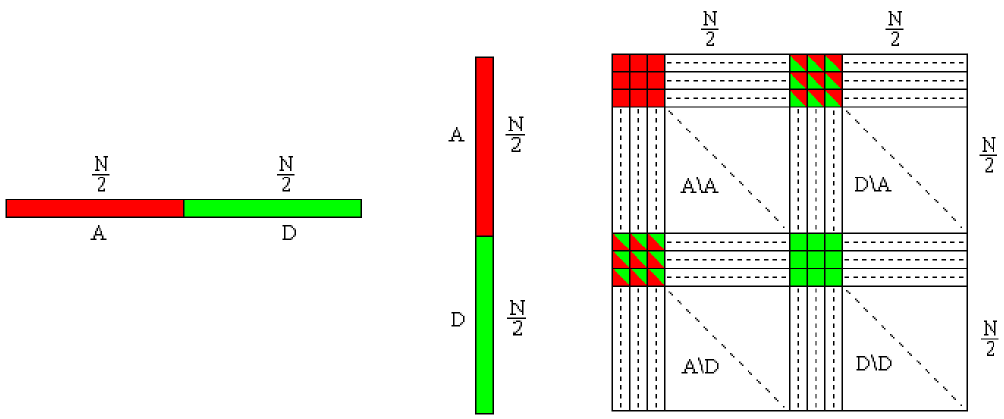

Figure 2.4: Haar transform applied to vectors and matrixes: the two vectors at the left represent the application of the Haar transformation on row vectors and column vectors (average elements in red, detail elements in green). At the right, the transformation of a matrix NxN is represented, first by row, then by columns of the matrix resulting from the first phase of the transform. The colors point out the type and the order of the result. We get so a matrix NxN that contains four images, every of dimension N/2 x N/2, each one being the result of a different transformation of the original image.

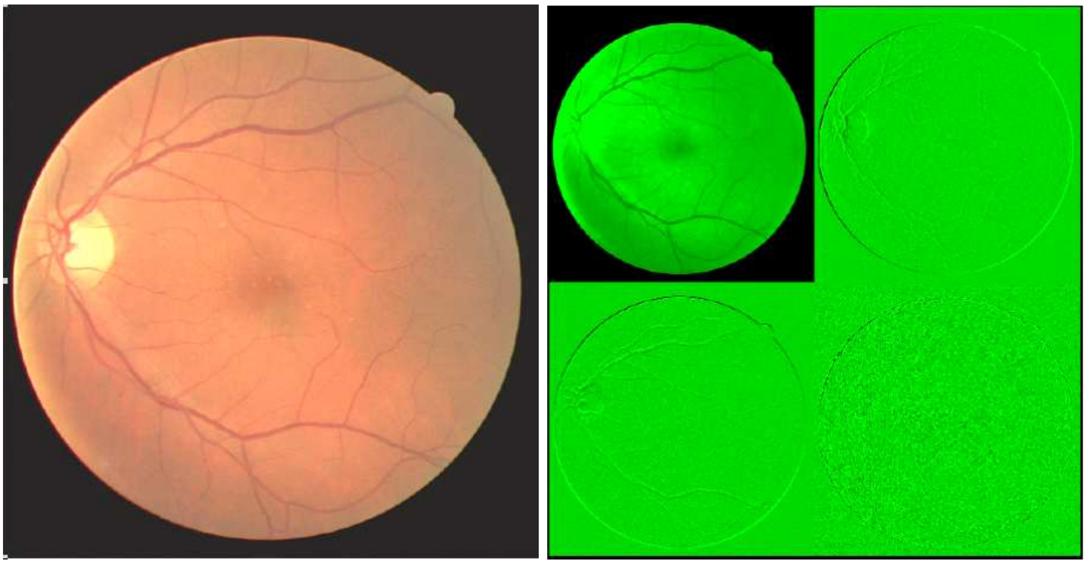

(a) (b)

Figure 2.5: An example of application of the Haar transform to a typical fundus retina image.

In [42] a method for automated segmentation of the vascolature in retinal images is presented. The method produces segmentations by classifying each image pixel as vessel or nonvessel, based on a pixel's feature vector. Feature vectors are composed of the pixel's intensity and two-dimensional wavelet transform outputs taken at multiple scales. The wavelet is capable of tuning to specific frequencies, thus allowing noise filtering and vessel enhancement in a single step. A Bayesian classifier is used with class-conditional probability density functions (likelihoods) described as Gaussian mixtures, yielding a fast classification, while being able to model complex decision surfaces. The probability distributions are estimated on the basis of a training set of labeled pixels obtained from the manual segmentations stored in the DRIVE databases.

Chapter 3

The multiscale analysis

In this thesis we develope a novel algorithm for vessel segmentation in fundus retina images. The algorithm is modular and is made up of two fundamental blocks. The former is devoted to vessel enhancement involving "*multiscale theory*". Two cases are studied: linear multiscale and an edge-preserving non-linear multiscale. In this chapter we deal with the multiscale paradigm and we introduce a proper mathematical framework based on both a differential and a variational approach. In the last part of this chapter we use this framework to better understand some general properties of the multiscale analysis. In the next two chapters we will use the knowledges introduced in this chapter to clarify the behaviour of the multiscale cases that will be introduced.

As outlined in the previous chapters, computer-based analysis for automated segmentation of blood vessels in retinal images helps eye care specialists to screen large populations for vessel abnormalities. The width of retinal vessels can vary from very large to very small. This property of retinal images makes a completely automated vessel segmentation very difficult. Multiscale techniques have been developed to isolate information about objects in an image by looking for geometric features at different scales, i.e. with different sizes [43].

Within this framework, we pass from the original image to smoothed versions, which still contain significant information. The main parameter of this preliminary transform is the "scale", a general parameter which measures the degree of smoothing, or more trivially, the size of the neighbourhoods which are used to give an estimate of the brightness of the picture at a given point. The so-called "multiscale analysis" tends to give less local and therefore more reliable information on the grey level than the original fluctuating "pixel".

If we want to extract a particular feature from an image, such as the vessels, we apply the feature detector at all scales, and then select the scale corresponding to local maxima, with respect to the scales, of measures of the feature strength. Lindeberg in [44] has shown empirically that for a tube-like feature as a vessel, a local maximum can be found at the scale corresponding to vessel width.

Mathematically, we define without loss of generality the "scale space" of an image $I(x,y)$ for a "multiscale analysis" T_t the sequence of pictures $I(x,y,t) = (T_t I)(x,y)$ that we obtain by applying the operator T_t to I. The operator T_t depend only on one parameter t. For example, if we consider the classical multiscale analysis due to the convolution of an image I with gaussian kernels with different standard deviations σ

$$I(x,y;\sigma) = (T_\sigma I)(x,y) = G_\sigma * I \tag{3.1}$$

with

$$G_\sigma = G(x,y;\sigma) = \frac{1}{2\pi\sigma^2} \quad e^{-\frac{x^2+y^2}{2\sigma^2}} \tag{3.2}$$

in this case we have $t \equiv \sigma$. In other cases, if we refer to a multiscale analysis modeled by a diffusion Partial Differential Equation (PDE), the parameter t corresponds to the diffusion time.

Roughly speaking, $T_t I$ can be thought as a semi-local version of I where a neighbourhood of size t around (x,y) has been exploited for determining the value of $I(x,y,t)$. If T_t is a linear operator, we have **linear multiscale analysis**, otherwise we have **non-linear multiscale analysis**. An example of image at a certain scale in shown in Figure 3.1.

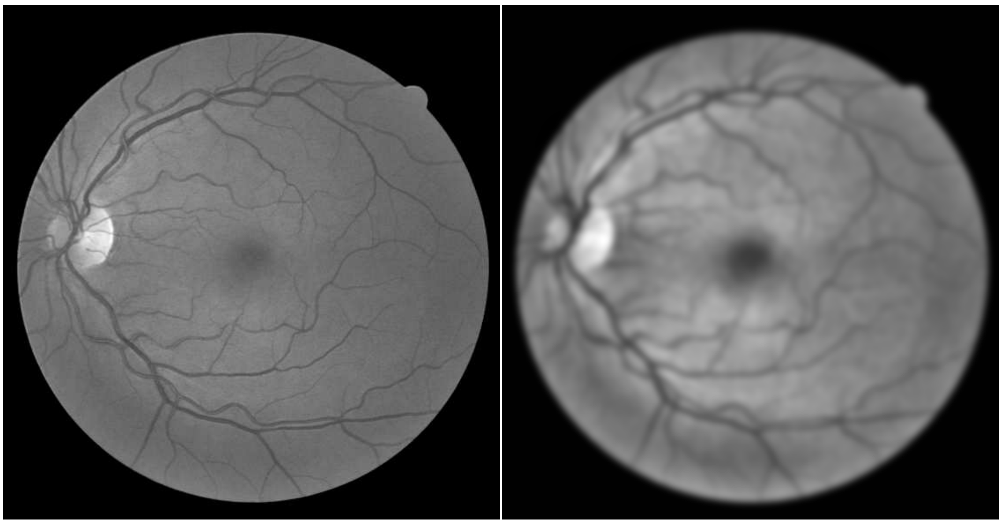

(a) (b)

Figure 3.1: (a) The image $I(x,y)$ (b) The same image at a certain scale.

We said that multiscale analysis is useful in vessel extraction tasks. Different algorithms have been proposed in the literature about this topic (see for istance [15, 45, 46]). In the next two chapters we will describe vessel enhancement algorithms based on this kind of analysis. In this chapter we detail the multiscale approach introducing some properties or axioms. Then we show how, by satisfying these axioms, every sequence of pictures $I(x, y, t) = (T_t I)(x, y)$ can be related to the solution of a second order PDE:

$$\frac{\partial I}{\partial t} = F(\nabla I, H(I)) \tag{3.3}$$

where ∇I is the image gradient and $H(I)$ the Hessian matrix (see Section 1.5).

In the literature, the first description of a multiscale analysis referred to an operator T_t and to linear scale spaces. Alvarez et al in [47] gave an axiomatic description of the multiscale properties and proved the relationship between operator-based multiscale analysis and PDEs, as introduced with Equation (3.3).

The results introduced in the first part of this chapter are valid for generic PDEs. In the second part of this chapter, we deal only with the so called *divercenge form*, a particular diffusion equation also used in image processing. This equation allows us to establish a link between the differential form and the *variational form*. We will define the mathematical framework for a variational description of multiscale analysis.

We rewrite then the equations given in the divergence form using an equivalent formulation, known as *oriented 1D Laplacians form*, which allows us to easily point out some characteristics of the diffusion equation we are going to work with.

3.1 Axioms of multiscale analysis

Alvarez et al in [47] introduced an axiomatic framework for the use of PDE in multiscale analysis models. In particular they formally stated and proved that PDEs are associated to multiscale analysis operators T_t which satisfy a series of formal properties, or axioms. An overview of these axioms is presented in this section. We introduce and briefly describe them, without the aim of being exhaustive. The first six axioms (strong and weak causality, comparison principle, grey-level-shift invariance, grey-scale invariance and translation invariance) state some desiderable properties from the vision theory point of view. The last three axioms (generator, regularity, locality) refer to strictly mathematical properties. They are necessary in [47] to demonstrate the relationship between operators T_t and PDEs.

3.1.1 Causality

We first consider an axiom, which in vision theory is called "causality" property, or "pyramidal architecture" property. This axioms states that T_t can be computed from T_s for any $s \leq t$, and T_0 is the identity. This is natural, since a coarser analysis of the original picture is likely to be deduced from a finer one without any dependence upon the original picture. Of course, the finest picture analysis is the identity.

A strong version of this property is:

[Strong causality] $T_0(I) = I$, $T_s \circ T_t(I) = T_{s+t}(I)$ *on* $\Re^2$, *for all* $s, t \geq 0$ *and* I.

If [Strong causality] is satisfied, the visual process is reduced to a single loop, if the scales are discretized. Indeed, T_t is equivalent to the n-th iteration of $T_{\frac{t}{n}}$. A weaker version of the pyramidal architecture hypothesis is the following: we include $T_t = T_{t,0}$ in a family of transition operators $T_{s,t}$ indexed by $0 \leq s, t < \infty$ and satisfying

[Weak causality] $T_{t+s} = T_{t+s,s} \circ T_s$ *for all* $0 \leq s, t < \infty$.

In order to get back to [Strong causality], one needs to assume that $T_{t+s,s} = T_{t,0}$. From the viewpoint of the theory of perception, causality in general is a coherent hypothesis, if the image perceptual analysis consists in a sequence of filters which are applied sequentially. Since new images are constantly arriving at the retina, the image-analysis process is thought of as a flow of the picture through different filters, each associated with a scale t.

3.1.2 Comparison principle

The comparison principle is an obvious order-preserving property (the "maximum principle"). It means that no enhancement is made, but just a smoothing of the original image. Thus if one image G is everywhere brighter than another image I, this ordering is preserved by the operator T_t

[Comparison principle] $T_t(I) \leq T_t(G)$ *on* $\Re^2$ *for all* $t \geq 0$ *and* I, G *such that* $I \leq G$.

This axiom is equivalent, in the case where T_t is a linear filter defined by $T_t I = I * F_t$, to the inequality $F_t \geq 0$. Thus, this axiom is the nonlinear generalization of a nonnegative smoothing kernel.

3.1.3 Grey scale invariance

This axiom and the next one are called the “morphological axioms” and are well-known in mathematical morphology. They state that image analysis must be invariant under fluctuations of light and under changes of position, orientation and scale of the planar shapes.

In the case of digital pictures, many electronic devices are applied successively to an image before its arrival at the human eye or at some automatic image-analysis device: since the grey scale of the resulting image has been changed by each device, the only sound assumption about the information-preserving properties of the whole chain of captors and transmittors is that they might preserve the order of grey levels. In other terms, if some point or some region was brighter than an another in the original picture, this order should be preserved in the final picture.

We begin by stating that the image analysis must be independent of the (arbitrary) grey-level scale. In the following, we shall always assume the following weak form of this axiom:

[Grey-level-shift invariance] $T_t(0) = 0$, $T_t(I + C) = T_t(I) + C$ for any I and any constant C.

This axiom means that no a priori assumption is made about the range of brightness of a picture to be observed. Of course, this is not absolutely true for natural or artificial photosensitive systems. It is however true that the interpretation of a photograph is widely independent of its exposure time: the photograph can be dark or light and yet be identified as essentially the same picture. This axiom is equivalent, in the case where T_t is a linear filter defined by $T_t I = I * F_t$, to the requirement that $\int F_t(x)\,dx = 1$.

The strong form of the first morphological axiom is

[Grey-scale invariance] $T_t\left(h(I)\right) = h\left(T_t(I)\right)$ for all I and all $t \geq 0$, where h is any nondecreasing real function.

The function h is simply an order-preserving rearrangement of the grey levels. Notice that the second relation of [Grey-level-shift invariance] is a particular case of [Grey-scale invariance].

3.1.4 Translation invariance

Now we introduce an axiom which states that all points of the space are a priori equivalent:

[Translation invariance] $T_t\left(\tau_{\boldsymbol{h}} \cdot I\right) = \tau_{\boldsymbol{h}}\left(T_t \cdot I\right)$ *for all* $\boldsymbol{h}$ *in* $\Re^2$, $t \geq 0$, *where* $\left(\tau_{\boldsymbol{h}} \cdot I\right)(x, y) = I\left(x + h_1, y + h_2\right)$.

In other words, there is no a priori knowledge about location of any feature of the picture.

3.1.5 Regularity, Locality and Generator

We present three strictly mathematical properties. These axioms are necessary condition in the demonstration of the relationship between the operators T_t and PDEs. We shortly introduce them without the aim of being exhaustive, for more details please refer to [47].

We define, the so called infinitesimal generator A for the operator T_t as the following limit, provided that it exists:

[Generator] $(T_t I - I)/t \rightarrow A[I]$ *uniformly on* $\Re^N$, *as* $t \rightarrow 0^+$ *for smooth* I.

A way of justifying [Generator] is to deduce it from axioms more natural from the viewpoint of perception. An example of such an axiom, which, combined with the other axioms of the theory, implies [Generator] is

[Regularity] $\|T_t(I + hG) - (T_t(I) + hG)\|_\infty \leq Cht$ *for all* h, t *in* $[0, 1]$, *for smooth* I *and* G, *where of course* C *depends on* I *and* G.

This last axiom states a natural assumption of continuity of T_t and is therefore a strong justification for the existence of an infinitesimal generator for the multiscale analysis. We next require an axiom on the local character of the multiscale analysis T_t for t small (and therefore the local character of the infinitesimal generator A):

[Locality] $\left\{T_t(I) - T_t(G)\right\}(x) = o(t)$ *as* $t \rightarrow 0^+$, *for all smoth* I *and* G *such that* $D^\alpha I(x, y) = D^\alpha G(x, y)$ *for all* $|\alpha| \geq 0$ *and for all* x.

where D^α denotes every measure associated with a derivative of α-th order. For example, if $\alpha = 1$, we can have $D^\alpha I = \frac{\partial I}{\partial x}$ or $D^\alpha I = \frac{\partial I}{\partial y}$ or $D^\alpha I = \|\nabla I\|$. Roughly speaking, this last axiom means that the value of $T_t(I)$ for t small, at any point x, is determined by the behaviour of I near x.

3.2 Differential form of regular multiscale analysis operators

Now we introduce an important result that allows us to express the commonly used multiscale analysis in a different way: we will report a theorem, proved in [47], stating that the main multiscale image processing models can be related to parabolic partial differential equations (PDEs) of order 2.

First of all, it has been proved that if T_t is a multiscale analysis that satisfy the "architectural" conditions [Strong causality], [Regularity], [Locality], together with [Comparison principle], and the morphological conditions [Translation invariance] and [Grey-level-shift invariance], then there exists a "generator" A for that operator T_t

Then, considering the previous axioms and also [Locality], it has been proved that there exists a continuous function F such that, for any given picture I, $I(x, y, t) = T_t I$ satisfies

$$\frac{\partial I}{\partial t} = F(\nabla I, H(I)) \tag{3.4}$$

where F is the infinitesimal generator for T_t (i.e. we have $F(\nabla I, H(I)) \equiv A[I]$).

Conversely, any partial differential equation of the kind of Equation (3.4) corresponds to a multiscale analysis satisfying the above mentioned axioms.

To better understand the influence of each axiom on the result, we show what would happen if we relax some of the axioms necessary for Equation (3.4). For example, if instead of the [Strong causality], we have the [Weak causality], and the obvious adaptation of the other axioms to $T_{t,s}$, the same result has been proved with a time-dependent F:

$$\frac{\partial I}{\partial t} = F(\nabla I, H(I), t) \tag{3.5}$$

Moreover, for example, if we remove [Translation invariance], the equation becomes space-dependent, and F has the form

$$\frac{\partial I}{\partial t} = F(\nabla I, H(I), x) \tag{3.6}$$

Notice that, in the same way, a dependence of F on I, such as

$$\frac{\partial I}{\partial t} = F(\nabla I, H(I), I, t) \tag{3.7}$$

only contradicts [Grey-level-shift invariance].

We remark that now the "time" t is the scale parameter: larger values of t lead to simpler representations. According to the framework defined above we can observe that multiscale analysis realizes (in general) a **nonlinear diffusion filtering**: the image is simplified step by step and its variations are minimized. In the literature this simplification process of a given image is called **regularization**.

3.2.1 The divergence form

During the last two decades, nonlinear diffusion filters have become a powerful and well-founded tool in multiscale image analysis. Many papers have appeared proposing different models, investigating their theorethical foundations, and describing interesting applications. We focus on approaches in **divergence form**, a particular case of Equation (3.4). In particular, this form is interesting since will allow us to establish in the next section a link between the differential form and an alternative variational definition of a similar problem.

We have referred to a given image $I(x, y)$ calling $I(x, y, t)$ the scale space related to it. For the sake of clarity in the following we rename the original image $I(x, y)$ as $I_0(x, y)$ to more clearly distinguish this from $I(x, y, t)$. From now on, we will be interested in regularization due to partial differential equation of the class:

$$\frac{\partial I}{\partial t} = \nabla \left(g\left(\|\nabla I\|\right) \nabla I\right) \tag{3.8}$$

on $\Omega \times (0, \infty)$ with the original image as initial state and homogeneous Neumann boundary conditions:

$$I(x, y, 0) = I_0(x, y) \ on\ \Omega \tag{3.9}$$

$$\frac{\partial I}{\partial \mathbf{n}} = 0 \ on\ \partial\Omega \times (0, \infty) \tag{3.10}$$

where $\mathbf{n}$ denotes the normal to the image boundary $\partial\Omega$.

The function $g\left(\|\nabla I\|\right)$ is commonly called **diffusivity**. It is a not-increasing positive function, that basically, in the non linear case, characterizes the diffusion behaviour by blurring low-contrast regions much more than high-contrast locations (the edge of the image). The function $\|\nabla I\|\, g\left(\|\nabla I\|\right)$ is called **flux**. For reasons that will be clear only in Section 3.4, we have to choose the function g so that to have a non-negative flux for every value $\|\nabla I\|$.

For such a class of equations the following properties can be established:

1. (Well-posedness and smooth results)

   There exists a unique solution $I(x,y,t)$ in $C^{\infty}\left(\Omega \times (0,\infty)\right)$ and it depends continuously on $I_0(x,y)$ with respect to the $L^2(\Omega)$ norm.

2. (Average grey level invariance)

   The average grey level of the original image

   $$\mu := \frac{1}{|\Omega|} \int_{\omega} I_0(x,y)\, dxdy \tag{3.11}$$

   is not affected by non linear diffusion filtering:

   $$\frac{1}{|\Omega|} \int_{\omega} I(x,y,t)\, dxdy = \mu \tag{3.12}$$

   for all $t > 0$

3. (Convergence to a constant steady state)

   $\lim_{t \to \infty} I(x,y,t) = \mu$ *in* $L^p(\Omega)$, $1 \le p < \infty$

The existence, uniqueness and regularity is proved in [48], the other results are proved in [49].

Continuous dependence of the solution on the initial image is of significant practical importance, since it guarantees stability under perturbations. This is relevant when considering stereo images, image sequences or slices from medical CT (Computed Tomography) or MR (Magnetic Resonance) sequences, since we know that similar images remain similar after filtering.

Average grey level invariance is a property which distinguishes nonlinear diffusion filtering from other PDE-based image processing techniques, such as mean curvature motion [50]. The latter is not in divergence form and, thus, can not be conservative. Average grey level invariance is required in some segmentation algorithms such as the

Hyperstack [51].

The third property tells us that, for $t \to \infty$, diffusion filtering tends to a constant image with the same average grey level of I_0.

3.3 The variational form

Variational methods constitute an interesting alternative to nonlinear diffusion filters. The idea behind regularization with variational methods is the following. Image regularization can be done by minimizing energy functionals measuring the global image variations. The acknowledged aim is to suppress low image variations mainly due to noise, while preserving the high ones representing the image contours. Typical variational methods for image regularization (such as [52, 53, 54, 55, 56]) provide a filtered version of some given image I_0 as the minimizer I^* of

$$\begin{aligned} E\left(I(x,y;\tau)\right) &= \int_\Omega \Psi(I, I_x, I_y)\, dxdy \\ &= \int_\Omega \Psi_1 + \tau \Psi_2\, dxdy \\ &= \int_\Omega (I - I_0)^2 + \tau \Phi\left(\|\nabla I\left(x,y\right)\|\right)\, dxdy \end{aligned} \tag{3.13}$$

where $\Phi(s) : \Re \to \Re$ is an increasing convex function for $s > 0$ ($\Phi' \geq 0$ and $\Phi'' \geq 0$). So we want to find the function $I^*(x, y; \tau)$ that minimizes Equation (3.13):

$$E\left(I^*\right) = \min_I E\left(I\right) \tag{3.14}$$

The first term Ψ_1 in the integral is commonly called **fidelity term** and encourages similarity between the regularized image and the original one, while the second term Ψ_2 is named **regularization term** and rewards smoothness, i.e. penalizes the presence of edges in the image. The smoothness weight $\tau > 0$ is called **regularization parameter**.

For this class of regularization methods one can establish a similar well-posedness and scale-space framework as for nonlinear diffusion filtering, if one considers the regularization parameter $\tau > 0$ as scale. In [57] the following properties have been proved:

1. (Well-posedness and regularity)

Let $I_0 \in L^\infty(\Omega)$. Then the functional Equation (3.13) has a unique minimizer I^* in the Sobolev space $H^1(\Omega)$. Moreover, $I^* \in H^2(\Omega)$ and $\|I^*\|_{L^2(\Omega)}$ depends continuously on τ

2. (Average grey level invariance)

The average grey level

$$\mu := \frac{1}{|\Omega|} \int_\omega I_0(x, y)\, dxdy \tag{3.15}$$

remains constant under regularization:

$$\frac{1}{|\Omega|} \int_\omega I^*(x, y; \tau)\, dxdy = \mu \tag{3.16}$$

for all $\tau > 0$

3. (Convergence to a constant image for $\tau \to \infty$)

$\lim_{\tau \to \infty} \|I^*(x, y; \tau) - \mu\|_{L^p(\Omega)}$ *for any* $1 \leq p < \infty$

Let us now give an intuitive reason for this large amount of structural similarities between diffusion filters and regularization methods.

3.3.1 The Euler-Lagrange equations

Finding the function I^* that minimizes the functional $E(I)$ is not a trivial problem. Nevertheless, the *Euler-Lagrange equations* give a necessary condition that must be fulfilled by $I^*(x, y; \tau)$ to reach a minimum of $E(I)$.

Let us define a function F:

$$F = \frac{\partial}{\partial I}\left[(I - I_0)^2\right] - \tau \frac{\partial}{\partial x}\frac{\partial \Phi}{\partial I_x} - \tau \frac{\partial}{\partial y}\frac{\partial \Phi}{\partial I_y} \tag{3.17}$$

The solution of the variational problem can be found out solving

$$F = 0 \tag{3.18}$$

We calculate now more explicity each term of F:

1.
$$\frac{\partial}{\partial I}(I - I_0)^2 = 2(I - I_0) \tag{3.19}$$

2.

$$\begin{aligned}\frac{\partial}{\partial x}\frac{\partial \Phi}{\partial I_x} &= \tau \frac{\partial}{\partial x}\frac{\partial \Phi(\|\nabla I(x,y)\|)}{\partial \|\nabla I(x,y)\|}\frac{\partial \|\nabla I(x,y)\|}{\partial I_x} \\ &= \tau \frac{\partial}{\partial x}\left[\Phi' \frac{I_x}{\sqrt{I_x^2 + I_x^2}}\right] \end{aligned} \tag{3.20}$$

3.

$$\begin{aligned}\frac{\partial}{\partial y}\frac{\partial \Phi}{\partial I_y} &= \tau \frac{\partial}{\partial y}\frac{\partial \Phi(\|\nabla I(x,y)\|)}{\partial \|\nabla I(x,y)\|}\frac{\partial \|\nabla I(x,y)\|}{\partial I_y} \\ &= \tau \frac{\partial}{\partial y}\left[\Phi' \frac{I_y}{\sqrt{I_y^2 + I_y^2}}\right] \end{aligned} \tag{3.21}$$

Concluding, we have:

$$\begin{aligned} F &= 2(I - I_0) - \tau \frac{\partial}{\partial x}\left[\frac{\Phi'}{\|\nabla I\|}\nabla I_x\right] - \tau \frac{\partial}{\partial y}\left[\frac{\Phi'}{\|\nabla I\|}\nabla I_y\right] \\ &= 2(I - I_0) - \tau \nabla \left(\frac{\Phi'}{\|\nabla I\|}\nabla I\right) \end{aligned} \tag{3.22}$$

On the basis of this results we can introduce a link between the divergence and the variational form, as explained in the next section.

3.3.2 Link between variational and divergence form

We have seen that the solution of a variational problem can be obtained by solving

$$F = 0 \tag{3.23}$$

that can be rewritten as follows:

$$\frac{(I - I_0)}{\tau} = \frac{1}{2}\nabla \left(\frac{\Phi'}{\|\nabla I\|}\nabla I\right) \tag{3.24}$$

This can be thought of as a fully implicit time discretization of the diffusion filter

$$\frac{\partial I}{\partial t} = \frac{1}{2}\nabla \left(g\left(\|\nabla I\|\right)\nabla I\right) \tag{3.25}$$

with a time discretization step of size τ and

$$g\left(\|\nabla I\|\right) \equiv \frac{\Phi'}{\|\nabla I\|} \tag{3.26}$$

One may thus regard our well-posedness and multiscale framework for regularization methods as a discrete-time framework for diffusion filtering, estabilishing a tight relationship between $I(x, y, \tau)$ and $I(x, y, t)$ [58]; in other words, we can write:

$$I(x, y; \tau) \cong I(x, y, t) \tag{3.27}$$

Moreover, to avoid the direct and difficult solution of Equation (3.22), a classic iterative method is used: the *gradient descent*. Actually, Equation (3.22) can be considered as the gradient of the functional $E(I)$. Starting from I_0 as initial condition and following the opposite direction of this gradient leads to a local minimizer I^{**} of E:

$$\begin{cases} I_{(t=0)} = I_0 \\ \frac{\partial I}{\partial t} = -F \end{cases} \tag{3.28}$$

Note that this PDE evolution has been parameterized with an (artificial) time variable t. It describes the continuous progression of the function I until it minimizes E(I). Then the PDE speed vanishes: $\partial I/\partial t = 0$.

For $t \to \infty$ I tends to a steady state I^{**} that is a local minimizer of $E(I)$. It has been proved that if Φ is a *convex function*, we have only one minimum and then the minimum obtained in this way is the global one ($I^{**} \equiv I^{*}$). More in the general, if Φ is *not convex*, the starting point I_0 must be carefully chosen, ideally near the global minimum of the functional $E(I)$. Choosing different initializations I_0 may lead to different results (different local minima).

Concluding, the Euler-Lagrange equations make the link between differential form and variational form (through Equation (3.26)) in image regularization. Generally, we will be more interested in the gradient descent itself than in the functional minimization, and we will often use the term **PDE flow** to describe such evolutions. The reader is referred to [59] for an exhaustive theory about the calculus of variations.

3.4 The oriented 1D Laplacians form

The PDEs in the divergence form are widely used in the literature and are useful if we want to work with a framework strictly related to equivalent variational formulations, but don't give us direct information about the diffusion behaviour. We can more directly understand it if we rearrange the diffusion equations we have considered until now in a new equivalent form, called **oriented 1D Laplacians form**. In other words we are interested in establishing a further correspondence between the previous definition of a differential image processing problem in the divergence form

$$\frac{\partial I}{\partial t} = \nabla\left(\frac{\Phi\prime}{\|\nabla I\|}\nabla I\right) := \nabla\left(g\left(\|\nabla I\|\right)\nabla I\right) \tag{3.29}$$

and the following equation:

$$\frac{\partial I}{\partial t} = c_1 I_{zz} + c_2 I_{vv} \tag{3.30}$$

being I_{dd} the second derivative of I along the generic direction $\mathbf{d} = [d_x, d_y]$

$$I_{dd} := \left(\mathbf{d}^T \boldsymbol{H}\right)\mathbf{d} \tag{3.31}$$

and $\boldsymbol{H}$ the Hessian matrix.

This is the so called oriented 1D Laplacians form, that was firstly introduced to describe the behaviour of the Perona-Malik diffusion equation [60, 61]. Roughly speaking, Equation (3.30) can be interpreted as the sum of two coexistent and oriented "heat flows" (recalling a sound analogy with the heat equation $\partial I/\partial t = \nabla^2 I = I_{xx} + I_{yy}$) that smooth the image along the directions $\mathbf{z}$ and $\mathbf{v}$, respectively, by weighing the two flows with coefficients the c_1 and c_2.

In our case, Equation (3.29) is equivalent to Equation (3.30) if:

1. $c_1 := g$
2. $c_2 := g + \|\nabla I\|\, g'$
3. $\mathbf{z} := \frac{\nabla_\perp I}{\|\nabla I\|}$
4. $\mathbf{v} := \frac{\nabla I}{\|\nabla I\|}$

In Appendix A we show the proof of this result.

The unit vectors $\mathbf{z}$ and $\mathbf{v}$ correspond respectively to the directions *orthogonal* and *parallel* to the gradient. Note that $\mathbf{z}$ is everywhere tangent to the isolevel lines $I(x,y) = a$ (for every fixed t) of the contours in the image. The set $(\mathbf{z},\mathbf{v})$ is then a moving orthonomal basis whose configuration depends on the current point coordinate $\mathbf{x} = (x,y)$ (Figure 3.2)

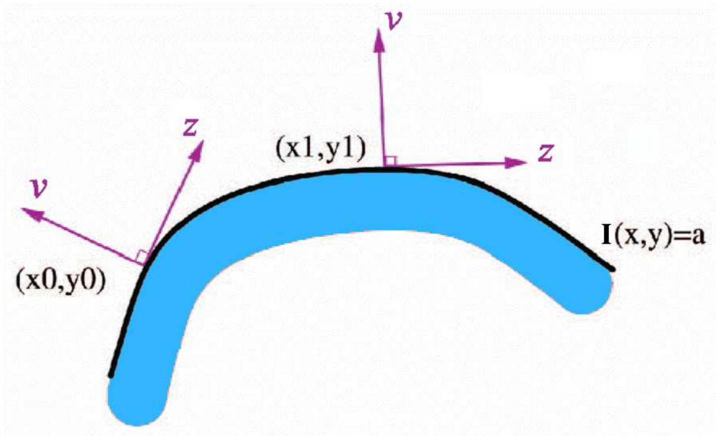

Figure 3.2: An image contour and its moving vector basis ($\mathbf{z}$,$\mathbf{v}$)

In conclusion, the values $(\mathbf{z},\mathbf{v},c_1,c_2)$ define the local geometry of the diffusion process. In the next subsection we will use the oriented 1D Laplacians form to mathematically characterize some properties of the diffusion according to the framework described to now.

3.4.1 Link between variational and oriented 1d Laplacians form

Since it exists a link between the variational form and the divergence form and a link between the divergence form and the oriented 1D Laplacians form, we can establish a direct link between the variational form and the oriented 1D Laplacians form. In particular, this will allow us to understand why at the beginning of Section 3.3 we have imposed to the regularization term of the functional Equation (3.13) to be convex. Moreover it will allow us to understand why we have imposed to the flux associated to the PDE in the divergence form to be non-negative.

Starting from the definitions of c_1 and c_2 introduced in the previous section and considering Equation (3.26) we have:

$$c_1 = g \quad = \quad \frac{1}{2}\frac{\Phi'}{\|\nabla I\|}$$

$$
\begin{aligned}
c_2 = g + \delta g' &= \frac{1}{2}\frac{\Phi'}{\|\nabla I\|} + \frac{1}{2}\|\nabla I\|\left[\frac{\partial}{\partial\|\nabla I\|}\left(\frac{\Phi'}{\|\nabla I\|}\right)\right] \\
&= \frac{1}{2}\frac{\Phi'}{\|\nabla I\|} + \frac{1}{2}\|\nabla I\|\left[\frac{\|\nabla I\|\Phi'' - \Phi'}{\|\nabla I\|^2}\right] \\
&= \frac{1}{2}\Phi'' \qquad (3.32)
\end{aligned}
$$

These results point out the link between the variational representation (introduced with Equation (3.13)) and the oriented 1D Laplacians one.

These results are useful to fix up the conditions that let us to avoid *inverse diffusion*, an *unstable process* that *enhances* image features, and among these the noise. If it happens, no uniqueness of the solution and no stability of the process can be expected.

We do not have inverse diffusion when:

1. $c_1 \geq 0 \Rightarrow \Phi' \geq 0$
2. $c_2 \geq 0 \Rightarrow \Phi'' \geq 0$

The specified equivalencies hold by considering the range $\delta = \|\nabla I\| > 0$.

To avoid inverse diffusion the function $\Phi(\delta)$ has to be monotonically increasing and convex, according to what stated at the beginning of Section 3.3. Moreover, since $\Phi' = \delta g(\delta)$, we have also to impose that the flux should be non-negative, according to what stated in Section 3.2.1

3.4.2 About isotropic diffusion

Concluding, we want to show explicitly under which conditions we have the so called *isotropic diffusion*. A diffusion is named "isotropic" if

$$c_1 = c_2 \qquad (3.33)$$

Considering the already known results

$$
\begin{aligned}
c_1 &:= g \\
c_2 &:= g + \|\nabla I\| g' \qquad (3.34)
\end{aligned}
$$

then Equation (3.33) is equivalent to

$$\begin{aligned} g &= g + \|\nabla I\| \, g' \\ &\Rightarrow \; g' = 0 \\ &\Rightarrow \; g = K \qquad \forall K \in \Re^{+} \end{aligned} \tag{3.35}$$

In this case the magnitude of K has effect only on the speed of the diffusion but not on its nature. We can set $K = 1$ without loss of generality. Then, according to Equation (3.8), the only PDE corresponding to an isotropic diffusion is:

$$\frac{\partial I}{\partial t} = \nabla(1\nabla) = \nabla^2 I \tag{3.36}$$

This the so called heat equation, that will be recalled in the next chapter. All the other kinds of PDEs, in the divergence form, known in the literature realize the so called *anisotropic diffusion*.

Please note that in this thesis, we will use the term *anisotropic* as the opposite of *isotropic*, to designate a regularization process that does not smooth the image with the same weight in all the spatial directions. In the literature, some authors have different definitions. For instance, Weickert [49] introduces the notions of *homogeneous* and *inhomogeneous* filtering, as well as different definitions for the terms *isotropic* and *anisotropic*.

Chapter 4

A supervised vessel segmentation algorithm using linear scale space

Blood vessels can be viewed as tube-like structures of different widths, lenghts and orientations. To detect this kind of structures in a fundus retina image, we must search for the geometrical feature that describes them at best, finding the scale that gives us the more accurate results. The vessel extraction can be obtained by resorting to different methods (see Chapter 2 for an overview), either rule-based or supervised. In the latter case, the rule for the vessel extraction is "learned" by the algorithm on the basis of a training set of reference manually-processed images. An algorithm with a partial supervision strategy has been recently proposed [17].

In this chapter, we propose a modular supervised algorithm for the segmentation of retinal blood vessels on $M \times N$ red-free images. The algorithm performs two main operations, vessel enhancement and image binarization (plus cleaning), and it has two main characteristics:

- flexibility, due to its supervised nature
- modularity.

If we consider a red-free image $I(x, y)$ as a surface in a 3D space (x, y, I), we can represent fundus retina image as shown in Figure 4.1 (detail).

If we focus our attention on a section of the surface in the direction orthogonal to a vessel, we have locally a convex curve. This will be the basic idea used in the first part of our algorithm to achieve the vessel enhancement.

Usually, all the parameters in algorithms for image processing are heuristically fixed a priori. In other cases, some parameters are fixed by using optimization procedures [18]. In this chapter we determine two "optimal" significant parameters by properly

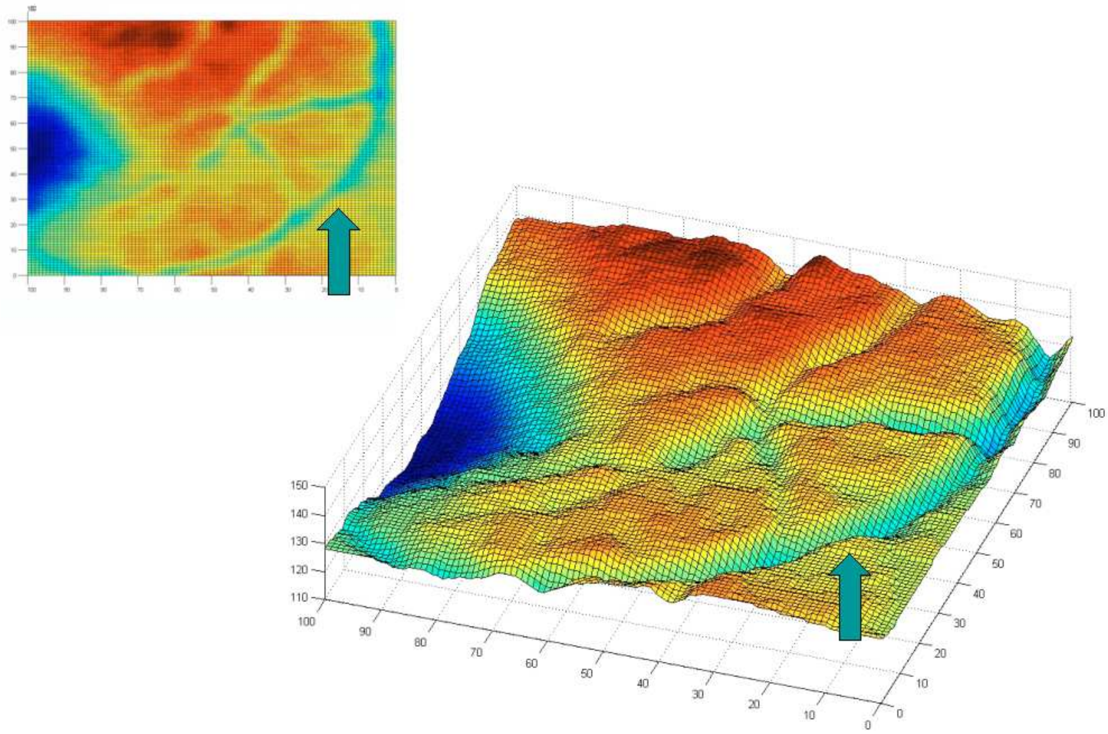

Figure 4.1: On the left: detail of a generic fundus image. On the right: the same crop in a 3D representation.

maximizing some Measures Of Performances (MOPs) for the algorithm applied to a training set. This makes the algorithm supervised.

The optimization procedure our supervised approach is based on makes this algorithm suitable for different purposes. Indeed, the results depend on the chosen MOP and different MOPs can be used to highlight different features in the processed images. This flexibility combines with a modular structure of the algorithm, resulting in quite short computation times. As a matter of fact, the two main processing blocks are made up, in turn, of sub-blocks, thus making the algorithm highly modular, with the possibility of applying only a subset of the possible processing operations. Most of the sub-blocks, moreover, can be implemented by enhancing either the processing accuracy or the simplicity. In the latter case, one reduces the quality of the results in favor of lower complexity and computation times [62].

We realize vessel enhancement through scale-space according to the multiscale analysis theory and the most critical parameter in this part of the algorithm is the scale factor. The image binarization is based on a simple thresholding procedure and the most critical parameter in this part of the algorithm is the threshold. Generally speaking, the sub-blocks the algorithm is made up of are not new. The main novelty elements are

- the use of optimization procedures (supervised, being applied to an image database with reference images) to determine two "optimal" parameters (scale factor and threshold);
- the combination of the sub-blocks to produce an accurate result as a trade-off between processing quality and computation complexity.

The obtained results are compared with those of other methods proposed in the literature.

In particular, using the 20 images of the DRIVE (Digital Retinal Images for Vessel Extraction, see Section 1.3) database test set, we obtain a mean value of 0.9419 for the Maximum Average Accuracy and a mean value of 0.7286 for the agreement between two observers (K-value). The preliminary optimization step can take several minutes, but once the "optimal" parameters are obtained, each segmentation of a fundus image requires only few seconds. Then this algorithm represents a good trade-off between accuracy of the results and computational complexity.

In Section 4.1 we present the algorithm. It involves a linear multiscale analysis, introduced by using the mathematical framework discussed in the previous chapter. After the image binarization, we want to determine the value of the "optimal" parameters: the used MOPs are summarized in Section 4.2, while the target function which is used to determine the optimal parameters' values is defined in Section 4.3. In Section 4.4 some results are presented and commented and the algorithm performances are discussed. Some concluding remarks are drawn in Section 4.5.

4.1 The algorithm

The algorithm is made up of two fundamental blocks (see the dashed boxes in Figure 4.2), exhibiting in turn a modular structure. The first block performs a preliminary contrast enhancement (to compensate the different illumination conditions of fundus images) and is devoted to vessel enhancement, while the second one provides a binary image by resorting to both a thresholding procedure and some cleaning operations.

Of course, each block may be replaced by other (modular) algorithms. For instance, for the first block one can resort to a multi-scale method for retinal image contrast enhancement based on the Contourlet transform [63] or to an algorithm for luminosity and contrast normalization [64].

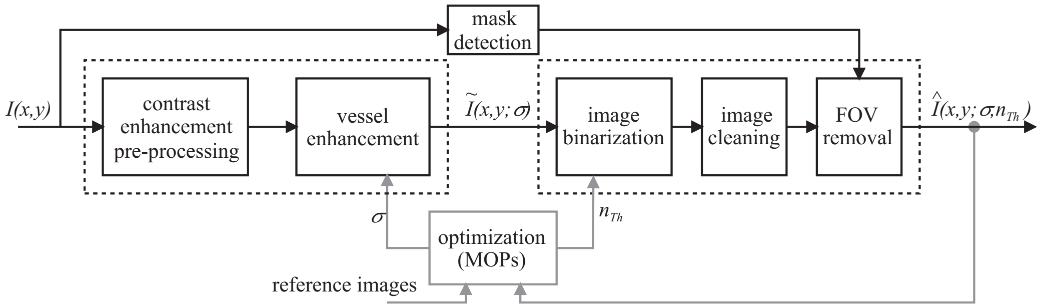

Figure 4.2: Block scheme of the algorithm. The grey elements are related to the supervised training algorithm that determines *a priori* the "optimal" parameters σ and n_{Th}. Once these parameters are fixed, the processing algorithm reduces to the black part of the scheme.

4.1.1 Contrast enhancement pre-processing

To compensate the effects of a non uniform lighting, common in this kind of images and due to changing conditions during the acquisition process, a pre-processing of the images has to be done. To this end, we use the function ADAPTHISTEQ, contained in the Image Processing *Matlab*® Toolbox, which performs a Contrast-Limited Adaptive Histogram Equalization (CLAHE) [65, 66].

The CLAHE algorithm operates on small regions in the image, called tiles, rather than on the entire image. Each tile's contrast is enhanced, so that the histogram of the output region approximately matches a uniform histogram. The neighboring tiles are then combined using bilinear interpolation to eliminate artificially induced boundaries. The contrast, especially in homogeneous areas, can be limited to avoid amplifying any noise that might be present in the image.

We call $I_0(x, y)$ the image that we obtain after the contrast enhancement. In Figure 4.3 an example is shown.

4.1.2 Vessel enhancement

To perform the vessel enhancement, we adopt the method introduced in [67] and [68] and then used in [15] to process two-dimensional fundus images. The vessel enhancement procedure, devoted to highlight geometric tube-like structures, is based on the Hessian operator $\boldsymbol{H}$ of the function $I(x, y; \sigma)$.

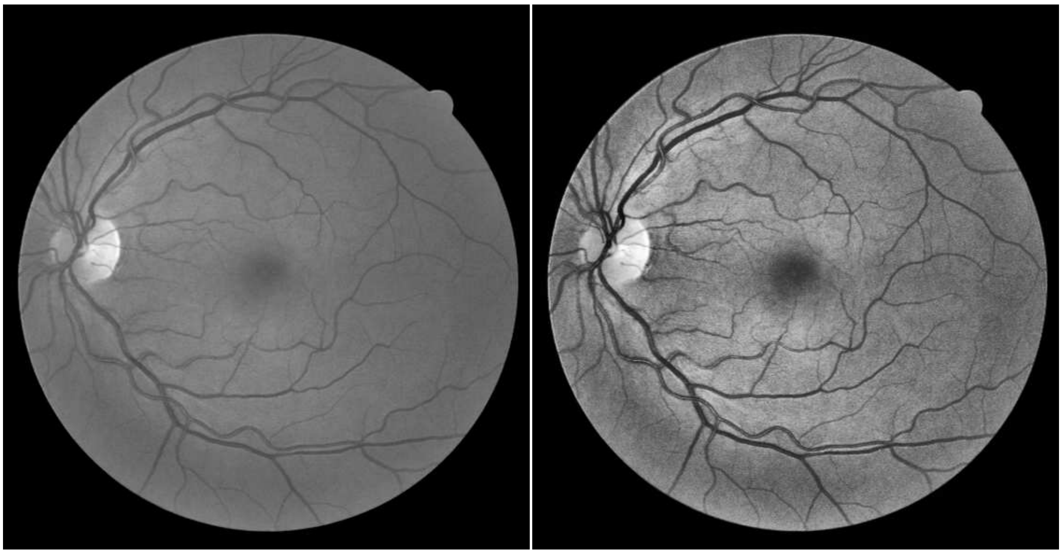

Figure 4.3: Example of contrast enhancement. (a) Original image. (b) Enhanced image

The linear scale-space

We call $I(x, y; \sigma)$ the scale-space due to a linear multiscale analysis and then a linear diffusion of the image to be processed $I_0(x, y)$. As pointed out in Section 3.4, linear diffusion is an isotropic diffusion and then realizes an **isotropic regularization**. It represents the easier way to smooth and simplify data and has consequently been reached by several mathematical formulations: from the restoration scheme proposed by Tikhonov in [69] to the classic linear filtering of images (for istance in the Fourier spectral space [70]), the proposed methods lead to the same regularization behaviour.

We use $I_0(x, y)$, the enhanced fundus retina image, to start our elaboration. Using the framework introduced in the previous chapter we can give a variational formulation of this problem:

$$\begin{aligned} E\left(I(x, y; \sigma)\right) &= \int_{\Omega} (I - I_0)^2 + \sigma \left\| \nabla I(x, y) \right\|^2 \, dxdy \\ &= \int_{\Omega} (I - I_0)^2 + \sigma \left(\left(\frac{\partial I(x, y)}{\partial x} \right)^2 + \left(\frac{\partial I(x, y)}{\partial y} \right)^2 \right) dxdy \quad (4.1) \end{aligned}$$

where, with respect to Equation (3.13), in this case we have

$$\Phi(s) = s^2 \rightarrow \Phi(\|\nabla I\|) = \|\nabla I\|^2 \quad (4.2)$$

By remembering the link between the variational form and the differential one, expressed in Equation (3.26), we can calculate:

$$g(\|\nabla I\|) = \frac{1}{2}\frac{\Phi'}{\|\nabla I\|} = \frac{1}{2}\frac{2\,\|\nabla I\|}{\|\nabla I\|} = 1 \tag{4.3}$$

Now, we are able to formulate the same problem by using the divergence form:

$$\frac{\partial I}{\partial t} = \nabla(\nabla I) = \Delta I = \frac{\partial^2 I}{\partial x^2} + \frac{\partial^2 I}{\partial y^2} \tag{4.4}$$

and by using I_0 as initial condition. We have obtained the well known *heat equation*, used in physics, for istance, to describe heat flows through solids. As shown in the previous chapter only linear multiscale realizes an isotropic diffusion.

Koenderink noticed in [71] that the solution of Equation (4.4) at a particular time t is the convolution of the original image I_0 with a *normalized 2D Gaussian kernel* G_σ of standard deviation $\sigma = \sqrt{2t}$:

$$I(x, y; \sigma) = (T_\sigma I_0)(x, y) = G_\sigma * I_0 \tag{4.5}$$

In a more explicit notation:

$$I(x, y; \sigma) = \int\int I_0(x - u, y - v) G_\sigma(u, v)\, dudv \tag{4.6}$$

with

$$G_\sigma = G(x, y; \sigma) = \frac{1}{2\pi\sigma^2} \quad e^{-\frac{x^2+y^2}{2\sigma^2}} \tag{4.7}$$

This means that the regularization is linear (based on a convolution). The regularization behavior is then typical of a linear multiscale analysis: the signal is blurred little by little in an isotropic way during the PDE evolution (see Figure 4.4).

Note that convolving an image by a Gaussian kernel is equivalent to multiply the Fourier transform of this image by another Gaussian kernel: the isotropic regularization behaves then as a *low-pass filter* suppressing high frequencies in the image I.

Unfortunately, image contours are high frequency signals as well as noise. As illustrated in Figure 4.5, they are quickly blurred by such an isotropic scheme. The need to resort to more complex non-linear and anisotropic regularization methods quickly appeares (in particular for noise removal image restoration purposes). Nevertheless, a

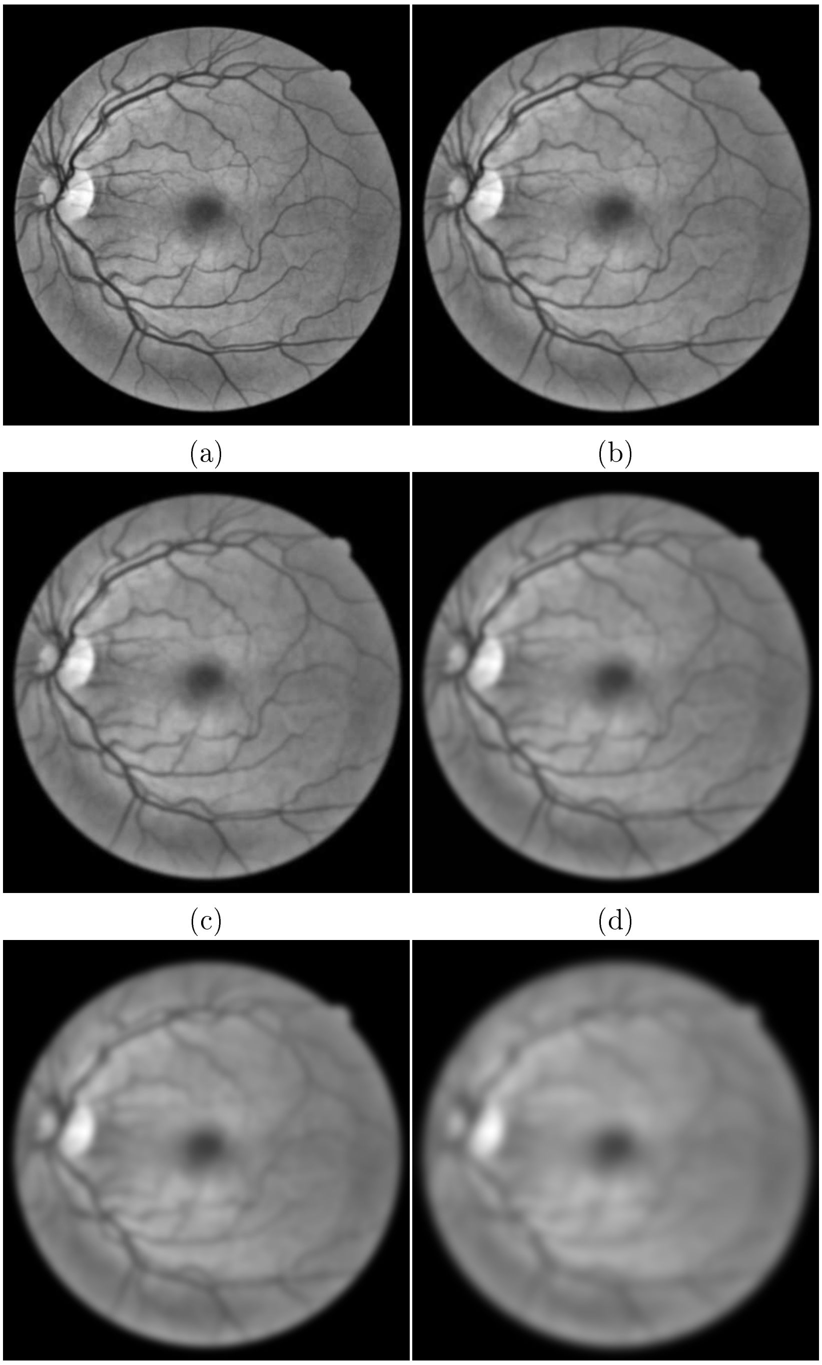

(a) (b) (c) (d) (e) (f)

Figure 4.4: Example of linear scale-space: $\sigma^2 = 2, 4, 8, 16, 32, 64$.

basic linear multiscale analysis maybe enough for our segmentation task, keeping the global implementation very simple. Moreover, in the next chapter we will investigate the improvements in the quality of the results that we obtain by using a non linear multiscale analysis.

Evaluation of the Hessian matrix and its eigenvalues

We have now to evaluate the Hessian matrix along the scales and then the second order spatial derivatives of I_0. We have shown that Gaussian kernel is the scale-space operator at the basis of the linear multiscale analysis. There is an important additional result: the spatial derivatives of the Gaussian kernel are also solutions of the heat diffusion equation, and, together with the zeroth-order Gaussian (see Equation (4.7)), they form a complete family of differential operators [72].

Since we may commute the differential and the convolution operators

$$\frac{\partial}{\partial x}(I_0 * G_\sigma) = I_0 * \frac{\partial G}{\partial x} \tag{4.8}$$

the derivative of I_0 can be found by convolving the image with the derivative of a Gaussian. This is true for derivatives of any order.

Then, the Hessian matrix of $I_0 * G$ can be expressed as follows:

$$\boldsymbol{H}(I_0(x,y) * G(x,y;\sigma)) = \begin{bmatrix} L_{xx}(x,y;\sigma) & L_{xy}(x,y;\sigma) \\ L_{yx}(x,y;\sigma) & L_{yy}(x,y;\sigma) \end{bmatrix} \tag{4.9}$$

where

$$L_{\alpha\beta}(x,y;\sigma) = I_0(x,y) * \frac{\partial G(x,y;\sigma)}{\partial \alpha\beta}, \quad \alpha,\beta \in \{x,y\} \tag{4.10}$$

For a given value of the scale parameter σ, the eigenvalues $\lambda_\pm$ of the Hessian matrix $\boldsymbol{H}$ measure the convexity of $I_0 * G$ in the corresponding eigendirections [21]. At each point $(x,y;\sigma)$, the eigenvalue with the maximum absolute value is denoted as $\Lambda(x,y;\sigma)$ and the corresponding eigenvector is parallel to the direction of maximum curvature of the grey level. In the considered red-free images, a high positive curvature marks the presence of ridges in the low-pass filtered surface $I * G$, i.e., the presence of vessels in the image. Then, the processed image can be obtained as follows:

$$\tilde{I}(x,y;\sigma) = \max\left(0, \Lambda(x,y;\sigma)\right) \tag{4.11}$$

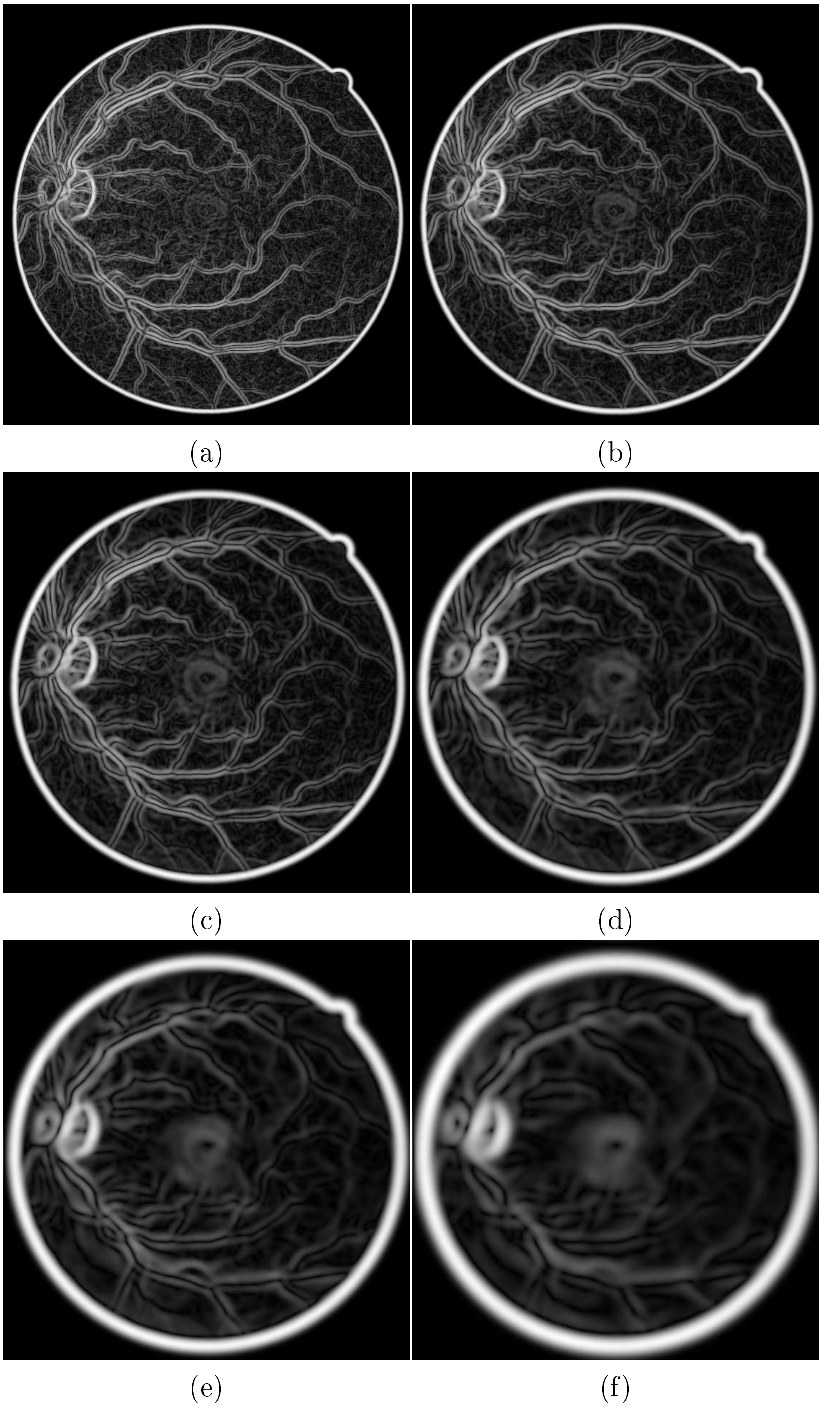

(a) (b) (c) (d) (e) (f)

Figure 4.5: Contours of a fundus image along a linear scale-space: $\sigma^2 = 2, 4, 8, 16, 32, 64$.

The standard deviation σ is our *scale parameter* and must be properly set.

Basically, the scale fits the average vessel thickness in the considered images. There are multiscale algorithms which combine together the results obtained at different scales [15]. The results are usually accurate, but at the cost of high computation times. In this thesis, we set an "optimal" value for the parameter σ by properly maximizing some MOPs, that are able to quantitatively measure the performances of the image processing algorithm.

Before performing the operations described in the next subsection, the histogram of the grey levels of $\tilde{I}(x, y; \sigma)$ is stretched between 0 and 255.

4.1.3 Image binarization and cleaning

Histogram based binarization

In order to segment the vessels through image binarization, we must identify a proper threshold grey level Th. This threshold can be implicitly chosen by fixing the fraction n_{Th} of image pixels whose intensity level will be set to 0, i.e., those pixels with grey levels between 0 and Th. So doing, the value of Th turns out to be image dependent and it is not influenced by possible scalings on the image luminosity level. The value of n_{Th} will be directly derived through the optimization procedure described in Section 4.3. Figure 4.7 shows an example of binary image at this processing stage.

Cleaning of spurious elements

Once the binary image is available, it can be desirable to delete spurious elements not belonging to the vessel network. To this end, we adopted a simple algorithm, that, at best of our knowledge, is original and is illustrated in Figure 4.8.

We fix a virtual grid made up of squares of $n \times n$ pixels and, for each square, we focus on the perimetric pixels. If such pixels are all black, we assume that the corresponding square contains either only background pixels or spurious elements, not connected with the vessel structure. In both cases, the whole square is set to black, thus removing the possible spurious elements.

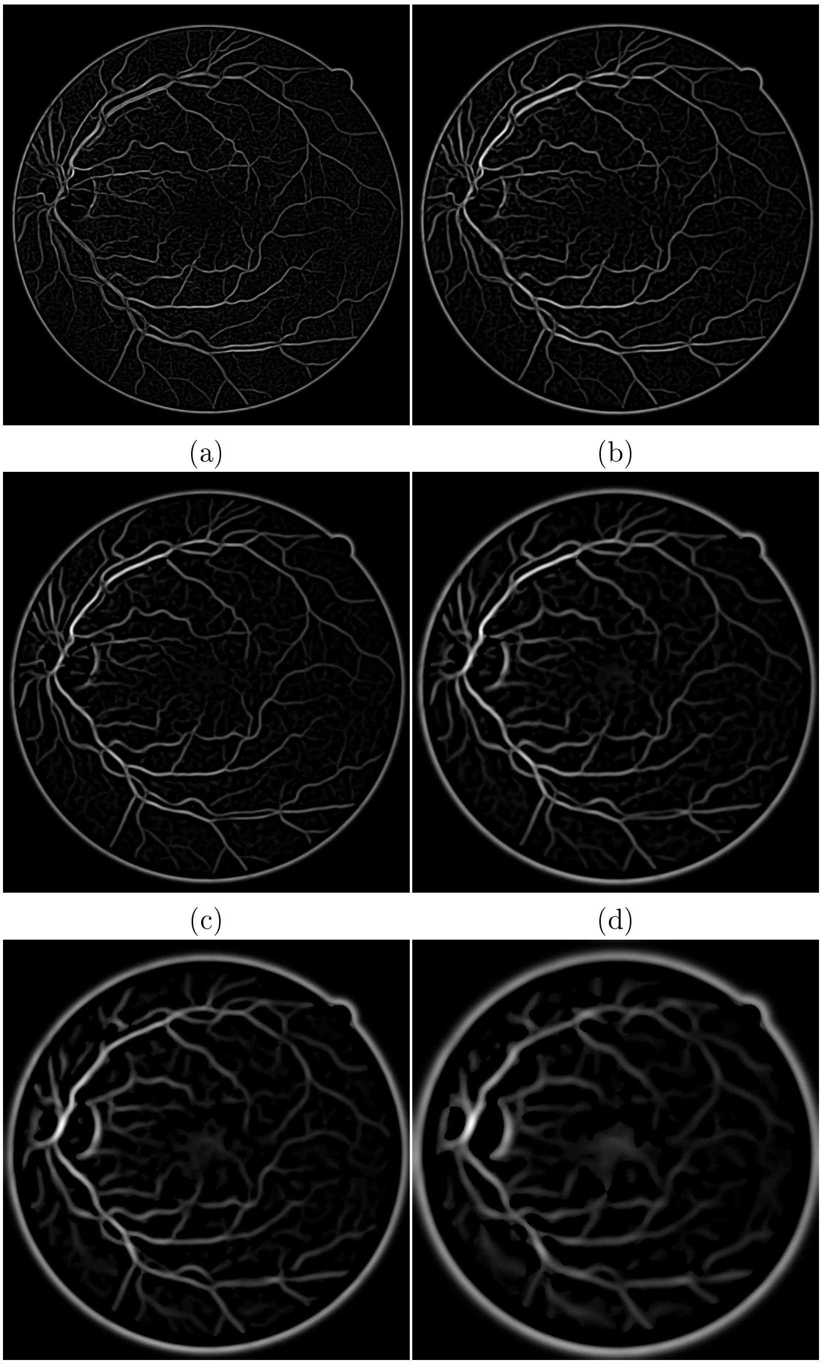

(a) (b) (c) (d) (e) (f)

Figure 4.6: (a) $\tilde{I}$ at different scales: scale $\sigma^2 = 2, 4, 8, 16, 32, 64$.

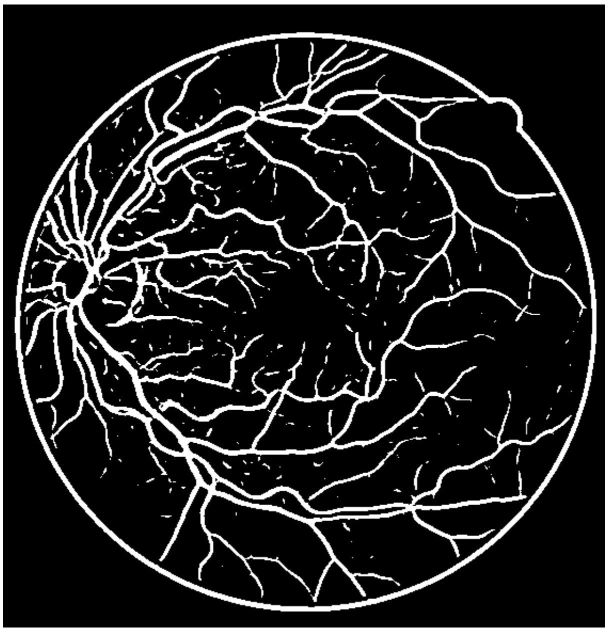

Figure 4.7: Example of image that we get after the binarization of $\tilde{I}(x, y; \sigma)$, before the cleaning task.

This cleaning algorithm can be iterated by changing n or the virtual grid position, so as to accurately clean the image, but at the cost of an increasing computational effort. Figure 4.8 shows what happens if we choose to iterate the algorithm only twice, with $n = 10$. In the first step, the grid completely covers the image (see a detail in Figure 4.8(a)) and some spurious elements or not connected parts of vessels (see the grey squares in Figure 4.8(a)) are removed, as shown in Figure 4.8(b). In the second step, the grid is shifted by 5 pixel both horizontally and vertically (grey grid in Figure 4.8(c)) and other elements (see the grey squares in Figure 4.8(c)) are removed, as shown in Figure 4.8(d).

As an alternative, thanks to the algorithm modularity, one may resort to other morphological solutions (e.g., area opening) for the cleaning block in order to achieve a different trade-off between speed and accuracy requirements.

Field Of View edge removal

We point out that the block described so far provide not only the vessel tree but also the edge of the field of view (FOV), as shown in Figure 4.7(a). This edge is evidenced by the vessel enhancement block and to remove it we must introduce a proper set of operations. The histogram of the original image $I(x, y)$ (see Figure 4.9(a)) exhibits an

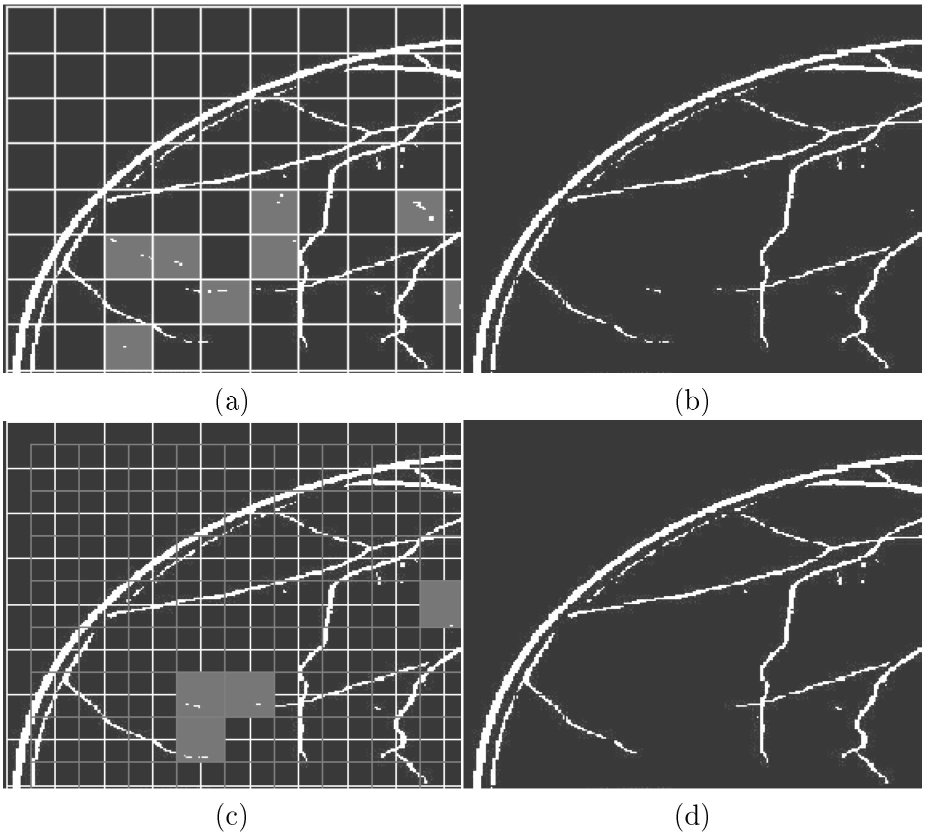

Figure 4.8: An example of the cleaning operation.

evident peak at very low gray levels. This peak is clearly distinct from the central part of the histogram, representing the FOV pixels. By resorting to a simple and robust thresholding operation, it is possible to define an $M \times N$ mask made up of white pixels corresponding to pixels of the FOV and black pixels elsewhere. The logical multiplication of the binary image resulting from the vessel extraction algorithm with this mask provides images similar to the one shown in Figure 4.9(b), where the edge of the FOV is not completely removed. To accurately delete this edge, we can perform a slight erosion of the white portion of the mask by using, as structuring element, a disk of 5-pixels radius. This operation is not particularly sensitive as only the peripheral portion of the vessel tree could be partially involved.

The image provided by the binarization, cleaning, and FOV removal blocks is called $\hat{I}(x, y; \sigma, n_{Th})$.

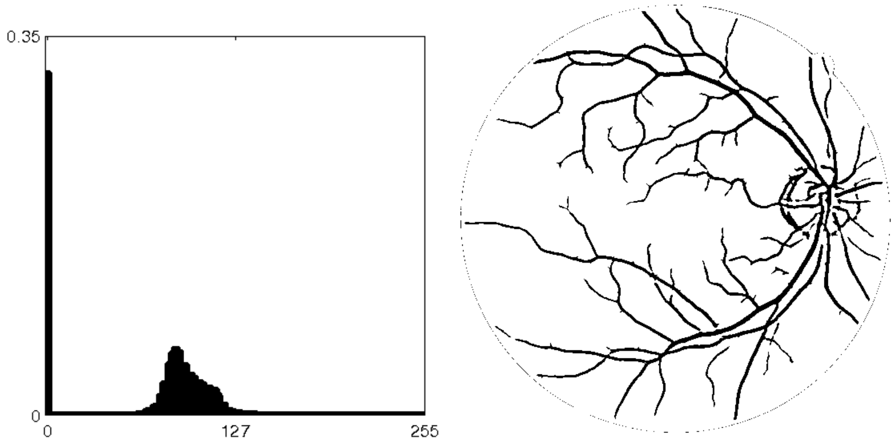

(a) (b)

Figure 4.9: (a) The normalized histogram of the green channel of a typical fundus image. Beside this, the negative of a typical binary image obtained by resorting to the proposed vessel extraction algorithm without doing any operation to remove the edge of the FOV. (b) Negative of a typical binary image obtained by applying the block to remove the edge of the FOV without the preliminary erosion of the white portion of the mask.

4.2 Measures of performances for vessel detection

Generally speaking, a MOP is nothing more than a quality measure that addresses how well a system works. In this Section, some MOPs are introduced to evaluate from a quantitative point of view the results provided by the proposed algorithm.

The MOPs defined in the following are based on two images: a reference binary image $\bar{I}$ - resulting from the manual segmentation of a fundus image I performed by people trained by an experienced ophthalmologist - and the binary image $\hat{I}$ - resulting from the algorithm.

We remark that, since $\hat{I}$ depends on the algorithm parameters σ and n_{Th}, also each MOP depends on σ and n_{Th}. For the sake of simplicity, however, in the next subsections such a dependence will be omitted.

4.2.1 Maximum Average Accuracy (MAA)

The MAA evaluates the MOP of the vessel detection algorithm in correspondence with the N_{FOV} pixels belonging to the FOV [73]. This MOP expresses the number of pixels that have been correctly classified with respect to N_{FOV}:

$$MAA = 1 - \frac{\sum_{j,k \in FOV} \left| \bar{I}_{jk} - \hat{I}_{jk} \right|}{N_{FOV}} \in [0, 1] \tag{4.12}$$

4.2.2 K value

Preliminarily, we define the following quantities: n_{tp} is the percentage of true positive pixels (i.e., white pixels in $\hat{I}$ that belong to the manually extracted vessels in $\bar{I}$), n_{fp} is the percentage of false positive pixels (i.e., white pixels in $\hat{I}$ that do not belong to manually extracted vessels in $\bar{I}$), n_{fn} is the percentage of false negative pixels (i.e., black pixels in $\hat{I}$ that belong to manually extracted vessels in $\bar{I}$), and n_{tn} is the percentage of true negative pixels (i.e., black pixels in $\hat{I}$ that do not belong to manually extracted vessels in $\bar{I}$). The over mentioned percentages are taken with respect to the MxN pixels of the image to be processed.

The K value is a measure of the agreement between two observers [74]:

$$K = \frac{OA - EA}{1 - EA} \in [-1, 1] \tag{4.13}$$

where $OA = (n_{tp} + n_{tn})$ is the *observed agreement* and $EA = (n_{tp} + n_{fp})(n_{tp} + n_{fn}) + (n_{fn} + n_{tn})(n_{fp} + n_{tn})$ is the *expected agreement*. The index OA expresses the percentage of pixels of $\bar{I}$ that are correctly classified in $\hat{I}$, while the index EA expresses the probability that the two observation coincide. Indeed, EA can be interpreted as the sum between the product of the percentages of white pixels in $\hat{I}$ $(n_{tp} + n_{fp})$ and in $\bar{I}$ $(n_{tp} + n_{fn})$ and the product of the percentages of black pixels in $\hat{I}$ $(n_{fn} + n_{tn})$ and in $\bar{I}$ $(n_{fp} + n_{tn})$.

4.2.3 Q value

This MOP is defined according to the universal image quality index defined in [75]. Such an index is "universal" in the sense that the quality measurement approach does not depend on the images being tested, the viewing conditions or the individual observers.

We consider two images, t and r, where t is the image whose quality must be evaluated (in our case $t = \hat{I}$), whereas r is the reference image (in our case $r = \bar{I}$). To define the index Q, we preliminarily introduce a square window $w(j, k)$ of $n_w \times n_w$ image pixels. Such a window slides over the images r and t, starting from the top-left corner and moving pixel by pixel horizontally and vertically through all the rows and columns of each image until the bottom-right corner is reached. The index $Q \in [-1, 1]$ is defined as follows:

$$Q(t,r) = \frac{1}{|W|} \sum_{w(j,k)\in W} \frac{4\sigma_{tr}(j,k)\bar{t}(j,k)\bar{r}(j,k)}{\left(\sigma_t^2(j,k)+\sigma_r^2(j,k)\right)\left(\bar{t}^2(j,k)+\bar{r}^2(j,k)\right)} \tag{4.14}$$

where $|W|$ is the overall number of possible different positions of the window w over each image, whereas $\bar{t}(j,k)$ and $\bar{r}(j,k)$, $\sigma_t^2(j,k)$ and $\sigma_r^2(j,k)$, and $\sigma_{tr}(j,k)$ are the mean values, the variances, and the covariance, respectively, of the images t and r on each window position. The explicit expressions used to calculate the mean values, the variances and the covariances of the images t and r at each window position are provided in Appendix B. For the Q value, we set $n_w = 8$ to have a window large enough to obtain reliable estimates of the mean, variance and covariance of this MOP.

4.3 Optimization

The binary images obtained by resorting to the supervised algorithm proposed in this chapter depend on the algorithm parameters σ and n_{Th}. For this reason, it is necessary to define a procedure to choose proper values for these parameters in order to ensure a good quality of the results. To do that, a training set made up of N_{TS} fundus images (together with their reference segmentations) can be used and σ and n_{Th} can be fixed by maximizing the quality of the results obtained by processing the images belonging to it. In this sense the proposed algorithm turns out to be supervised.

From a practical point of view, one can choose one of the MOPs introduced in the previous section and then either maximize the following target function

$$F(\sigma, n_{Th}) = \frac{1}{N_{TS}} \sum_{k=1}^{N_{TS}} MOP_k(\sigma, n_{Th}) \tag{4.15}$$

or minimize $-F(\sigma, n_{Th})$.

We have used the simplex search method of [76]. It is generally referred to as *uncostrained non linear optimization*. This is a direct search method, based on the convergence properties of the Nelder-Mead simplex method, that does not use numerical or analytic gradients.

Such an algorithm is been implemented in the function FMINSEARCH, contained in $Matlab^{®}$. Starting from a initial point $P_0 = (\sigma_0, n_{Th0})$ and using this algorithm, we can find only local minimizers (or maximizers), but this is not a problem since working in a reasonable space of the parameters

$$(\sigma, n_{Th}) \in [1, 8] \times [0.85, 0.95] \tag{4.16}$$

the MOPs behave regularly; they are convex functions as shown in Figure 4.10 for MAA.

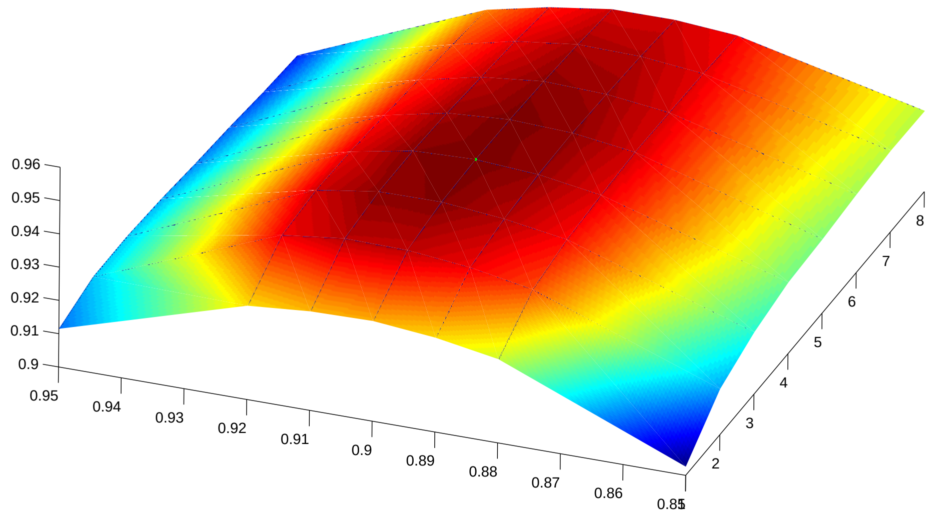

Figure 4.10: MAA convex behaviour.

This is true also for the other two MOPs, K and Q.

4.4 Simulation results

To derive the image processing results presented in this Section as benchmarks for the proposed algorithm, the 40 fundus images making up the DRIVE database have been used. In particular, our training set contains the last 20 images ($N_{TS} = 20$) of the database, whereas the first 20 images are a test set used to measure the performances of the algorithm whose parameters have been tuned according to the optimization procedure.

The cleaning operation has been iterated for many values of n. For each value of n, the corresponding grid has been shifted on the image by positioning its upper-left vertex in all the pixels (j, k) for $j = 1, \ldots, n-1$ and $k = 1, \ldots, n-1$. The sequence of values assigned to n is $\{3, 4, 8, 16, 4, 8, 16\}$ and has been chosen heuristically after many trials. We need to repeat twice some values of n in the sequence, since a single application would clean only one element in pairs of close spurious patterns.

4.4.1 Training phase

During the training phase, for each MOP defined in the previous section, the optimal values of the algorithm parameters σ and n_{Th} have been obtained by maximizing $F(\sigma, n_{Th})$. These values are given in the first and second columns of Table I, respectively. The MOPs values corresponding to the best and worst cases are shown in the third and fourth columns, respectively. These values were obtained by processing the images of the training set with the optimal values of the algorithm parameters. Figure 4.11 shows the corresponding image-processing results, i.e., the best (first row) and worst (second row) vessel extraction results for the training set images in terms of MAA (a,d), K (b,e), and Q (c,f). The number of original images in the database is also given.

Table I

Table 4.1: Values of σ, n_{Th}, best and worst cases after optimization, for each MOP

MOP	σ	n_{Th}	Best case	Worst case
MAA	2.0253	0.90946	0.9541	0.9067
K	2.1505	0.89261	0.7610	0.5958
Q	2.0882	0.88603	0.7295	0.5406

Once the optimal values of σ and n_{Th} have been obtained, the algorithm can be applied to other images to test its performances.

4.4.2 Test phase

The first two columns of Table II contain the mean values and the standard deviations, respectively, of the MOPs obtained by processing the images of the test set after fixing the parameters σ and n_{Th} at their optimal values (see Table I). The values of the

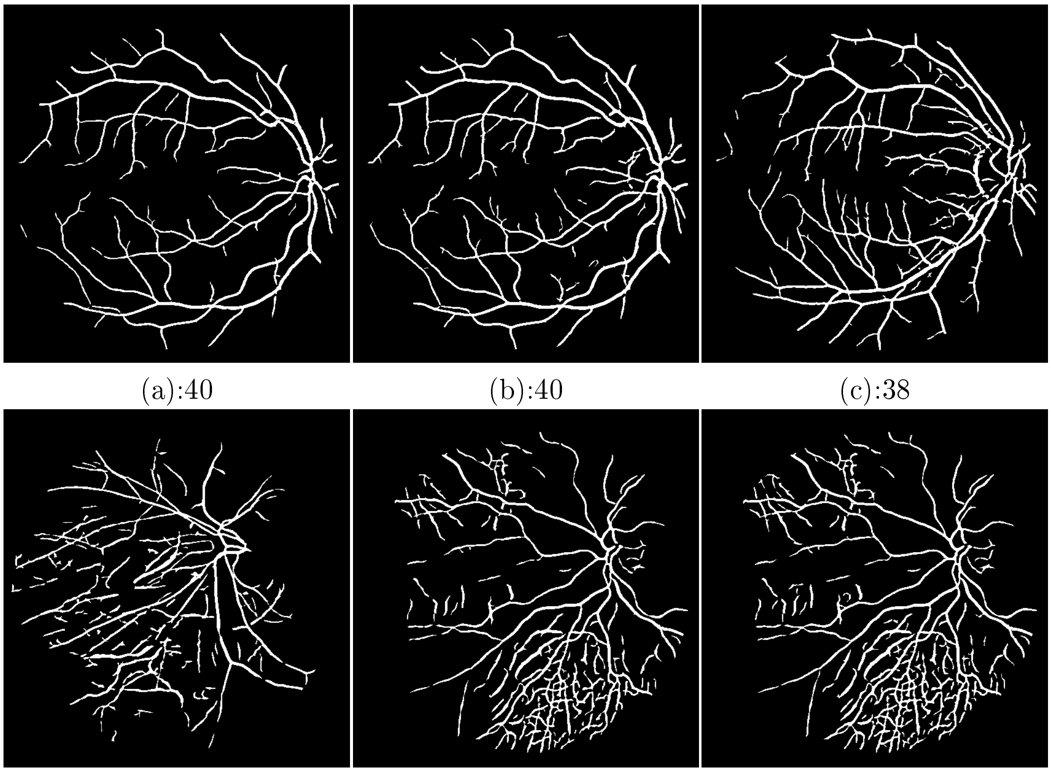

(a):40 (b):40 (c):38

(d):34 (e):23 (f):23

Figure 4.11: Best (first row) and worst (second row) vessel extraction results for the training set images with respect to MAA (a,d), K (b,e), and Q (c,f). The database numbers of the original images are shown next to the labels.

MOPs corresponding to the best (third column) and worst (fourth column) cases are also shown. The fifth and sixth columns contain the mean values of the True Positive Fraction (for each image, the percentage of vessel pixels actually classified as vessel pixels) or TPF and of the False Positive Fraction (for each image, the percentage of non-vessel pixels actually classified as vessel pixels) or FPF, respectively, for the 20 images of the test set. In Figure 4.12, the segmented images corresponding to the best (first row) and worst (second row) cases are provided for the test set in terms of MAA (a,d), K (b,e), and Q (c,f). The number of original images in the database is given.

4.4.3 Comparison with other methods

By resorting to the first two MOPs (MAA and K), it is possible to compare the per-

Table II

Table 4.2: Mean values, standard deviations, best and worst cases, mean TPF and FPF for the MOPs with σ and n_{Th} set to their optimal values.

MOP	Mean	Standard deviation	Best case	Worst case		Mean TPF	Mean FPF
MAA	0.94183	0.00822	0.9587	0.9275		0.6377	0.0091
K	0.72860	0.03452	0.8069	0.6642		0.7052	0.0162
Q	0.69123	0.03933	0.7735	0.6247		0.7246	0.0193

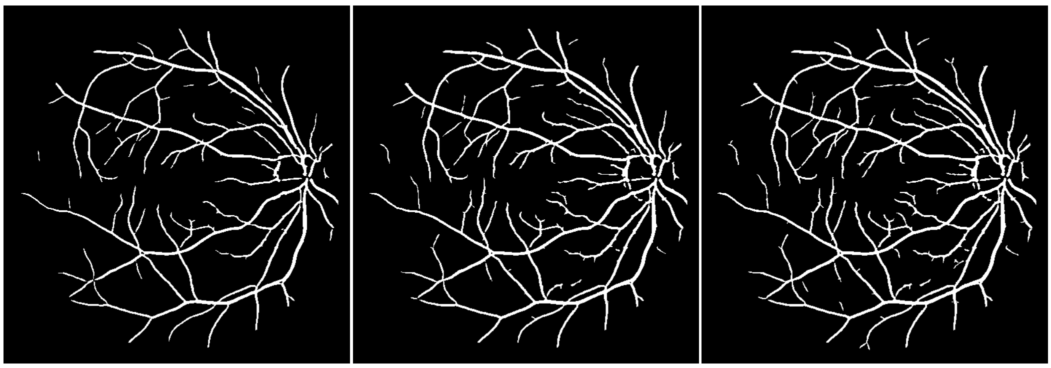

(a):19 (b):19 (c):19

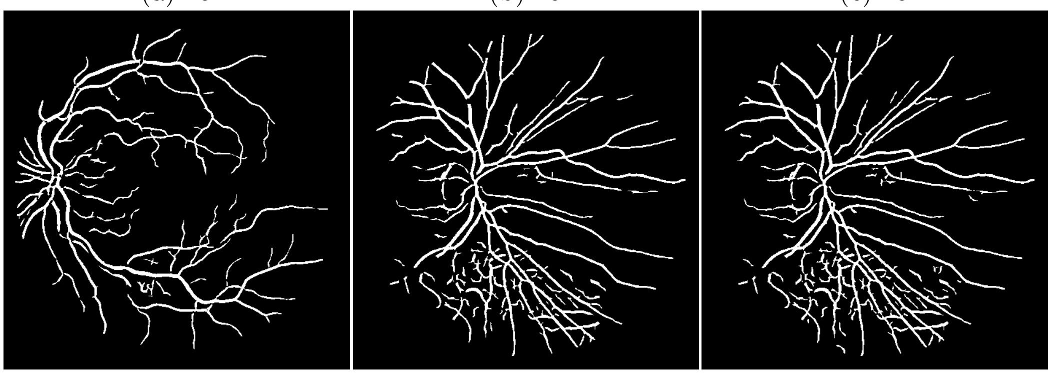

(d):3 (e):15 (f):15

Figure 4.12: Best (first row) and worst (second row) vessel extraction results for the test set images with respect to MAA (a,d), K (b,e), and Q (c,f). The database numbers of the original images are shown next to the labels.

formances of the proposed algorithm with the ones of other algorithms that can be found in the literature. The first two columns of Table III contain the mean values of both MAA and K, obtained by a second independent manual segmentation available for the first 20 images of the DRIVE database (first row) and by processing the test set images by resorting to different methods [73, 14]: primitive-based method [14], pixel classification method [73], mathematical morphology and curve estimation method [77], verification-based local thresholding method [78], scale-space analysis and region growing approach [79], matched filter method [20]. Among these algorithms, only the pixel classification and primitive-based methods are supervised.

Table III

Table 4.3: Comparisons with other methods proposed in the literature

Method	MAA	K	TPF	FPF
Second manual segmentation	0.9473	0.7589	0.776	0.0275
Primitive-based method	0.9441	0.7345	0.697	0.019
Our algorithm	0.9419	0.7286	0.7246	0.019
Pixel classification	0.9416	0.7145		
Mathematical morphology	0.9377	0.6971		
Local thresholding	0.9212	0.6399		
Scale-space and region growing	0.9181	0.6389	0.7246	0.0345
Matched filter	0.8773	0.3357		
All background	0.8727	0		

The last two columns of Table III contain the mean values of TPF and FPF, respectively, for some of the considered methods. In particular, for our method, we have reported the mean TPF and FPF for the MOP Q, which provides the best results (see Table II).

Comparisons of the results summarized in Tables II and III evidence that the performances of the proposed algorithm are close to the ones of well-known algorithms proposed in the literature. On the whole, the results confirm that supervised methods represent a reliable way to get the best results. We remark that in this case the algorithm is much less computationally expensive than the best algorithm in Table III. Using a Matlab® implementation and not a faster C++ one, running on a Intel® Celeron® CPU 2.40GHz with 192Mb RAM, the initial optimization phase of our algorithm can take several minutes, but after this, once the "optimal" values for parameters σ and n_{Th} are fixed, each segmentation of a fundus image does not require more than six seconds, for images of size 564x584 pixels. The Primitive-based method algorithm, instead, requires a processing time of several minutes, in similar conditions [14]. We remark that the modular structure of the proposed algorithm may allow one a further speed up of the computations if combined with a pipeline architecture, i.e., if the sub-blocks can process in parallel different images.

4.4.4 MOPs influence on the results

By using the Q value as measure of performance, we show how different features of the results can be highlighted. In particular, with this MOP we can detect a higher number of small vessels, related to higher values of the mean TPF for this MOP (see Table II). The price to pay is a larger number of wrongly classified pixels, related to higher values of the mean FPF (see Table II). Anyway, we remark that these new false positives are confined to regions close to image elements denoting the presence of some pathologies (e.g., drusen, exudates, age-related macular degeneration) and then they affect the results only for images containing this kind of elements.

For istance Figure 4.13 shows:

1. vessel segmentation of an image with no pathologies, for σ and n_{Th} obtained by training with (a) MAA and (b) Q;
2. vessel segmentation of an image with signs of mild early diabetic retinopathy, for σ and n_{Th} from the training with MAA (c) and with Q (d).

The number of original images in the database is given.

4.5 Remarks

A supervised algorithm for vessel segmentation in red-free images of the human retina has been proposed. Two parameters have been identified whose choice seems to be particularly critical. The "optimal" values for these parameters are obtained by optimizing proper target functions, defined on the basis of some MOPs. We referred to three examples of MOPs, but different choices can fit different specific requirements. We point out that nowadays there is not, in the literature, a common opinion about a universal MOP able to evaluate adequately the results of most of the algorithms. Moreover, different applications may need a different attention on specific aspects of the result: as an example, one may be interested in having a higher accuracy on small vessels or in determining the vessels' widths or in finding at best the ramifications of the vessels' tree. Several applications do not need either all the cited features nor that

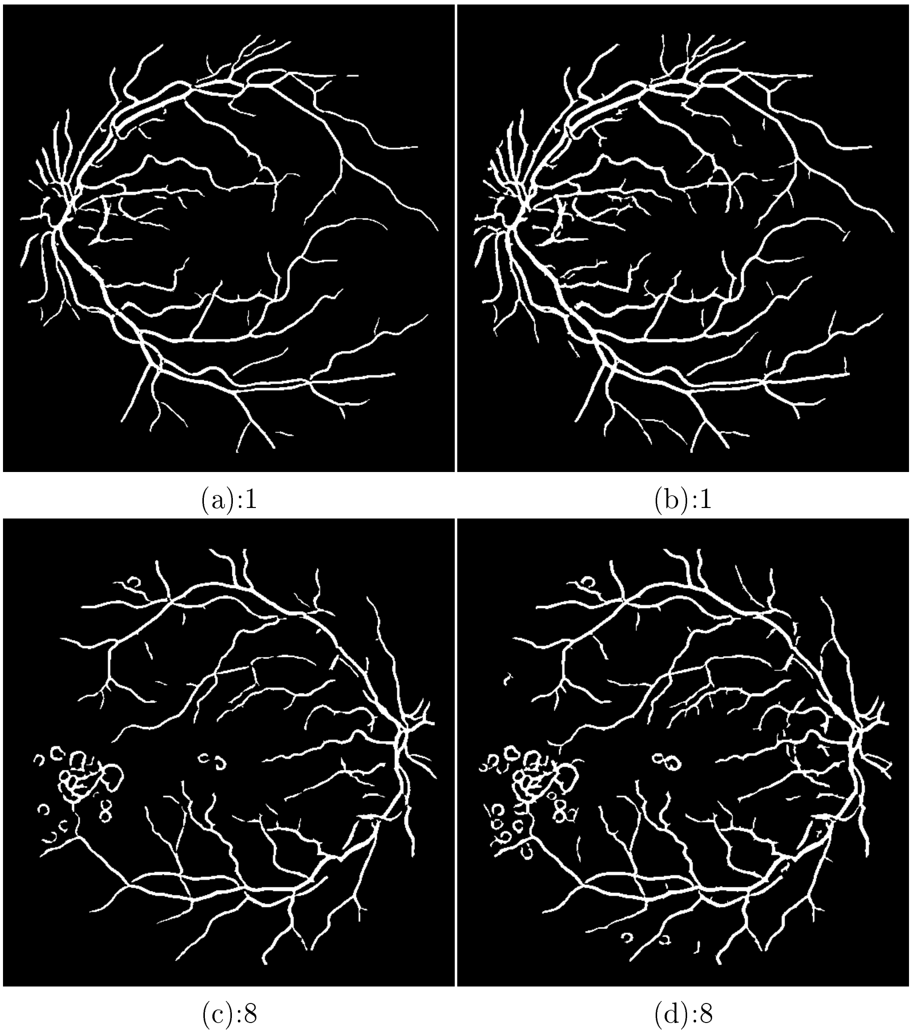

Figure 4.13: (a) Vessel segmentation of an image with no pathologies, for σ and n_{Th} obtained from the training with MAA. (b) Result for σ and n_{Th} from the training with Q. (c) Vessel segmentation of an image with signs of mild early diabetic retinopathy, for σ and n_{Th} from the training with MAA. (d) Result from the same image but for σ and n_{Th} from the training with Q. The database numbers of the original images are shown next to the labels.

these features are detected all at the same time. The proposed algorithm is enough flexible to be customized for different applications, simply by changing the reference MOP.

We have experimentally verified that choosing the threshold Th implicitly, by fixing the fraction n_{Th} of image pixels whose intensity level is set to 0, provides better results than choosing Th directly. For instance, in the latter case, we obtain a mean value of 0.94015 and a standard deviation of 0.00898 for MAA, which is a worst result if compared with the first row in Table II.

With respect to other Hessian-based methods (e.g., [15]), where two or more thresholds are required, our choice of defining the algorithm only for red-free images (setting to zero the eigenvalue $\Lambda(x, y)$ with maximum absolute value in correspondence of negative curvature regions) allowed us to obtain satisfactory results with only one threshold. Indeed, in this case the only high-curvature structures are the vessels. We point out that the same algorithm can work with the negative of fluorescein images.

The choice of a single "optimal" scale factor σ, instead of a multi-scale approach, yields similar results, and reduces considerably the computational effort. As a matter of fact, by using the 20 images of the test set, with a multi-scale algorithm we obtained the best average $MAA = 0.9423$, with scales within the interval of $1 \leq s \leq 10$ pixels in steps of 1 pixel and with optimization only on n_{Th}. With our algorithm, the best average MAA was 0.94183 (see Table II). A further visual inspection of the results reveals that there are not appreciable differences in the detection of small vessels. Only slight differences in the width of vessels can be appreciated.

We have already remarked that the cleaning procedure deletes all the spurious elements. It may happen that some of these spurious elements belong to thin vessels, which remain therefore unconnected to the main tree. Specific measures allowed us to state that this is a marginal behavior. As compared with the complete algorithm, a version not containing the cleaning procedure causes an increase of 30% in the FPF and of only 4% in the TPF. This confirms that most of unconnected spurious little clusters do not belong to the vessel tree. These measures are average values for the 20 images of the test set and have been obtained by σ and n_{Th} fixed after the training with MAA (see Table I).

Finally, we remark that the quality of the results may be further improved by adding other processing blocks. For instance, a procedure for removing pixels belonging to the edge of the optic disk could be introduced. Another improvement for images showing some pathology (e.g., drusen, exudates, and others) may be obtained by a block for the elimination of light objects before segmenting the vessels in pathological images. As a matter of fact, Figure 4.13 points out that light objects in pathological images usually have a bad influence on results, mainly when the objects are near or touch the vascular network. The presence of a block that eliminates these objects before vessel segmentation should overcome this drawback, thus having a positive influence on the calculation of σ and n_{Th}.

Chapter 5

Improving vessel segmentation using non-linear scale space

In this chapter we introduce a modified version of the algorithm described in the previous chapter. Our aim is to improve the segmentation results. Furthermore, we use it for the segmentation of noisy fundus retina images. Denoising (or image restoration) is, with segmentation, one of the most basic image processing problem. It constitutes a significant preliminary step in several machine vision tasks, such as object detection and recognition. It is also one of the mathematically most intriguing problems in vision.

A major concern in designing image denoising models is to preserve important image features while removing noise. An important image feature is given by edges: exactly to face this kind of problems, the Total Variation image restoration models were first introduced by Rudin, Osher and Fatemi in their pioneering work [80]. The variational form of this models was designed with the explicit goal of preserving sharp discontinuities (edges) in images, while removing noise and other undesired fine-scale details. The functional is convex and it is one of the simplest variational approaches having this most desirable property.

We aim to achieve the vessel enhancement task on the basis of the Total Variation regularization. In the previous chapter we used the linear multiscale theory. Now, the second derivatives and then the curvatures of the ridges are estimated on the basis of the Total Variation non-linear scale-space. After this step, we apply the same blocks introduced in Chapter 4, to achieve image binarization and cleaning. The two parameters of interest (scale and threshold) are fixed by properly maximizing only the MAA measure of performance.

5.1 Total variation regularization

TVM (Total Variation Minimization using the variational model or Total Variation Motion considering the differential form) was originally introduced in image processing by Rudin, Osher and Fatemi in [80] and then it has been used in many image processing applications. TVM is one of the earliest and best known examples of edge preserving regularization. It was designed with the explicit goal of preserving sharp discontinuities (edges) in images while removing unwanted fine scale details and among them the noise, if present in the image. Figure 5.1 shows an example of Total Variation non-linear scale space. In Figure 5.2 we can observe the edges of the image: they are preserved better than in the linear case.

The Total Variation functional, associated to energies, has appeared and has been previously studied in many different areas of pure and applied mathematics. For instance, the notion of Total Variation of a function appeared in the theory of minimal surfaces. In applied mathematics, Total Variation based models and analysis appear in more classical applications such as elasticity and fluid dynamics. Due to [80], this notion became central also in image processing.

At first, we introduce the variational form:

$$\begin{aligned} E\left(I(x,y;\tau)\right) &= \int_\Omega (I-I_0)^2 + \tau \left\|\nabla I(x,y)\right\| \, dxdy \\ &= \int_\Omega (I-I_0)^2 + \tau \sqrt{\left(\frac{\partial I(x,y)}{\partial x}\right)^2 + \left(\frac{\partial I(x,y)}{\partial y}\right)^2} \, dxdy \qquad (5.1) \end{aligned}$$

The regularization term, for smooth images, is equivalent to the L^1 norm of the first derivatives. In other words, it corresponds to the integration on the domain Ω of the gradient norm. As the gradient evaluated in a given point is a measure of the variation of the function in such point, the integration over the entire domain must result in the total variation (hence the name).

It should be noticed that TVM is non-linear, i.e., we can't define an operator T_t that, convoluted with the function I_0, returns the total variation result.

We want now to underline the mathematical properties that make this multiscale analysis edge preserving. First of all, we deduce the corresponding divergence form from the variational definition. According to Equation (3.13), we define

$$\Phi(s) = s \rightarrow \Phi(\|\nabla I\|) = \|\nabla I\| \qquad (5.2)$$

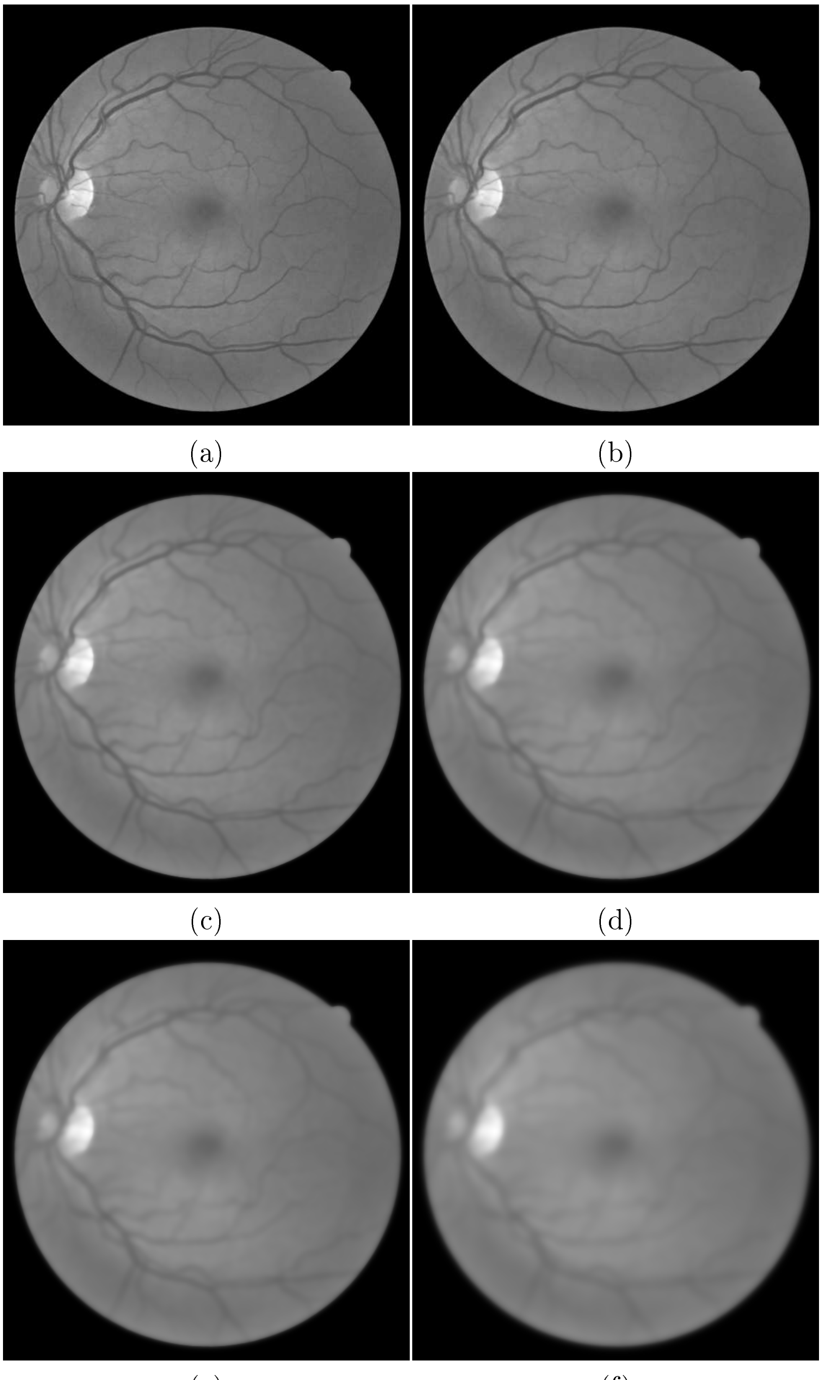

(a) (b) (c) (d) (e) (f)

Figure 5.1: Example of TV scale-space: $t = 5, 10, 50, 100, 150, 200$.

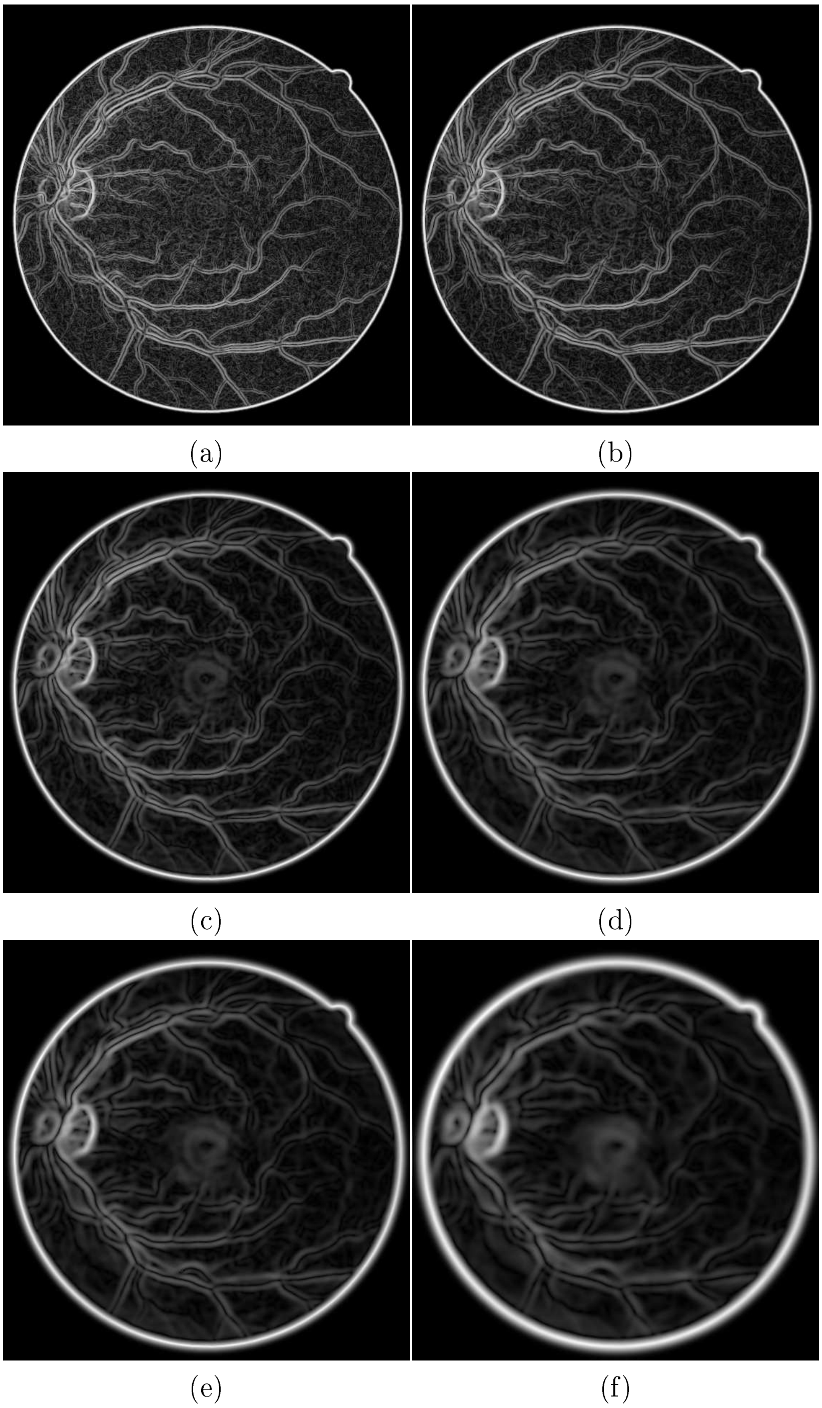

(a) (b) (c) (d) (e) (f)

Figure 5.2: Edge of a fundus image along a TV scale-space: $t = 5, 10, 50, 100, 150, 200$.

Then, having in mind Equation (3.26), we evaluate:

$$\begin{aligned} g(\|\nabla I\|) &= \frac{1}{2}\frac{\Phi'}{\|\nabla I\|} = \frac{1}{2}\frac{1}{\|\nabla I\|} \\ &= \frac{1}{2}\frac{1}{\sqrt{\left(\frac{\partial I(x,y)}{\partial x}\right)^2 + \left(\frac{\partial I(x,y)}{\partial y}\right)^2}} \end{aligned} \tag{5.3}$$

and then we are able to express the divergence form:

$$\frac{\partial I}{\partial t} = \frac{1}{2}\nabla\left(\frac{\nabla I}{\|\nabla I\|}\right) \tag{5.4}$$

with I_0 as initial condition.

Equation (5.4) represents an intermediate result. Now we derive the oriented 1D Laplacians form. This is the concluding form that allows us to understand the nature of the diffusion associated with the Total Variation:

1. For $z = \frac{\nabla_{\perp} I}{\|\nabla I\|}$ we have $c_1 = g = \frac{1}{2}\frac{1}{\|\nabla I\|}$
2. For $v = \frac{\nabla I}{\|\nabla I\|}$ we have $c_2 = g + \|\nabla I\|\, g' = \frac{1}{2}\frac{1}{\|\nabla I\|} + \frac{1}{2}\|\nabla I\|\left(-\frac{1}{\|\nabla I\|^2}\right) = 0$

Finally, we reach the result:

$$\frac{\partial I}{\partial t} = \frac{1}{2}\frac{1}{\|\nabla I\|} I_{zz} \tag{5.5}$$

This result tells us that the Total Variation Motion describes a diffusion process that follows only the direction orthogonal to the gradient ($c_1 \neq 0$, $c_2 = 0$).

No diffusion involves the local edges of the image, so no blurring of them can be observed during the diffusion process. In digital images we can have, actually, little diffusion in the direction of the edges due to incorrect estimates of the edge direction, but this effect remains anyway limited thus preserving the main features of the diffusion process.

5.2 The staircasing problem

The image restoration model, based on the Total Variation, tends to yield piecewise constant images, i.e., "blocky" images. In other words the TVM method well preserves edges but exhibits the sometimes undesiderable *staircase effect*, namely the transformation of smooth regions (*ramps*) into piecewise constant regions (*stairs*). This behaviour can be clearly seen in a 1D example, like in Figure 5.3, where the regularization of a noisy signal is shown.

This feature is certainly useful for many applications, but it can be a serious drawback for many others. This is true for our case, since the staircase effect reduces the ridgeness of the vessels.

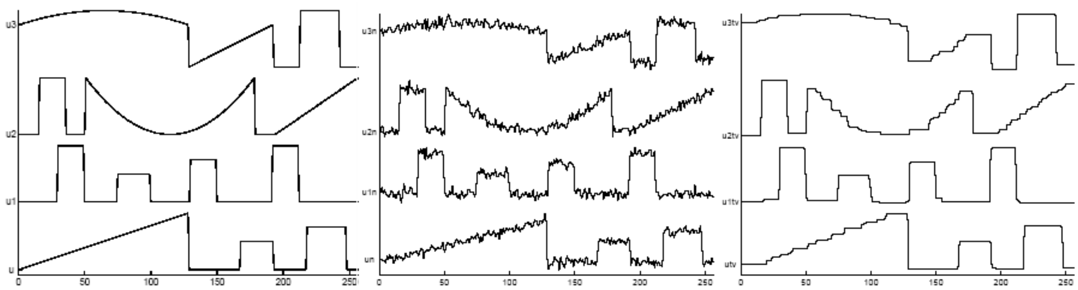

Figure 5.3: Left: original 1D signals. Center: noisy 1D signals, $SNR \approx 5$. Right: result of TV restoration.

This behaviour is mainly due to huge diffusion near critical points where the gradient magnitude of the image is zero, i.e., $\|\nabla I\| = 0$. We can also notice that Equation (5.4) is not defined at these points, due to the presence of the term $1/\|\nabla I\|$.

To solve this problem it is common in the literature [81] to introduce a slightly perturbed norm

$$\begin{aligned} \|\nabla^{\epsilon} I\| &\equiv \sqrt{\|\nabla I\|^2 + \epsilon^2} \\ &= \sqrt{\left(\frac{\partial I(x,y)}{\partial x}\right)^2 + \left(\frac{\partial I(x,y)}{\partial y}\right)^2 + \epsilon^2} \end{aligned} \tag{5.6}$$

with $\epsilon \in \Re$. At the end of this section we will show the effects of this choice on the behaviour of the diffusion process.

5.2.1 Variational and differential form using the perturbed norm

Now, we want to derive the divergence and the oriented 1D Laplacians form from the variational definition of our problem (TVM with the pertubed norm). We start from the general definition of a variational problem involving the perturbed norm, then we get the two differential representations from this (divergence form and oriented 1D Laplacians form). In a second time we obtain the particular results for the TVM case. At the end we will be able to directly understand how the introduction of the perturbed norm affects the diffusion behaviour.

First of all, it can be easily noticed that every function of the perturbed norm is implicity a function of the gradient magnitude

$$f\left(\|\nabla^{\epsilon} I\|\right) = f\left(\sqrt{\|\nabla I\|^2 + \epsilon^2}\right) = \Phi_{\epsilon}\left(\|\nabla I\|\right) \tag{5.7}$$

This simple consideration allows us to reuse the results of Chapters 3. For the sake of convenience, we introduce the following notations:

$$\begin{aligned} \delta &= \|\nabla I\| \\ \delta_{\epsilon} &= \|\nabla^{\epsilon} I\| = \sqrt{\|\nabla I\|^2 + \epsilon^2} \end{aligned} \tag{5.8}$$

Then according to what reported above we have

$$\delta_{\epsilon} = \sqrt{\delta^2 + \epsilon^2} \tag{5.9}$$

$$\lim_{\epsilon \to 0} \delta_{\epsilon} = \delta \tag{5.10}$$

Before going on, it is useful to introduce the following results:

1.

$$\begin{aligned} \Phi'_{\epsilon}(\delta) &:= \frac{\partial \Phi_{\epsilon}}{\partial \delta} = \frac{\partial f\left(\delta_{\epsilon}\right)}{\partial \delta_{\epsilon}} \frac{\partial \delta_{\epsilon}}{\partial \delta} \\ &= f' \frac{\partial}{\partial \delta}\left(\sqrt{\delta^2 + \epsilon^2}\right) = f' \frac{1}{2} \frac{2\delta}{\sqrt{\delta^2 + \epsilon^2}} \\ \Rightarrow \Phi'_{\epsilon}\left(\delta\right) &= f' \frac{\|\nabla I\|}{\|\nabla^{\epsilon} I\|} \end{aligned} \tag{5.11}$$

2.

$$\begin{aligned}
\Phi''_\epsilon(\delta) &= \frac{\partial}{\partial\delta}\left(f'\frac{\delta}{\delta_\epsilon}\right) = \frac{\partial f'}{\partial\delta}\frac{\delta}{\delta_\epsilon} + f'\frac{\partial}{\partial\delta}\left(\frac{\delta}{\delta_\epsilon}\right) \\
&= \frac{\partial f'}{\partial\delta_\epsilon}\frac{\partial\delta_\epsilon}{\partial\delta}\frac{\delta}{\delta_\epsilon} + f'\frac{\partial}{\partial\delta}\left(\frac{\delta}{\sqrt{\delta^2+\epsilon^2}}\right) \\
&= f''\frac{\delta}{\delta_\epsilon}\frac{\delta}{\delta_\epsilon} + f'\frac{\delta_\epsilon - \frac{\delta\delta}{\delta_\epsilon}}{\delta_\epsilon^2} \\
&= f''\frac{\delta^2}{\delta_\epsilon^2} + f'\frac{\delta_\epsilon^2 - \delta^2}{\delta_\epsilon^3} \\
\Rightarrow \Phi''_\epsilon &= f''\frac{\|\nabla I\|}{\|\nabla^\epsilon I\|} + f'\frac{\|\nabla^\epsilon I\|^2 - \|\nabla I\|^2}{\|\nabla^\epsilon I\|^3} \qquad (5.12)
\end{aligned}$$

Now, we have all the elements to define completely the mathematical framework for a general problem involving the perturbed norm. We define the variational form of this problem as follows

$$\begin{aligned}
&\int_\Omega (I - I_0)^2 + \tau f(\|\nabla^\epsilon I\|)\, dxdy = \\
&\int_\Omega (I - I_0)^2 + \tau\Phi_\epsilon(\delta)\, dxdy \qquad (5.13)
\end{aligned}$$

from this and having in mind Equation (3.26), we can describe the differential problem associated to this, using a PDE in the divergence form:

$$\begin{aligned}
\frac{\partial I}{\partial t} &= \nabla\left(\frac{\Phi'_\epsilon}{\|\nabla I\|}\nabla I\right) \\
&= \nabla\left(f'\frac{\|\nabla I\|}{\|\nabla^\epsilon I\|}\frac{1}{\|\nabla I\|}\nabla I\right) \\
\Rightarrow \frac{\partial I}{\partial t} &= \nabla\left(\frac{f'}{\|\nabla^\epsilon I\|}\nabla I\right) \qquad (5.14)
\end{aligned}$$

and then derive the oriented 1D Laplacians form. We have to consider a PDE of the kind

$$\frac{\partial I}{\partial t} = c_1 I_{zz} + c_2 I_{vv} \qquad (5.15)$$

for which we calculate the values of the two diffusion coefficients that weigh, respectively, the diffusion in the directions orthogonal ($\mathbf{z}$) and parallel ($\mathbf{v}$) to the gradient:

$$c_1 = \frac{\Phi'_\epsilon}{\delta} = \frac{f'}{\|\nabla^\epsilon I\|} \tag{5.16}$$

$$c_2 = \Phi''_\epsilon = f'' \frac{\|\nabla I\|}{\|\nabla^\epsilon I\|^2} + f' \frac{\|\nabla^\epsilon I\|^2 - \|\nabla I\|^2}{\|\nabla^\epsilon I\|^3} \tag{5.17}$$

5.2.2 Variational and differential form for TVM case

For the specific TVM case we have to consider:

$$\begin{aligned} f(\delta_\epsilon) &= \Phi_\epsilon(\delta) = \sqrt{\delta^2 + \epsilon^2} = \delta_\epsilon \\ f' &= 1 \\ f'' &= 0 \end{aligned} \tag{5.18}$$

Using these results we calculate the exact expression of TVM in all the three representations:

VARIATIONAL FORM

$$\int_\Omega (I - I_0)^2 + \tau \|\nabla^\epsilon I\| \, dxdy \tag{5.19}$$

DIVERGENCE FORM

$$\frac{\partial I}{\partial t} = \nabla \left(\frac{\nabla I}{\|\nabla^\epsilon I\|} \right) \tag{5.20}$$

1-D LAPLACIANS FORM

$$c_1 = \frac{1}{\|\nabla^\epsilon I\|}$$

$$c_2 = \frac{\|\nabla^\epsilon I\|^2 - \|\nabla I\|^2}{\|\nabla^\epsilon I\|^3} \tag{5.21}$$

The result for the Laplacian form is interesting since it shows that, introducing a pertubation in the norm $\|\nabla I\|$, we have consequently the presence of a component of the diffusion also in the direction parallel to the gradient ($c_2 \neq 0$). For $\epsilon \to 0$ we come back to the TVM as described in Section 5.1 (staircase problem). Then, for increasing values of ϵ, the amount of diffusion across the edges increases gradually and we can easily observe a larger amount of blur in the regularized image, up to the complete loss of the edge preserving properties typical of a TVM scheme.

The choice of a useful value of ϵ should represent a trade-off between these two opposite behaviours, but we will show that this seems not to be a critical choice.

5.3 The improved algorithm

At this point we want to test the behaviour of the TVM (and its edge preserving properties) in a segmentation application. To do this, we work with a modified version of the algorithm introduced in the previous chapter. It changes since now we use the nonlinear scale-space $I(x, y, t)$ due to TVM, instead of a linear scale-space. The algorithm can be summarized as follows:

1. Contrast enhancement pre-processing
2. TVM diffusion using Equation (5.20); we obtain the non-linear scale-space $I(x, y, t)$
3. Evaluation of the second derivatives and then the Hessian matrix and its eigenvalues across the scales; we obtain the function $\tilde{I}(x, y, t)$, equivalent to the function intoduced by Equation (4.11)
4. Histogram-based binarization
5. Cleaning
6. FOV removal

We remark that for the TVM the scale parameter is the time t required by the diffusion process: the higher time, the higher the blurring we can observe into the areas of the image bounded by edges. Once obtained the image at a certain scale t we evaluate the spatial derivatives by the convolution of our image with the derivatives of a Gaussian with standard deviation $\sigma_{der} = 0.5$ and so the Hessian matrix and its eigenvalues. We choose $\sigma_{der} = 0.5$ to have a robust estimation of the second derivatives without perturbing too much, with a further linear multiscale analysis, the results from TVM.

The same blocks introduced in Chapter 4, for image binarization, cleaning and FOV removal are then applied to obtain the segmentation of the vessel tree of the fundus retina images. The "optimal" scale and histogram based threshold are still chosen by maximazing a MOP. In this chapter we only deal with MAA measure (for further detail, see Section 4.4).

5.4 Simulation results

In this section we show the results obtained by using the modified segmentation algorithm. We want only to offer an overview on significant performances, to point out manifest improvements we achieve with this new version of the algorithm. For the TVM we have to take into account also the value of the perturbation ϵ used to avoid or reduce the staircase effect. We use the results presented in this section also to investigate and discuss how they are influenced by this new parameter in the multiscale analysis.

We anticipate that this parameter seems to be not critical. This topic has not been faced in this thesis, but "optimal" values of ϵ could be automatically calculated starting from geometrical measures related to the mean value of the vessel edges in the image to be regularized. Starting from the variational model of the Total Variation, it can be shown that the value of the perturbation of the norm discriminates between "low edges" and "high edges" [80]. Low edges are assimilated to the noise and blurred like this. For high edges we can observe minimum diffusion across the edge, similar to the case of the Total Variation without perturbed gradient norm.

We report the results we obtained by considering four different values of the perturbation ϵ. First of all, regardless the value of ϵ, we obtain close "optimal" values for t and n_{Th}, after the training phase as described in Section 4.4. By maximazing the MAA measure of performance, we have:

$\epsilon = 10 \rightarrow (t = 20.364;\ n_{Th} = 0.9084)$

$\epsilon = 100 \rightarrow (t = 21.406;\ n_{Th} = 0.9096)$

$\epsilon = 150 \rightarrow (t = 21.058;\ n_{Th} = 0.9087)$

$\epsilon = 200 \rightarrow (t = 20.524;\ n_{Th} = 0.9025)$

Once we have obtained the optimal values of t and n_{Th}, we apply the algorithm to the first 20 images of the DRIVE database to test its perfomance.

The first two columns of Table IV contain the mean values and the standard deviations of the MAA, obtained by processing the images of the test set. The parameters t and n_{Th} are fixed at their optimal values for each case, considering $\epsilon = 10, 100, 150, 200$. The values of MAA corresponding to the best (third column) and worst (fourth column) cases are also shown. The fifth and sixth columns contain the mean values of TPF and FPF, respectively, for the 20 images of the test set. In Figure 5.4, the segmented images corresponding to the best (first row) and worst (second row) cases are provided for the test set, for $\epsilon = 150$ (corresponding to the best result) and for $\epsilon = 100$ and $\epsilon = 200$. The number of original images in the database is given.

Table IV

Table 5.1: Mean values, standard deviations, best and worst cases, mean TPF and FPF for $\epsilon = 10, 100, 150, 200$ with t and n_{Th} set to their optimal values for MAA.

MAA	Mean	Standard deviation	Best case	Worst case		Mean TPF	Mean FPF
with $\epsilon = 10$	0.94209	0.0074597	0.96104	0.92992		0.65478	0.010646
with $\epsilon = 100$	0.94327	0.0078334	0.96253	0.93009		0.65362	0.0095701
with $\epsilon = 150$	0.94329	0.0074413	0.96149	0.9324		0.64893	0.0091484
with $\epsilon = 200$	0.94320	0.0076326	0.96163	0.9306		0.64701	0.0094993

For the four considered values of ϵ, the results in Table IV suggest the presence of a (sub)optimal value $\epsilon = 150$ which gives us the best $MAA = 0.94329$. Compared with the $MAA = 0.94183$, obtained with a linear scale space, we have clearly better results, even with a lower variance (0.00746 instead of 0.00822 in the previous case).

Moreover, for $\epsilon = 100$ and $\epsilon = 200$ the results seem to not vary too much: on a visual inspection the results are almost identical. The MAA corresponding to these two values are very close to the one for $\epsilon = 150$. We point out that the introduction of the perturbation in the gradient norm is not useless: for $\epsilon = 10$ we can observe a lower MAA due to a higher influence of the staircase effect, however still having better results than the linear case.

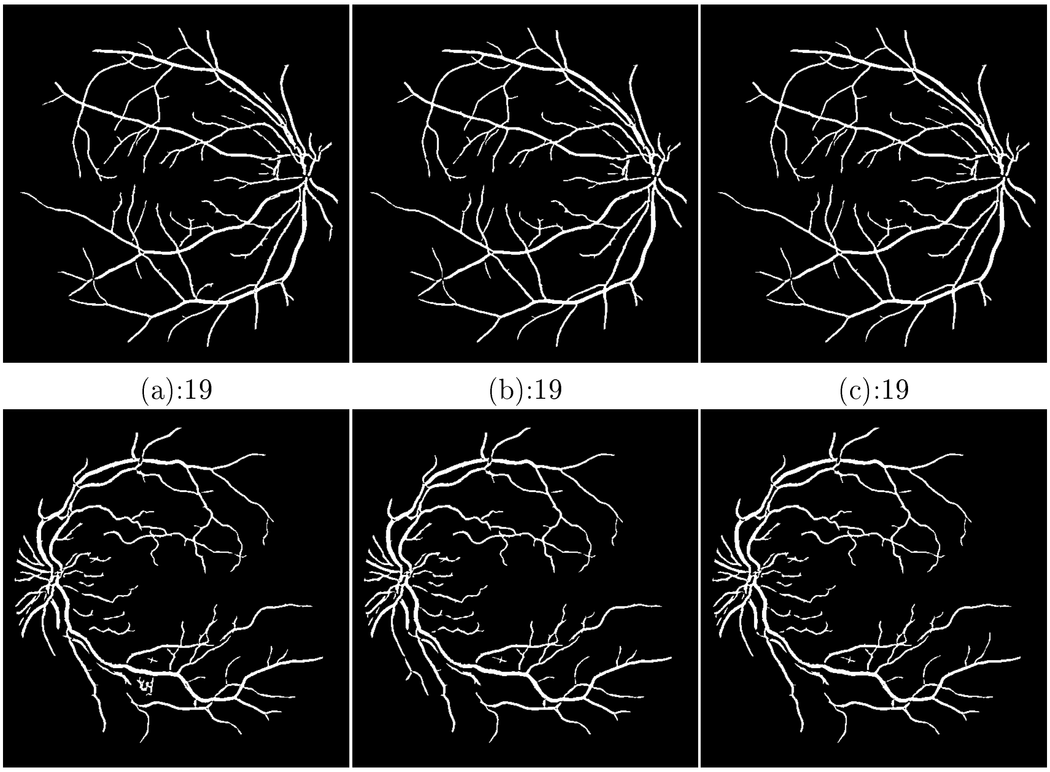
(a):19 (b):19 (c):19

(d):3 (e):3 (f):3

Figure 5.4: Best (first row) and worst (second row) vessel extraction results for the test set in terms of MAA for $\epsilon = 100$ (a,d), $\epsilon = 150$ (b,e), $\epsilon = 200$ (c,f). The database numbers of the original images are shown next to the labels.

5.5 Simulation results with noisy images

In many real applications, in the course of acquiring, transmitting, or processing, digital images are perturbed by noise. The noise is usually described by its probabilistic model, e.g., gaussian noise is characterized by two moments (mean and standard deviation of a gaussian distribution of density of probability).

Application-dependent, a degradation often yields a resulting signal/image observation model, and the most commonly used is the additive one:

$$I_N(x, y) = I(x, y) + \eta(x, y) \tag{5.22}$$

where the observed image I_N includes the original signal I and the independent and identically distributed (i.i.d) noise process η.

The Total Variation Motion is designed to work with noisy images. We have decided to test this multiscale analysis using noisy fundus retina images of the DRIVE database, corrupted by Additive White Gaussian Noise (AWGN). This is a gaussian noise with zero mean characterized by its standard deviation σ_{noise}. It is modeled by an additive scheme like the one of Equation (5.22).

In Figure 5.5 we can see two examples of noisy fundus retina images.

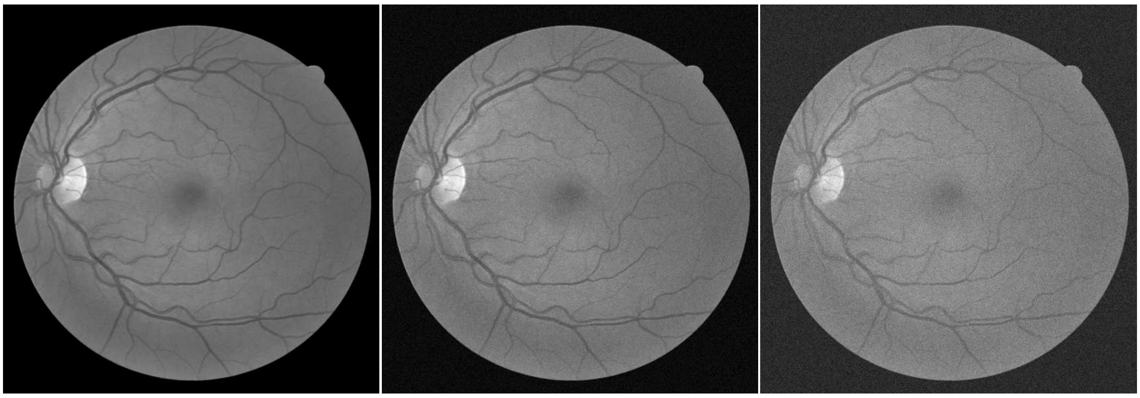

(a) (b) (c)

Figure 5.5: (a) Original image. (b) Noisy image, $\sigma_{noise} = 5$. (c) Noisy image, $\sigma_{noise} = 10$.

We consider two cases: $\sigma_{noise} = 5$ and $\sigma_{noise} = 10$. We compare the results we obtain with the TVM based algorithm with the results we would have by using the algorithm based on a linear multiscale analysis. In any case, we refer to the mean MAA value for the 20 images of the test set. The optimal scales and thresholds are fixed after a training phase on the last 20 images of the database, corrupted with AWGN noise.

Tables V and VI show the results for the two considered standard deviations σ_{noise}, for different values of the perturbation ϵ of the gradient norm.

Also in this case, among the values of ϵ chosen to study the behaviour of our algorithm, the value $\epsilon = 150$ gives the best result. Besides, for $\epsilon = 100$ and $\epsilon = 200$, the MAA don't vary too much. In Figures 5.6 and 5.7 the segmented images corresponding to the best (first row) and worst (second row) cases are provided for the test set, for $\epsilon = 100, 150, 200$ and considering, respectively, the two cases $\sigma_{noise} = 5$ and $\sigma_{noise} = 10$. The number of original images in the database is given.

Table V

Table 5.2: Noisy image results for TVM scale-space based segmentation (noise AWGN with $\sigma_{noise} = 5$): mean values, standard deviations, best and worst cases, mean TPF and FPF for the MAA with t and n_{Th} set to their optimal values.

MAA	Mean	Standard deviation	Best case	Worst case		Mean TPF	Mean FPF
with $\epsilon = 10$	0.93818	0.007082	0.09539	0.92420		0.64813	0.0128
with $\epsilon = 100$	0.94098	0.007169	0.95535	0.92773		0.65730	0.0115
with $\epsilon = 150$	0.94147	0.006826	0.95646	0.92867		0.65939	0.0113
with $\epsilon = 200$	0.94112	0.006774	0.95518	0.92852		0.65247	0.0109

Table VI

Table 5.3: Noisy image results for TVM scale-space based segmentation (noise AWGN with $\sigma_{noise} = 10$): Mean values, standard deviations, best and worst cases, mean TPF and FPF for the MAA with t and n_{Th} set to their optimal values.

MAA	Mean	Standard deviation	Best case	Worst case		Mean TPF	Mean FPF
with $\epsilon = 10$	0.93416	0.00695	0.94903	0.92063		0.6285	0.0139
with $\epsilon = 100$	0.93808	0.00731	0.95227	0.92486		0.6234	0.0115
with $\epsilon = 150$	0.93822	0.00737	0.95448	0.92282		0.6314	0.0104
with $\epsilon = 200$	0.93810	0.00767	0.95385	0.92209		0.6218	0.0102

To better understand the quality of the results, we present the MAA we would have by using the linear multiscale based segmentation. In Table VII the measures of the MAA using a linear scale-space are reported for the same values of the noise standard deviation as in Tables V and VI.

From the comparison of the results reported in Table VII with the ones of Tables V and VI, we can notice that the new algorithm works well also with noisy images, still providing better results than the linear case.

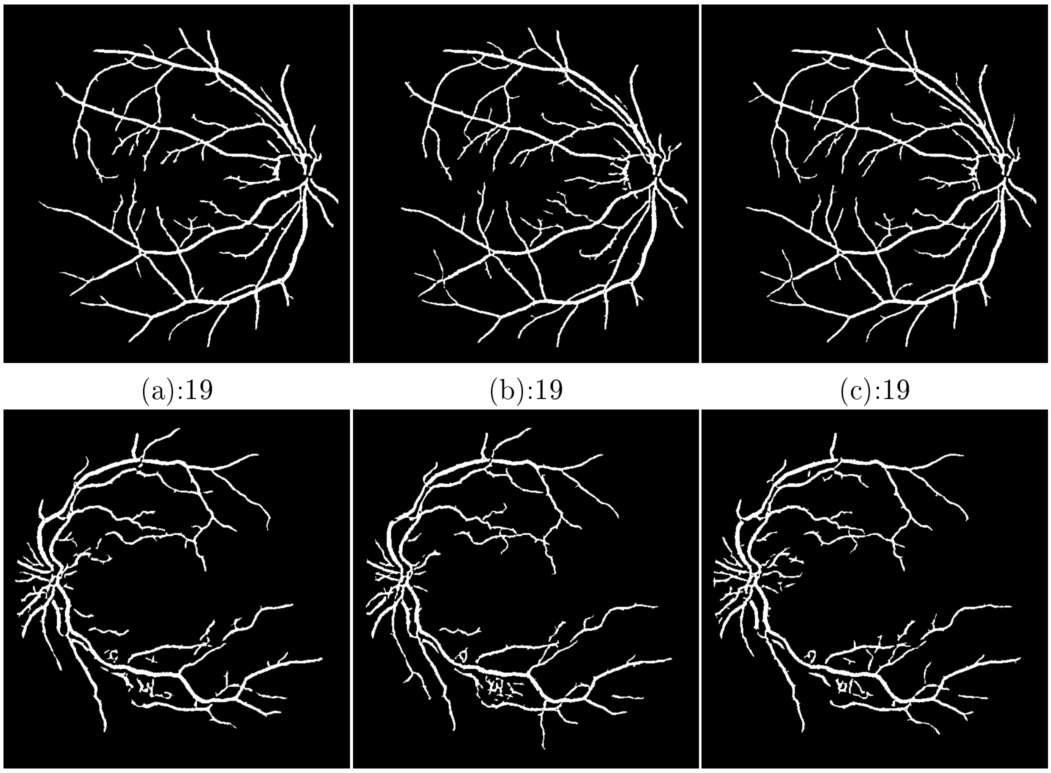

(a):19 (b):19 (c):19

(d):3 (e):3 (f):3

Figure 5.6: Best (first row) and worst (second row) vessel extraction results for the test set in terms of MAA for $\epsilon = 100$ (a,d), $\epsilon = 150$ (b,e), $\epsilon = 200$ (c,f), considering $\sigma_{noise} = 10$. The database numbers of the original images are shown next to the labels.

Table VII

Table 5.4: Noisy image results for linear scale-space based segmentation (noise AWGN with $\sigma_{noise} = 5$ and $\sigma_{noise} = 10$): Mean values, standard deviations, best and worst cases, mean TPF and FPF for the MAA with t and n_{Th} set to their optimal values.

MAA	Mean	Standard deviation	Best case	Worst case		Mean TPF	Mean FPF
with $\sigma_{noise} = 5$	0.93821	0.00786	0.95601	0.9252		0.6340	0.0118
with $\sigma_{noise} = 10$	0.93657	0.00778	0.95192	0.9218		0.5992	0.0107

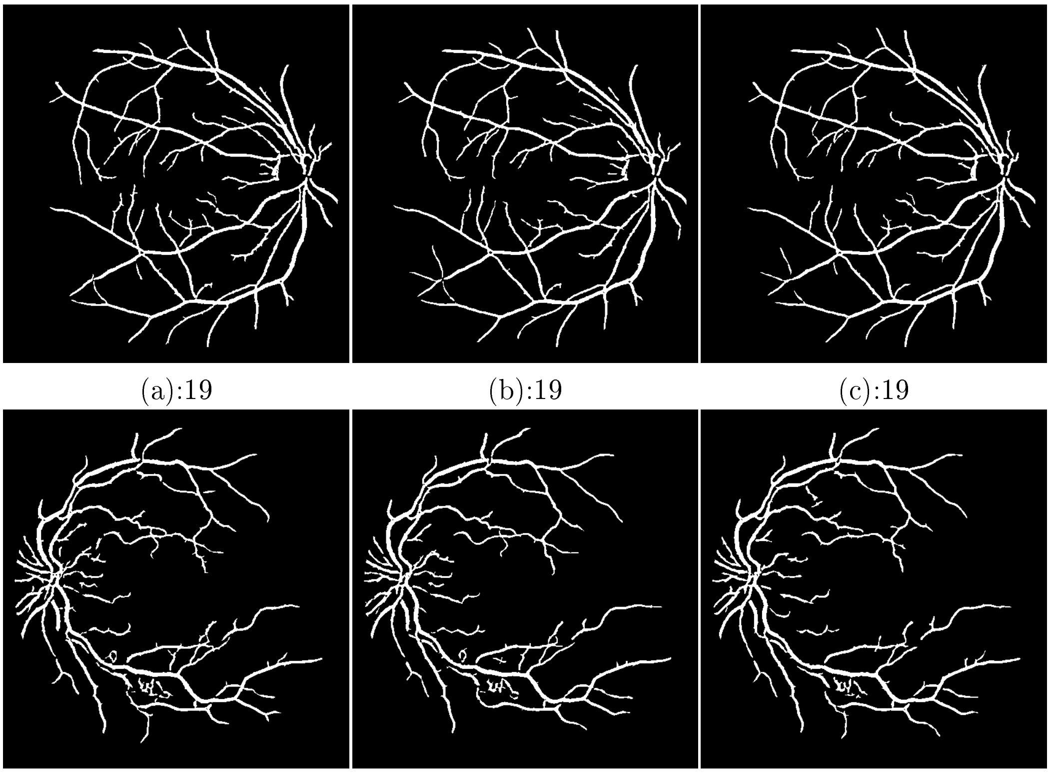

(a):19 (b):19 (c):19

(d):3 (e):3 (f):3

Figure 5.7: Best (first row) and worst (second row) vessel extraction results for the test set in terms of MAA for $\epsilon = 100$ (a,d), $\epsilon = 150$ (b,e), $\epsilon = 200$ (c,f), considering $\sigma_{noise} = 10$. The database numbers of the original images are shown next to the labels.

Chapter 6

Conclusion

In this thesis we introduced a novel algorithm for the segmentation of the vessels in fundus retina images. The algorithm has a modular structure and is made up of two fundamental blocks. The first is devoted to vessel enhancement involving multiscale theory and scale-space. Two cases are considered: linear scale-space and edge-preserving non-linear scale-space based on Total Variation Motion. The second block provides a binary image by resorting both to a thresholding procedure and cleaning operations.

The multiscale analysis framework is discussed in detail. At first we introduced the multiscale analysis referred to an operator T_t applied to an image $I(x, y)$. This was the first description of a multiscale analysis presented in the literature. Alvarez et al in [47] gave an axiomatic description of the multiscale properties and proved the relationship between operator-based multiscale analysis and PDEs. We used the Eulero-Lagrange equations to link the diffusion PDE in the divergence form with the variational method. Then we derived the oriented 1D Laplacians form and we proved this result.

We used our framework to prove or to deduce with a coherent formulation several properties of the multiscale analysis (i.e. isotropic regularization, diffusion next to the edges of the image, uniqueness of the solution). For Total Variation Motion, we gave a novel characterization of the effects related to the use of a perturbed norm. We proved the mathematical framework that describes the diffusion behaviour in proximity of the edges.

To achieve the vessel enhancement, we located the ridges in the image by evaluating the eigenvalues of the Hessian matrix. The eigenvalues give us point to point informations about the curvature along the principal direction, i.e. the direction on which we measure the maximum convexity or concavity. This allows us to save computation time with respect to other methods. As a matter of fact, for example, the matched filter approach or the morphological techniques need kernels or structuring elements at different orientations, and repeat several times the same operations for each direction.

The optimal values of the "scale" and "threshold" parameters of the algorithm were found out by maximizing proper measures of performance (MOPs). We introduced some MOPs to test the quality of our results and we compared them with other methods presented in the literature. The nonlinear algorithm outperforms the linear algorithm, working with both uncorrupted and noisy retinal images. We showed that for uncorrupted images the performances of the proposed algorithms are close to the ones of well-known algorithm presented in the literature. At best of our knowledge, no methods have been applied to noisy DRIVE database images until now, so no terms of comparison are available.

We discussed the influence that the MOPs have on the results. A research topic could be the development of further MOPs able to highlight different segmentation applications (i.e., accuracy on small vessels, vessels' widths, ramification of the vessels' tree).

The algorithm is modular. The quality of the results may be improved by adding other processing blocks. For istance, a procedure for removing pixels belonging to the edge of the optic disk could be introduced. Another improvement for image showing some pathology (e.g., drusen, exundates, and others) may be obtained by a block for the elimination of light objects before segmenting the vessels in pathological images. The presence of a block that eliminates these objects before vessel segmentation should overcome this drawback.

The modified algorithm based on the non-linear scale-space involves a new parameter: the perturbation of the gradient norm ϵ. We showed that this is not a critical parameter, unlike the scale and the threshold. Specific studies, not faced in this thesis, can be developed to identify an analytical relationship beetween the geometrical characteristics of the image and an optimal value of this parameter. Once an optimal value for this is identified, the results are robust with respect to limited changes of this value.

Further studies can be developed to analyze in detail the quality of the results, respect to increasing standard deviations of the gaussian noise and with salt and pepper noise or poissonian noise. It can be measured the different rate of the degradation of the results between the two cases, linear and non-linear.

Appendix A

From divergence form to oriented 1D Laplacians form

We have have said that a PDE in the divergence form

$$\frac{\partial I}{\partial t} = \nabla \left(\frac{\Phi\prime}{\|\nabla I\|} \nabla I \right) := \nabla \left(g \left(\|\nabla I\| \right) \nabla I \right) \tag{A.1}$$

can be rewrittten using the oriented 1D Laplacians form

$$I_t = c_1 I_{zz} + c_2 I_{vv} \tag{A.2}$$

provided that:

1. $c_1 := g$
2. $c_2 := g + \|\nabla I\| \, g'$
3. $\mathbf{z} := \frac{\nabla_{\perp} I}{\|\nabla I\|}$
4. $\mathbf{v} := \frac{\nabla I}{\|\nabla I\|}$

PROOF

We rename $\delta := \|\nabla I\| = \sqrt{I_x^2 + I_y^2}$. We have:

$$\begin{aligned} \frac{\partial I}{\partial t} &= \nabla \left(g \left(\delta \right) \nabla I \right) = \\ &= g \left(\delta \right) \nabla^2 I + \nabla g \left(\delta \right) \nabla I = \end{aligned}$$

$$= g\nabla^2 I + g_x I_x + g_y I_y \tag{A.3}$$

with

$$\begin{aligned}
g_x &= \frac{\partial g(\delta)}{\partial x} = \frac{\partial g}{\partial \delta}\frac{\partial \delta}{\partial x} = g' \frac{I_x I_{xx} + I_y I_{yx}}{\sqrt{I_x^2 + I_y^2}} = g' \frac{I_x I_{xx} + I_y I_{yx}}{\|\nabla I\|} \\
&= g' \frac{I_x I_{xx} + I_y I_{yx}}{\delta} \\
g_y &= \frac{\partial g(\delta)}{\partial y} = \frac{\partial g}{\partial \delta}\frac{\partial \delta}{\partial y} = g' \frac{I_x I_{xy} + I_y I_{yy}}{\sqrt{I_x^2 + I_y^2}} = g' \frac{I_x I_{xy} + I_y I_{yy}}{\|\nabla I\|} \\
&= g' \frac{I_x I_{xy} + I_y I_{yy}}{\delta}
\end{aligned} \tag{A.4}$$

By replacing (A.4) in (A.3), we obtain:

$$\begin{aligned}
\frac{\partial I}{\partial t} &= g\nabla^2 I + \frac{g'}{\delta}\left(I_x\left(I_x I_{xx} + I_y I_{yx}\right) + I_y\left(I_x I_{xy} + I_y I_{yy}\right)\right) \\
&= g\left(I_{xx} + I_{yy}\right) + \frac{g'}{\delta}\left(I_x^2 I_{xx} + I_x I_y I_{xy} + I_x I_y I_{yx} + I_y^2 I_{yy}\right)
\end{aligned} \tag{A.5}$$

We assume that our images are regular enough, so that $I_{xy} = I_{yx}$.

By multiplying and dividing the right hand side (r.h.s.) of equation (A.5) by the same quantity δ, we obtain:

$$\begin{aligned}
\frac{\partial I}{\partial t} &= \frac{g}{\delta^2}\delta^2\left(I_{xx} + I_{yy}\right) + \frac{g'\delta}{\delta^2}\left(I_x^2 I_{xx} + 2I_x I_y I_{xy} + I_y^2 I_{yy}\right) \\
&= \frac{g}{\delta^2}\left(I_x^2 + I_y^2\right)\left(I_{xx} + I_{yy}\right) + \frac{g'\delta}{\delta^2}\left(I_x^2 I_{xx} + 2I_x I_y I_{xy} + I_y^2 I_{yy}\right)
\end{aligned} \tag{A.6}$$

then, by adding and subtracting the same quantity to the first term of the r.h.s., we have:

$$\begin{aligned}
\frac{\partial I}{\partial t} &= \frac{g}{\delta^2}\left(I_x^2 I_{xx} + I_y^2 I_{yy} + I_x^2 I_{yy} + I_y^2 I_{xx} + 2I_x I_y I_{xy} - 2I_x I_y I_{xy}\right) \\
&\quad + \frac{g'\delta}{\delta^2}\left(I_x^2 I_{xx} + 2I_x I_y I_{xy} + I_y^2 I_{yy}\right)
\end{aligned}$$

$$
\begin{aligned}
&= \frac{g}{\delta^2}\left(I_x^2 I_{yy} - 2I_xI_yI_{xy} + I_y^2 I_{xx}\right) + \\
&\quad + \frac{g+g'\delta}{\delta^2}\left(I_x^2 I_{xx} - 2I_xI_yI_{xy} + I_y^2 I_{yy}\right)
\end{aligned} \tag{A.7}
$$

It can be easily verified that

$$
\begin{aligned}
\left(I_x^2 I_{xx} + 2I_xI_yI_{xy} + I_y^2 I_{yy}\right) &= \begin{bmatrix} I_x & I_y \end{bmatrix} \begin{bmatrix} I_{xx} & I_{xy} \\ I_{yx} & I_{yy} \end{bmatrix} \begin{bmatrix} I_x \\ I_y \end{bmatrix} \\
&= \left(\nabla I^T \boldsymbol{H}\right) \nabla I
\end{aligned} \tag{A.8}
$$

$$
\begin{aligned}
\left(I_y^2 I_{xx} - 2I_xI_yI_{xy} + I_x^2 I_{yy}\right) &= \begin{bmatrix} -I_y & I_x \end{bmatrix} \begin{bmatrix} I_{xx} & I_{xy} \\ I_{yx} & I_{yy} \end{bmatrix} \begin{bmatrix} -I_y \\ I_x \end{bmatrix} \\
&= \left(\nabla_\perp I^T \boldsymbol{H}\right) \nabla_\perp I
\end{aligned} \tag{A.9}
$$

and

$$
\|\nabla_\perp I\| = \|\nabla I\| \tag{A.10}
$$

Finally, we obtain:

$$
\begin{aligned}
I_t &= \frac{g}{\delta^2}\left[\left(\nabla_\perp I^T\right)\nabla_\perp I\right] + \frac{g+\delta g'}{\delta^2}\left[\left(\nabla I^T\right)\nabla_\perp I\right] \\
&= g\left[\left(\frac{\nabla_\perp I^T}{\|\nabla I\|} H\right)\frac{\nabla_\perp I}{\|\nabla I\|}\right] + \left(g+\delta g'\right)\left[\left(\frac{\nabla I^T}{\|\nabla I\|} H\right)\frac{\nabla I}{\|\nabla I\|}\right]
\end{aligned} \tag{A.11}
$$

This is the end of the proof, since the two terms inside the square parentheses correspond to the definition of the second directional derivatives in the directions orthogonal and parallel to, respectively, the image gradient.

Appendix B

Explicit expressions used to calculate the Q value

In this Appendix we report the explicit expressions used to calculate the mean values, the variances and the covariances of the images t and r at each window position:

$$\bar{t}(j,k) = \frac{1}{n_w^2} \sum_{p,q \in w(j,k)} t(p,q) \tag{B.1}$$

$$\sigma_t^2(j,k) = \frac{1}{n_w^2 - 1} \sum_{p,q \in w(j,k)} \left(t(p,q) - \bar{t}(j,k)\right)^2 \tag{B.2}$$

$$\sigma_t^2(j,k) = \frac{1}{n_w^2 - 1} \sum_{p,q \in w(j,k)} \left(t(p,q) - \bar{t}(j,k)\right)\left(r(p,q) - \bar{r}(j,k)\right) \tag{B.3}$$

Equations Equation (B.1) and Equation (B.2) apply, *mutatis mutandis*, also to r.

Bibliography

[1] A. Alm and A. Bill, "Ocular circulation," *Adler's Physiology of the Eye*, vol. 9, pp. 209–212, 1992.

[2] H. Tachibana, F. Gotoh, and Y. Ishikawa, "Retinal vascular autoregulation in normal subjects," *Stroke*, vol. 13, pp. 149–155, 1982.

[3] J. Jonas, G. Gusek, and G. Naumann, "Parapapillary diameters of retinal vessels. i. estimating the size of the optic papilla (a papillometric study over 264 normal eyes)," *Klinische Monatsblätter für Augenheilkunde*, vol. 192, pp. 325–328, April 1988.

[4] A. Hoover, V. Kouznetsova, and M. Goldbaum, "Locating blood vessels in retina images by piecewise threshold probing of matched filter response," *IEEE Trans. Med. Imag.*, vol. 19, pp. 203–210, March 2000.

[5] H. Novotny and D. Alvis, "A method of photographing fluorescence in circulating blood in the human retina," *Circulation*, vol. 24, pp. 82–86, 1961.

[6] http://www.isi.uu.nl/Research/Databases/DRIVE/

[7] P. Kornprobst, *Contributions à la Restauration d'Images et à l'Analyse de Séquences: Approches Variationnelles et Solutions de Viscosité.* PhD thesis, PhD thesis, Université de Nice-Sophia Antipolis, 1998.

[8] L. Florack, *Image Structure.* Kluwer Academic Publishers, 1997.

[9] L. O. Chua and T. Roska, "The cnn paradigm," *IEEE Transactions on circuits and systems-I: fundamental theory and applications*, vol. 40, pp. 147–156, 1993.

[10] T. Pavlidis and Y. Liow, "Integrating region growing and edge detection," *IEEE Transactions on Pattern Analysis and Machine Intelligence*, vol. 12, pp. 225–233, 1990.

[11] R. Haralick and L. Shapiro, "Image segmentation techniques.," *Computer Vision, Graphics and Image Processing*, vol. 29, pp. 100–132, 1985.

[12] N. Pal and S. Pal, "A review on image segmentation techniques," *Pattern Recognition*, vol. 26, pp. 1277–1294, 1993.

[13] C. Tsai, C. Stewart, H. Tanebaum, and B. Roysam, "Model-based method for improving the accuracy and repeatability of estimating vascular bifurcation and crossovers from retinal fundus images," *IEEE Trans. on Information Technology in Biomedicine*, vol. 8, pp. 122–130, June 2004.

[14] J. Staal, M. Abramoff, M. Niemeijer, M. Viergever, and B. van Ginneken, "Ridge-based vessel segmentation in color images of the retina," *IEEE Trans. Med. Imag.*, vol. 23, pp. 501–509, April 2004.

[15] M. Martinez-Perez, A. Hughes, S. Thom, A. Bharath, and K. Parker, "Segmentation of blood vessels from red-free and fluorescein retinal images," *Medical Image Analysis*, vol. 11, pp. 47–61, February 2007.

[16] C. Kirbas and F. Quek, "A review of vessel extraction techniques and algorithms," *ACM Comp. Surv.*, vol. 36, pp. 81–121, June 2004.

[17] S. Salem, N. Salem, and A. Nandi, "Segmentation of retinal blood vessels using a novel clustering algorithm (RACAL) with a partial supervision strategy," *Medical and Biological Engineering and Computing*, vol. 45, pp. 261–273, March 2007.

[18] M. Al-Rawi, M. Qutaishat, and M. Arrar, "An improved matched filter for blood vessel detection of digital retinal images," *Computers in Biology and Medicine*, vol. 37, pp. 262–267, February 2007.

[19] L. Espona, M. Carreira, M. Ortega, and M. Penedo, "A snake for retinal vessel segmentation," in *Pattern Recognition and Image Analysis*, Lecture Notes in Computer Science, pp. 178–185, Springer Berlin / Heidelberg, 2007.

[20] S. Chaudhuri, S. Chatterjee, N. Katz, M. Nelson, and M. Goldbaum, "Detection of blood vessels in retinal images using two-dimensional matched filters," *IEEE Trans. Med. Imag.*, vol. 8, pp. 263–269, Sept.s 1989.

[21] D. Eberly, *Ridges in Image and Data Analysis (Computational Imaging and Vision)*. Springer, 1996.

[22] S. Aylward, S. Pizer, E. Bullit, and D. Eberly, "Intensity ridges and widths for tabular object segmentation and registration," in *Wksp on Math. Methods in Biomed. Image Analysis*, pp. 131–138, 1996.

[23] S. Aylward and E. Bullit, "Analysis of the parameter space of a metric for registration 3d vascular images," in *Int. Conf. Med. Image Comp. and Comp.-Assisted Intervention*, 2001.

[24] R. Jain, R. Kasturi, and B. Schunck, *Machine Vision*. McGraw-Hill, Inc., 1995.

[25] M. Martinez-Perez, A. Hughes, A. Stanton, S. Thom, A. Bharath, and K. Parker, "Segmentation of retinal blood vessels based on the second directional derivative and region growing," in *Proc. ICIP 99*, vol. 2, pp. 173–176, 1999.

[26] M. Sonka, V. Hlavac, and R. Boyle, *Image Processing, Analysis, and Machine Vision.* PWS Pacific Grove - International Thomson Publishing, 1999.

[27] F. Zana and J. Klein, "Segmentation of vessel-like patterns using mathematical morphology and curvature evaluation," *IEEE Trans. Image Processing*, vol. 10, pp. 1010–1019, July 2001.

[28] M. Kass, A. Witkin, and D. Terzoopoulos, "Snake: Active contour models," *Int. J. of Comp. Vision*, vol. 1, pp. 321–331, 1988.

[29] V. Caselles, F. Catte, T. Coll, and F. Dibos, "A geometric model for active contours in image processing," *Numer. Math. 66*, vol. 1, pp. 1–32, 1993.

[30] C. Xu and J. Prince, "Snakes, shapes, and gradient vector flow.," *IEEE Trans. on Image Proces.*, vol. 7, pp. 359–369, 1998.

[31] R. Malladi, J. Sethian, and B. Vemuri, "Shape modeling with front propagation: A level set approach," *PAMI*, vol. 17, pp. 158–175, February 1995.

[32] S. Osher and J. A. Sethian, "Fronts propagating with curvature dependent speed: Algorithms based on hamilton-jacobi formulation," *Journal of Computational Physics*, vol. 79, pp. 12–49, 1998.

[33] S. Lu and S. Eiho, "Automatic detection of the coronary arterial contours with subbranches from an x-ray angiogram," *IEEE Computers in Cardiology*, vol. -, pp. 575–578, 1993.

[34] L. Lecornu, C. Roux, and J. Jacq, "Extraction of vessel contours in angiograms by simultaneous tracking of the two edges," in *IEEE Conf. Eng. in Medicine and Bio.*, vol. 1, pp. 678–679, 1994.

[35] A. Can, H. Shen, J. N. Turner, H. L. Tanenbaum, and B. Roysam, "Rapid automated tracing and feature extraction from retinal fundus images using direct exploratory algorithms," *IEEE Transactions on information technology in biomedicine*, vol. 3, p. Anza DOC, June 1999.

[36] C. Smets, G. Verbeeck, P. Suetens, and A. Oosterlinck, "A knowledge-based system for the delineation of blood vessels on subtraction angiograms.," *Pattern Rec. Lett.*, vol. 8, pp. 113–121, 1988.

[37] S. Stansfield, "Angy: A rule-based expert system for automatic segmentation of coronory vessels from digital subtracted angiograms," *PAMI*, vol. 3, pp. 188–199, March 1986.

[38] T. Kohonen, *Self-organizing Maps.* New York: Springer-Verlag, 1995.

[39] B. Ripley, *Pattern Recognition and Neural Networks.* Cambridge University Press, 1996.

[40] J. Clak, “Neural network modelling,” *Physics in Med. and Bio.*, vol. 36, pp. 1259–1317, 1991.

[41] S. Haykin, *Neural Networks: A Comprehensive Foundation*. New York: Mcmillan College, 1994.

[42] J. Soares, J. Leandro, R. C. Jr., H. Jelinek, and M. Cree, “Retinal vessel segmentation using the 2-d gabor wavelet and supervised classification,” *IEEE transactions on medical imaging*, vol. 25, pp. 1214– 1222, september 2006.

[43] T. Lindeberg, *Scale-Space Theory in Computer Vision*. Springer - Kluwer Academic Publishers, 1994.

[44] T. Lindeberg, “Edge detection and ridge detection with automatic scale selection,” *Int. J. Comput. Vision*, vol. 30, pp. 117-154, pp. 117–154, 1998.

[45] Q. Li, J. You, L. Zhang, and P. Bhattacharya, “Automated retinal vessel segmentation using multiscale analysis and adaptive thresholding,” *ssiai*, vol. 0, pp. 139–143, 2006.

[46] K. Krissian, G. Malandain, N. A. R. Vaillant, and Y. Trousset, “Model-based multiscale detection of 3d vessels,” *wbia*, vol. 00, p. 202, 1998.

[47] L. Alvarez, F. Guichard, P.-L. Lions, and J.-M. Morel, “Axioms and fundamental equations of image processing,” *Archive for Rational Mechanics and Analysis*, vol. 123, pp. 199–257, 1993.

[48] F. Catté, P.-L. Lions, J.-M. Morel, and T. Coll, “Image selective smoothing and edge detection by nonlinear diffusion,” *Siam Journal on Numerical Analysis*, vol. 32, pp. 1895–1909, 1992.

[49] J. Weickert, “Anisotropic diffusion in image processing,” tech. rep., Teubner, Stuttgart, 1998.

[50] L. Alvarez, P.-L. Lions, and J.-M. Morel, “Image selective smoothing and edge detection by nonlinear diffusion. ii,” *SIAM Journal on Numerical Analysis*, vol. 29, pp. 845–866, 1992.

[51] W. J. Niessen, K. L. Vincken, J. Weickert, and M. A. Viergever, “Nonlinear multiscale representation for image segmentation,” *Computer Vision and Image Understanding*, vol. 66, pp. 233–245, 1997.

[52] P. Charbonnier, L. Blanc-Féraud, G. Aubert, and M. Barlaud, “Two deterministic half-quadratic regularization algorithms for computed imaging.,” in *Proc. IEEE International Conference on Image Processing* (I. C. society press, ed.), vol. 2, pp. 168–172, Nov. 1994.

[53] R. Deriche and O. Faugeras, "Les edp en traitment des images et vision par ordinateur," *Traitment du Signal*, vol. 13, pp. 551–577, 1996. Numero Special.

[54] K. Ito and K. Kunisch, "An active set strategy based on the augmented lagrangian formulation for image restoration," *RAIRO Mathematical Models and Numerical Analysis*, vol. 33, pp. 1–21, 1999.

[55] N. Nordstrom, "Biased anisotropic diffusion - a unified regularization and diffusion approach to edge detection," *Image and vision computing*, vol. 8, pp. 318–327, 1990.

[56] Schnorr, "Unique reconstruction of piecewise smooth images by minimizing stricly convex non-quadratic functionals," *Journal of mathematical imaging and vision*, vol. 4, pp. 189–198, 1994.

[57] O. Scherzer and J. Weickert, "Relations between regularization and diffusion filtering," *Journal of mathematical imaging and vision*, vol. 12, pp. 43–63, 2000.

[58] J. Weickert, "Application of nonlinear diffusion in image processing and computer vision," in *Proceedings of algoritmy* (A. M. U. Comenianae, ed.), vol. LXX, pp. 33–50, 2000.

[59] H. Urakawa, *Calculus of Variations and Harmonic Maps*, vol. 132 of *Translations of Mathematical Monographs*. American Mathematical Society, 1993.

[60] P. Kornprobst, R. Deriche, and G. Aubert., "Nonlinear operators in image restoration," in *Proceedings of the International Conference on Computer Vision and Pattern Recognition* (I. C. Society, ed.), (Puerto Rico), pp. 325–331, IEEE, June 1997.

[61] P. Charbonnier, L. Blanc-Feraud, G. Aubert, and M. Barlaud., "Deterministic edgepreserving regularization in computed imaging," *IEEE Transactions on Image Processing*, vol. 6, pp. 298–311, 1997.

[62] A. Anzalone, F. Bizzarri, P. Camera, L. Petrillo, and M. Storace, "DSP implementation of a low-complexity algorithm for real-time automated vessel detection in images of the fundus of the human retina," in *Proc. of the 2007 IEEE International Symposium on Circuits and Systems (ISCAS'2007)*, pp. 97–100, May 27-30 2007.

[63] P. Feng, Y. Pan, B. Wei, W. Jin, and D. Mi, "Enhancing retinal image by the Contourlet transform," *Pattern Recognition Letters*, vol. 28, pp. 516–522, March 2007.

[64] M. Foracchia, E. Grisan, and A. Ruggeri, "Luminosity and contrast normalization in retinal images," *Medical Image Analysis*, vol. 9, pp. 179–190, June 2005.

[65] S. Pizer, E. Amburn, J. Austin, R. Cromartie, A. Geselowitz, T. Greer, B. ter Haar Romeny, and J. Zimmerman, "Adaptive histogram equalization and its variations," *Computer Vision, Graphics and Image Processing*, vol. 39, pp. 355–368, September 1987.

[66] K. Zuiderveld, "Contrast limited adaptive histogram equalization," in *Graphics Gems IV*, pp. 474–485, San Diego, CA, USA: Academic Press, 1994.

[67] Y. Sato, S. Nakajima, H. Atsumi, T. Koller, G. Gering, S. Yoshida, and R. Kikinis, "3D multi-scale line filter for segmentation and visualization of curvilinear structures in medical images," in *Proc. CVRMed-MRCAS*, pp. 213–222, 1997.

[68] C. Lorenz, I. Carlsen, T. Buzung, C. Fassnacht, and J. Weese, "Multi-scale line segmentation with automatic estimation of width, contrast and tangencial direction in 2D and 3D medical images," in *Proc. CVRMed-MRCAS*, (London, UK), pp. 233–242, Springer-Verlag, 1997.

[69] A. N. Tikhonov, "Regularization of incorrectly posed problems," *Soviet. Math. Dokl.*, vol. 4, pp. 1624–1627, 1963.

[70] G. B. Folland, *Fourier Analysis and its Applications.* The Wadsworth & Brooks/Cole Mathematics Series. Brooks/Cole Advanced Books & Software, 1992.

[71] J. Koenderink, "The structure of images," *Biological Cybernetics*, vol. 50, pp. 363–370, 1984.

[72] A. P. Witkin, "Scale-space filtering: a new approach to multi-scale description," *Image Understanding*, vol. 1984, pp. 79–95, 1984.

[73] M. Niemeijer, J. Staal, B. van Ginneken, M. Loog, and M. Abramoff, "Comparative study of retinal vessel segmentation methods on a new publicly available database," in *SPIE Medical Imaging* (J. M. Fitzpatrick and M. Sonka, eds.), vol. 5370, pp. 648–656, SPIE, SPIE, May 2004.

[74] J. Landis and G. Koch, "The measurement of observer agreement for categorical data," *Biometrics*, vol. 33, pp. 159–174, March 1977.

[75] Z. Wang and A. Bovik, "A universal image quality index," *IEEE Signal Processing Letters*, vol. 9, pp. 81–84, March 2002.

[76] J. C. Lagarias, J. A. Reeds, M. H. Wright, and P. E. Wright, "Convergence properties of the nelder-mead simplex method in low dimensions," *SIAM Journal of Optimization*, vol. 9, no. 1, pp. 112–147, 1998.

[77] F. Zana and J. Klein, "A multimodal registration algorithm of eye fundus images using vessels detection and hough trasform," *IEEE Trans. Med. Imag.*, vol. 18, pp. 419–428, May 1999.

[78] X. Jiang and D. Mojon, "Adaptive local thresholding by verification-based multithresholding probing with application to vessel detection in retinal images," *IEEE Trans. on Pattern Analysis and Machine Intelligence*, vol. 25, pp. 131–137, Jan. 2003.

[79] M. Martinez-Perez, A. Hughes, A. Stanton, S. Thom, A. Bharath, and K. Parker, "Scale-space analysis for the characterization of retinal blood vessels," in *Proc. Image Understanding and Analysis (MIUA'99)*, pp. 57–60, July 1999.

[80] L. Rudin, S. Osher, and E. Fatemi., "Nonlinear total variation based noise removal algorithms," *Physica D*, vol. 60, pp. 259–268, 1992.

[81] C. R. Vogel and M. E. Oman, "Iterative methods for total variation denoising," *SIAM Journal on Scientific Computing*, vol. 17, no. 1, pp. 227–238, 1996.